Advanced Diamond Microfabrication for Microoptics and Photonics

Thèse N° 9771

Présentée le 31 octobre 2019

à la Faculté des sciences et techniques de l'ingénieur
Groupe Quack
Programme doctoral en photonique

pour l'obtention du grade de Docteur ès Sciences

par

Marcell Kristof KISS

Acceptée sur proposition du jury

Prof. Y. Bellouard, président du jury
Prof. N. Quack, directeur de thèse
Prof. P. Olivero, rapporteur
Prof. M. Karlsson, rapporteur
Dr T. Scharf, rapporteur

2019

ÉCOLE POLYTECHNIQUE
FÉDÉRALE DE LAUSANNE

Acknowledgements

First and foremost, I would like to express my gratitude to my thesis supervisor, Prof. Niels Quack for the opportunity to conduct this research at the Quack Group at EPFL. I am grateful for his guidance and expertise that was crucial for realizing this thesis. I always felt welcome in his office and his encouragement lifted my spirit when the results did not meet my expectations. This work would not have been possible without his support. I thank Prof. Olivero, Prof. Karlsson and Dr. Scharf for the time they spent on reviewing this work and their helpful comments, and Prof. Yves Bellouard for accepting to be the president of my jury. I would like to thank the EPFL professors and staff that helped me with the experimental work during the thesis. I gratefully acknowledge the support of Prof. Martin, Dr. Scharf, and Dr. Santschi for the hospitality and the experimental support, especially during the first years of our group. I would like to thank Prof. Damjanovic and Alessandro Mapelli for the access to the vacuum furnace. I thank Prof. Harry Whitlow and Dr. Max Doebeli for access to implantation services. I thank Prof. Christophe Galland for his help with the Raman measurements. I would like to thank the CMI staff and the III/V cleanroom staff for the trainings and support in the cleanroom fabrication - both with technical matters and discussions and David Desscan for our discussions and his help administering our IT infrastructure. I thank Beatrice Raball and Cathy Buchs with their navigating the administrative tasks during this PhD. I am grateful to all the members of the group: Sichen Mi, Adrien Toros, Dorian Herle, Teodoro Graziosi Kiss, Gergely Huszka, Anton Lagosh, Yu Zhang, Yuji Takabayashi, Hamed Sattari, Hernan Furci, and Micol Massara for putting up with my jokes and for making the office life colourful! It was rewarding to work in such a stimulating environment. In particular, I have to acknowledge the help of Teodoro Graziosi, Sichen Mi and Adrien Toros for their work that contributed to the completion of this thesis. I thank Adrien for the help with clean room fabrication; Sichen for the development of the IBE surface polishing; and Teodoro for the countless discussions and math during the thesis, the help with FIB processing and NanoScribe experiments. I am grateful to my family for the continuous support, even as I got buried in thesis work. Finally, but most importantly, I would like to thank my girlfriend Csilla, who supported me and believed in me even when I did not: I couldn't have done it without you!

Lausanne, 8 October 2019 Marcell Kiss

Abstract

Diamond is an exceptional material – hard, stiff, transparent, which makes it ideal for the fabrication of optical and mechanical systems that take advantage of these properties. Diamond is not only "better", but it offers the possibility of integrating bright colour centres. These optically active defects can be exploited for a variety of applications, including the study of fundamental science, magnetometry, biosensing and new types of lasers.

Despite the attractive properties of diamond for optics, no standard platform exists to create photonic circuits and devices. This thesis shows the realisation of a diamond-on-insulator photonics platform, that aims to combine the versatility of the silicon-on-insulator photonics with the capability of performing diamond science in single crystal guided-wave devices. The diamond-on-insulator substrate is achieved via ion implantation-based cut of a single crystal membrane and bonding of the membrane to an insulator layer. This approach provides a monolithic fabrication process that scales to commercial exploitation, bringing convenient access to the study of diamond light-matter interactions without requiring custom substrate fabrication. Furthermore, the possibility of releasing the diamond devices adds access to freestanding structures, opening the way to diamond micro-opto-electro-mechanical systems and optomechanics.

Diamond also makes an excellent microoptics substrate, due to its high laser damage threshold, transparency and high refractive index, which is an attractive combination for high-power, compact optical systems operating in the UV, visible and near-infrared. Different diamond etching techniques are developed and investigated in this thesis, that enable the realisation of unique features. These techniques are employed to create diamond diffractive micro-optical components, which are then characterised, showing high-quality surfaces that closely match the designed features, indicating reliable fabrication and resulting in excellent optical performance. These devices have applications in high power beamsplitters, beam shapers and compact spectrometers.

Keywords: single crystal diamond, microfabrication, photonics, microoptics

Résumé

Le diamant est un matériau exceptionnel – dur, rigide, transparent, ce qui le rend idéal pour la fabrication de systèmes optiques et mécaniques qui mettent à profit ces propriétés. Le diamant n'est pas seulement « meilleur », il possède également la possibilité de contenir des centres colorés brillants. Ces défauts optiquement actifs peuvent être exploités dans une large variété d'applications, notamment en recherche fondamentale, mais aussi en magnétométrie, en biodétection et pour de nouveaux types de laser.

Malgré les propriétés attractives du diamant pour la réalisation de composants optiques, il n'existe pas de plateforme standard pour concevoir des circuits et dispositifs photoniques. Cette thèse démontre la réalisation d'une plateforme photonique diamant-sur-isolant, qui a pour but de combiner la polyvalence de la photonique sur silicium-sur-isolant avec l'utilisation du potentiel qu'offre le diamant au travers d'un dispositif monocristallin à ondes guidées. Le substrat diamant-sur-isolant est obtenu par le coupage d'une membrane de diamant monocristallin par implantation ionique suivi par le collage moléculaire de cette membrane sur une couche isolante. Cette approche permet une intégration monolithique compatible avec une exploitation commerciale, offrant un accès aisé à l'étude des interactions lumière-matière du diamant, sans avoir à recourir à une fabrication sur mesure. De plus, la possibilité de retirer partiellement la couche isolante sous le diamant donne accès à des structures autoportées, ouvrant la voie à des composants micro-opto-électro-mécaniques et optomécaniques en diamant.

Le diamant est aussi un excellent substrat pour la micro-optique, grâce à son seuil d'endommagement laser élevé, sa transparence et son haut indice de réfraction, une combinaison attractive pour les systèmes compacts de haute puissance fonctionnant dans l'ultraviolet, le visible et le proche infrarouge. Diverses techniques de gravure du diamant sont développées et étudiées dans cette thèse, et permettent la réalisation de structures aux caractéristiques singulières. Ces techniques sont ensuite utilisées pour créer des composants micro-optiques diffractifs en diamant monocristallin, caractérisés par des surfaces de haute qualité et de haute précision, indiquant une fabrication fiable et permettant d'obtenir d'excellentes performances optiques. Ces composants peuvent être utilisés pour la séparation et le modelage de faisceaux de haute puissance et pour les spectromètres compacts.

Mots clés : diamant monocristallin, microfabrication, photonique, micro-optique

Contents

1 Introduction and motivation

Microfabrication enables the creation of optical components that have characteristic sizes that are comparable to wavelength of light itself. These devices allow precise interaction with light previously not possible, and even more interestingly, it allows the fabrication of devices that exploit these phenomena on an industrial scale. Principally, two types of optical systems are in the scope of this thesis: integrated optics, where light is tightly confined inside a material and guided between devices and miniaturized versions of optical lenses and diffraction gratings, which are known as microoptics.

One of the most successful integrated optics ecosystem is the silicon-on-insulator (SOI) platform: silicon photonics has grown into an 400 million dollar business [1]. The SOI platform makes use of a thin silicon layer (device layer, 220 nm thick), that is on top of a thick (2 µm) buried silicon dioxide layer. This layer stack is attached to a silicon handle wafer (525 µm). Passive optical structures are fabricated from the device layer, featuring waveguides, grating couplers and directional couplers. Active devices can be made by integrating electrical contacts — creating modulators, variable attenuators, phase shifters and switches. Light propagates only in the device layer, where it is confined by the refractive index with respect to the surrounding air/SiO_2. Photonic integrated circuits built on SOI and III-V lasers power transceivers that are found in every datacenter, providing connectivity between electronics.

Microoptics delivers great value for fiber couplers, beam shaping and homogenizers for illumination, LIDAR and excimer lasers, photolithography, wavefront sensors for metrology and astronomy, beam samplers and beam splitters for laser applications. While optics traditionally builds on glass, microfabricated optics has expanded into many material systems, to exploit the properties not found in glass. These materials are frequently made into shape using some form of microfabrication, where moulding and ruling is not appropriate or possible. Commonly used materials for microoptics are fused silica, sapphire and silicon. While these materials are typically more expensive and more difficult to tailor, they can provide superior performance compared to glass for specific applications. Microfabrication also enables more flexibility and precision in the creation of the devices, along with convenient access to various anti-reflective and high-reflective optical coatings using vacuum deposition technology.

	single crystal diamond	**silicon**	**sapphire**	**fused silica**
Refractive index (1550 nm)	2.3878 [2]	3.5167 [3]	1.7462 [4]	1.444 [5]
Transparency window [μm]	0.22-20 [6]	1.1-6.5 [6]	0.17-5.5 [6]	0.38-2.2 [6]
Hardness [GPa]	50-110 [6]	13 [7]	15.6-17.4 [6]	7.8-8.8 [8]
Thermal conductivity [$\mathrm{W\,m^{-1}\,K}$]	2200 [6]	140 [6]	24 [6]	10 [6]
Young's modulus [GPa]	1080-1155 [9]	162 [6]	340 [6]	95 [6]

Table 1.1 – Table showing optical and mechanical properties of commonly used optical materials.

Table 1.1 shows how single crystal diamond compares in optical properties against common optical materials. It is evident that diamond has "extreme" properties: it is unsurpassed in mechanical properties (stiffness, hardness) and thermal conductivity, has a broad transparency window from the deep UV to far IR and has a refractive index only surpassed by silicon. Diamond is also a promising material for non-linear optics, due to the intrinsic high Raman shift and Raman gain [10].

Similarly to SOI, a diamond-on-insulator system can be envisaged, with a thin single crystal diamond layer taking the place of the silicon device layer. While the refractive index of diamond is smaller than the refractive index of silicon, the light still remains confined (although the designs made for an SOI platform need to be adapted to ensure correct operation). Creating a photonics platform with diamond as the waveguiding material allows for the study of light-matter interaction in diamond, as the light is tightly confined inside waveguides or resonators. Diamond is also an exceptional material for light-matter interaction due to its ability to host bright colour centres, optically active defects arising from a co-located missing carbon atom (vacancy) and a foreign atom. Diamond is host to over 500 luminescent colour centres [11], of which the most famous and most well-studied one is the nitrogen-vacancy centre (NV). This centre acts as a single photon emitter [12], as a highly sensitive magnetometer [13, 14], functions as a three-axis gyroscope [15] and performs as a biosensor for a multitude of applications [16]. Colour centres are also promising for the fabrication of light sources: this takes advantage of the optical or electrical pumping of the defects, that can then emit light at a different wavelength. There has been some experimental demonstration of the H_3 centre [17], while research is ongoing for NV and SiV [18]. With the demonstration of electrical pumping, this technology would provide this platform with access to on-chip light generation. SOI substrates are widely used to fabricate micromechanical systems as well. Silicon makes for a good mechanical material (**Table 1.1**) and the buried oxide can be used as a sacrificial layer for fabricating free-standing devices. The combination of optical and mechanical phenomena is of great interest, for example for reconfigurable integrated optics [19] or optomechanics [20]. Similar devices can also be fabricated in the diamond-on-insulator platform, which can take advantage of the higher stiffness to create high frequency MEMS and MOEMS devices, with mechanical resonators reaching the GHz range.

Diamond exhibits a high refractive index (2.4 at 635 nm [21]) and low absorption over a wide spectral range spanning from ultraviolet to far infrared. Furthermore, it provides high thermal conductivity and a remarkably high laser induced damaged threshold (LIDT), 20 times better than fused silica [22]. These properties enable compact, high power laser components and spectrometers operating in the visible and UV range that are not accessible with other materials. While the diamond material system is less developed than the competing fused silica, anti-reflection coatings [23, 24] and anti-reflection structuring [25, 26] have been demonstrated, which enable low loss optics, which are especially useful considering the high refractive index of diamond. While ruling and moulding are not possible for diamond, microfabrication can provide an avenue for creating high quality microoptical devices.

1.1 Thesis scope and outline

The aim of this thesis is to advance the current state-of-the-art of diamond microfabrication for the fabrication of optical devices. The work can be divided in to two major parts: development of a diamond-on-insulator platform and the fabrication diamond microoptical devices by application-tailored etch methods.

In the first part, the development of a diamond-on-insulator (DOI) platform is shown. This platform aims to combine the ease-of-use of an integrated optics platform, with the possibility of fabricating guided-wave structures in diamond (**Figure 1.1**). Based on previous results in literature, the fabrication method chosen is the ion implantation-based diamond membrane lift-off. This method is promising for commercial exploitation and can scale well for parallel processing of multiple substrates. While diamond layer lift-off has been demonstrated previously, this thesis shows the development of full chip transfer of diamond membranes by performing die-to-wafer bonding of the single crystal diamond substrate before the membrane is lifted off. This enables the monolithic fabrication of DOI substrates – a key requirement for commercial exploitation. However die bonding requires strict surface quality from the diamond substrates that are currently not found in substrates, so a section is dedicated to the improvement of surfaces found in as-received samples to the quality required. Subsequently the modelling and characterisation of ion implantation is treated, along with the bonding of the samples and diamond membrane lift-off. The resulting membranes are characterised to ascertain the quality.

The second part treats the development of microfabrication techniques to effectively fabricate microoptical components in diamond. To this end, different etch methods are developed, each imparting a different quality to the patterned structures. These methods are employed to fabricate high-quality surfaces, that can be exploited as diffractive microoptical devices. The thesis shows the development of V-groove and vertical sidewall binary gratings fabricated using a crystallographic etch, fabrication of free-standing microoptical and micromechanical components via a deep through etch, realisation of diamond diffractive optical elements for beam shaping via vertical etching and blazed gratings and Fresnel lenses via proportional etching. The microoptical devices yielded by these methods are characterised for optical properties, along with geometrical characterisation of the resulting features.

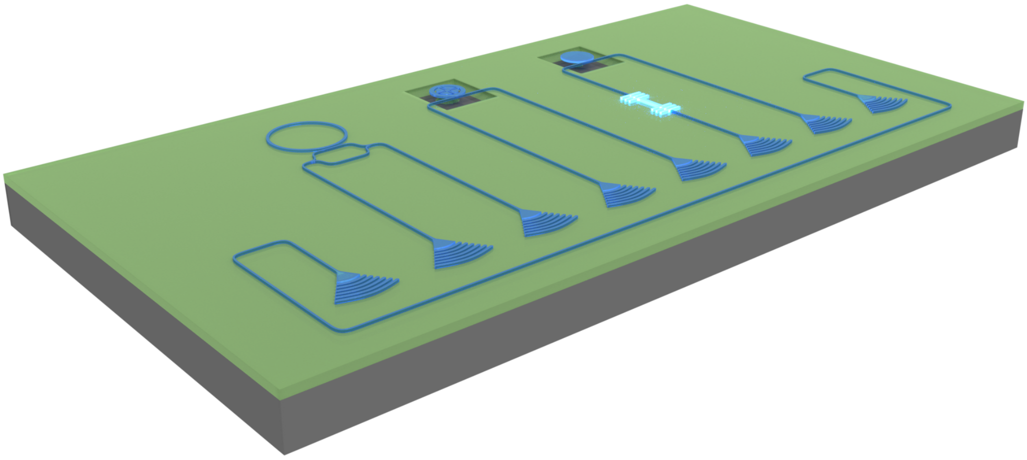

Figure 1.1 – Concept for an integrated diamond-on-insulator platform. Light is coupled in and out of the waveguides via grating couplers. Free-standing devices (microdisks and rings) are available and accessible via waveguides. Active components (based on colour centres) give convenient access to diamond science on-chip.

2 State of the art

The micromachining of diamond has seen tremendous progress over the last decade, spurred by the availability of high quality substrates becoming commercially available. In this chapter, the current state of the art will be reviewed for diamond microfabrication, with an emphasis on the possible avenues into creating integrated diamond photonics and the methods for fabricating diamond microoptical devices. First the available substrates, their fabrication and the resulting quality in the view of microfabrication for photonics is reviewed. Then the methods are reviewed for creating guided-wave optical devices, along with the demonstrations of such platforms in literature and a comparison is made between the techniques based on the reported figures-of-merit. In a similar vein, realisation of diamond micro-optical devices is examined from the processing point of view, along with exemplars of such devices in literature.

2.1 Diamond substrate growth and polishing

Commercially available single crystal diamond substrates are grown by either the high pressure-high temperature method (HPHT) or via chemical vapour deposition (CVD). These two methods have effectively displaced natural diamond for scientific experimentation, as they both offer finer control over the quality of substrate (dislocations, contaminations), offer controlled doping, have traceable origins and can produce much higher quality substrates than natural diamond, along with control over shape and a reduction in cost compared to mining.

The high pressure-high temperature seeks to mimic the conditions during natural diamond formation to produce artificial diamonds, using a temperature and pressure when diamond is a stable phase of carbon [27]. HPHT growing requires a source of carbon (like graphite), a diamond seed crystal that will serve as the template for the growth and a metallic solvent, like

Fe, Ni or Co, or an alloy of such materials. The metal acts as a catalyst during growth, enabling growth at a lower temperature. Typical pressures and temperatures are 5 GPa to 6 GPa and 1300 °C to 1600 °C [28]. The system is assembled in a way that there is a temperature gradient from the carbon source to the seed crystal, thereby forcing the carbon to dissolve into the molten metal and recrystallize as diamond on the seed. Eliminating nitrogen impurities from the source material is impossible, so a nitrogen-affine material is introduced if pure diamond is required, but this dramatically lowers the growth rate [29].

Chemical vapour deposition of diamond is a process carried out in a plasma reactor where precursor gases (typically CH_4, H_2) react due to the presence of an external energy source. Typical sources include hot-filament, radio-frequency plasma and arcjet torches, but these have been almost completely abandoned in favour of microwave plasma-type CVD processes for high quality substrates [30]. Single crystal diamond substrates are grown by placing a seed crystal in the reactor, that is grown over with diamond layers of matching configuration (homoepitaxy). CVD growth is a slow process, but produces very high quality layers, with N impurity concentrations below 1 ppb is reachable [31]. Crystal growth is especially slow in the lateral direction, which (with the increase in cost for large reactor sizes and substrate footprint) severely increases the price of large substrates. Some CVD-grown diamonds are annealed using an HPHT treatment to reduce defects, which can improve the quality of the substrate by reducing absorption [32].

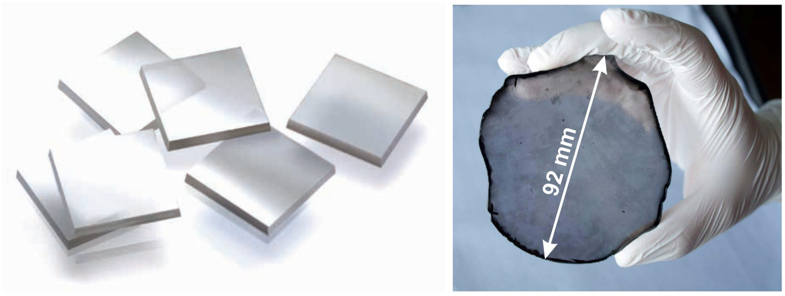

(A) **(B)**

Figure 2.1 – **(A)** Typical commercially available single crystal diamond plates used during microfabrication. Typical dimensions are 3 mm × 3 mm × 0.3 mm. Reproduced from [33]. **(B)** Wafer-scale heteroepitaxially grown single crystal diamond layer. The dark colour indicates still significant absorption form imperfections in the crystal. Reproduced from [34].

The quest for wafer scale single crystal diamond has always been a goal for the diamond microfabrication community, mimicking the developments on the silicon material system to enable large scale fabrication and integration of diamond devices. However, large scale growth using HPHT and CVD methods is difficult, while heteroepitaxial growth proved to be very challenging due to the very small lattice constant of diamond, which makes finding the appropriate substrate difficult. Recently, a growth method based on an iridium substrate has demonstrated truly single crystal, low defect density, large area ($\varnothing$= 92 mm) diamond substrates [34]. Studies carried out on this type of substrate confirm the viability of this diamond substrate type for hosting colour centres and exploiting their optical properties via microfabrication [35].

Another possibility for wafer-scale diamond growth is mosaic-type growth, where multiple seed crystals are overgrown at the same time [36]. The effect of the grain boundaries diminish over successive carbon layers, leading to a single-crystal layer. However, dislocation density remains higher at the boundaries, which can be detrimental for electronic applications [37]. A method for reducing lattice differences between the grains is to use a "cloning" method, by generating the seed crystals from the same original substrate via ion implantation and lift-off [38].

Once the diamond crystal has been grown, it is laser cut into plates. These plates are not yet suitable for microfabrication, as the laser cutting leaves a rough surface. To produce a smooth surface, grinding and polishing is carried out on the plates to render them suitable for defining micro- and nanoscale features [39]. Smooth surfaces are also a requirement for producing gemstones, and indeed, diamond polishing techniques have been developed for hundreds of years. The oldest, and still used process for polishing diamond is scaife polishing [40]: a ferrous wheel is rotated, which has diamond grit pre-dispersed on it using olive oil. The diamond pieces are pressed against the wheel during polishing. A traditional observation is that the polished crystal has "hard" and "soft" polishing directions, characterised by a large difference in material removal rate. Polishing along a "hard" direction can also damage the diamond or the scaife, and results in a rougher surface than polishing in a "soft" direction. The directions depend on the crystalline orientation of the polished surface, resulting in easy-to-polish $\{1\,0\,0\}$ faces and hard-to-polish $\{1\,1\,1\}$ faces [41]. Commercially available diamond plates typically use scaife polishing, potentially combined with other polishing methods. Scaife polishing is still actively developed [42, 43] and commercially available diamond plates are typically prepared (at least partially) via scaife polishing.

Scaife-polished diamonds have characteristic surfaces, caused by the polishing. The key features are polishing lines and pits. Polishing lines are low depth (0.2 nm to 5 nm) features attributed to individual grits on the scaife [44]. Polishing pits are large, randomly distributed features attribute to microcracking caused by polishing grits due to the brittleness of diamond [45]. These pits are up to hundreds nanometers in depth and have lateral dimensions approaching half a micrometer [46]. Apart from surface damage, there can be significant subsurface damage present, due to the mechanical polishing, manifesting as dislocations. Subsurface damage is revealed by selective etching [47, 48] or by cathodoluminescence spectra [49]. The depth of the damaged layer is difficult to quantify, but it is reported to extend to a few micrometers below the surface [45, 47, 49].

Among other contact polishing methods are chemical-mechanical polishing (CMP) [50] and thermo-chemical (or hot metal lapping) [51]. Non-contact polishing methods including reactive ion etching [52] and ion beam polishing [46] are promising techniques as well that are not yet industrially used. Reactive ion etching can also be combined with hardmask deposition and CMP for enhancing polishing [53].

Fabrication of photonic structures requires confinement of the optical mode in the structure, which is achieved by providing refractive index contrast. Diamond is a high refractive index material (2.38 at 1550 nm). The cross-section of the waveguiding structures taken in the direction of the propagation can be examined analytically or numerically to determine the set of guided wave modes that the structure can support, but in general, guided wave structures of interest require a thin strip of material surrounded either by air or another material of lower refractive index.

In the following section, such optical platforms for guided wave optics in diamond are reviewed.

2.2 Bulk diamond photonic platforms

Confinement of the optical mode can be provided by micromachining 3D structures in bulk diamond. In this case, the refractive index is provided by replacing the bulk diamond material with air or vacuum, forming waveguiding structures. A promising technique that will not be reviewed here is the femtosecond laser bulk modification of diamond, which can be used to write waveguiding structures into bulk diamond [54]. Similarly, waveguides formed by implantation induced refractive index change are not discussed [55]. In the following section, techniques for selectively milling 3D structures will be reviewed.

Focused ion beam (FIB) microfabrication is an attractive method for forming 3D structures, owing to the high degree of freedom it offers [56]. The samples are mounted on a multi-axis stage, allowing machining at different angles, the ion beam can be precisely focused, allowing for high resolution. The sample can be imaged by the focused ion beam, but typical FIB systems include a scanning electron microscope column as well, which allows for even higher resolution and more convenient imaging.

Bayn et al. uses 30 keV Ga focused ion beam to mill single crystal diamond abundant in nitrogen and NV centres [57]. Nanobeam cavities are formed by two milling steps: normal milling forms the defect region in the beam (milled as repeated lines at low current), which is followed by high current undercut from both sides of the beam at 52°. Finally the edges are defined and fine polished using a low current beam. The authors remark on the implanted Ga remaining in the diamond, with secondary ion mass spectroscopy showing that most of the ions are located in the top 5 nm. Optical characterisation reveals a *Q* factor of 221.

Similar investigation into FIB milled nanobeams are carried out by Babinec et al. [59]. A diamond membrane is fabricated by milling a large square pit into the side of the diamond plate using high current. The membrane is thinned using progressively lower beam currents to ~150 nm to 200 nm from the initial ~1 µm. Finally, the membrane is patterned into nanobeams and the nanobeams are milled with holes, using a low current beam. An alternative fabrication scheme is also proposed, where diamond lamellas are fabricated, based on the commonly used transmission electron microscope lift-off technique [60]. Slabs are milled

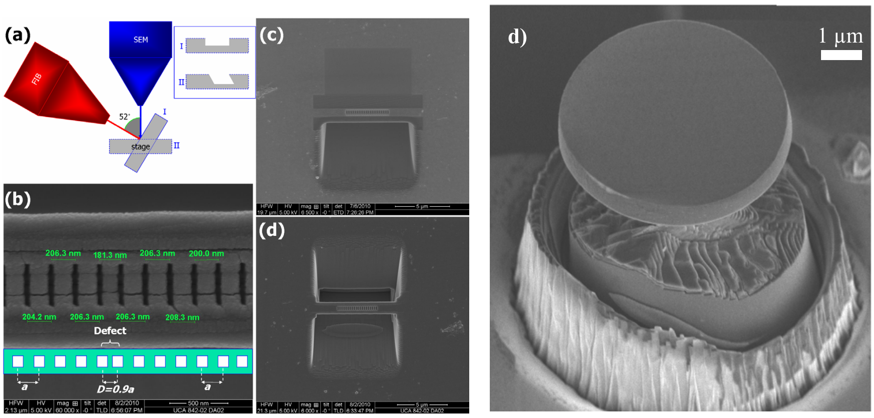

(A)

(B)

Figure 2.2 – **(A)** FIB fabricated nanobeam resonator, showing the photonic crystal formation and the undercut steps. Reproduced from [57]. **(B)** RIE etched and FIB undercut microdisk resonator. The undercut is performed from two angles to produce a rectangular pillar. Reproduced from [58].

into the diamond from a normal incidence, which are then welded to a microprobe by ion beam assisted deposition of tungsten. The slabs are then undercut and lifted out, attached to a TEM grid. The slabs are then thinned and polished, and finally patterned into nanobeams with holes. The authors report no Q factor measurements.

Microdisk resonators were fabricated by Graziosi et al. using a combination of RIE and FIB milling [58]. A pillar is defined by an initial directional oxygen reactive ion etch step, which is subsequently undercut using FIB milling from two directions. The two FIB milling steps result in a support pillar with a square cross-section. A limitation of this technique is the alignment of the two undercutting steps, which can result in non-uniformity on the underside of the resonator. The implanted Ga is removed via acid etching, plasma cleaning and thermal annealing in air. The authors report an optical Q of 5700, the highest reported quality factor by FIB machining.

In a different approach utilising directional milling, Burek et al. demonstrated a novel method for machining suspended photonic and mechanical elements [61]. Following the deposition and electron beam lithography of a Ti mask, the single crystal diamond substrate is etched using anisotropic oxygen RIE to transfer the hardmask pattern, with an etch depth of ~600 nm. Subsequently, a second anisotropic oxygen plasma etch is carried out, but at an oblique angle to the surface. This is achieved by placing the same inside a prism-shaped Faraday cage. The Faraday cage accelerates ions, defining the angle of bombardment inside the cage by the inclination of the cage wall. This "angled-etching" is used to fabricate suspended nanobeams of triangular cross-section. Nanobeam cavities are also demonstrated by including a photonic crystal pattern in the beam mask. More undercut profiles are realised by extending the fabrication method to conical Faraday cages, which can provide undercut from all directions. Conical undercut was used to demonstrate microdisks, suspended waveguides and cantilevers. This work was later extended with the fabrication and characterisation of more advanced

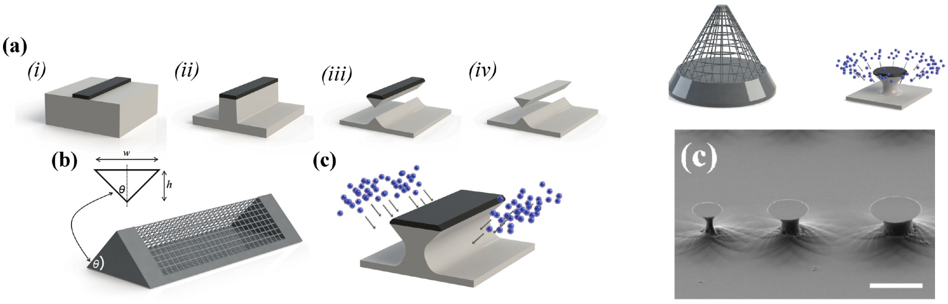

(A)

(B)

Figure 2.3 – **(A)** Process flow for fabricating free-standing nanobeam structured using a prism-shaped Faraday cage for achieving undercut. **(B)** Conical Faraday cage and schematic of the undercut for rotationally symmetric structures. SEM image of fabricated array of microdisks. To note is the misalignment of the centre of the pillar with respect to the disk due to the ion focusing effect. Reproduced from [61].

photonic devices, operating at telecom and visible wavelengths [62]. Racetrack resonators feature loaded Q-factors of $Q_{TE} \sim 151\,000$ and $Q_{TM} \sim 113\,000$ at 1550 nm wavelength. They estimate the propagation loss of the waveguides to be $\sim 1.5\,\mathrm{dB\,cm^{-1}}$.

A drawback of the "angled-etch" method using the conical cage is the focusing of the ions - while this makes the undercut possible due to introducing an angle to the ions, it also makes the resulting etch dependent on the positioning of the cage (**Figure 2.3B**). To overcome this limitation, Atikian et al. utilises a broad ion beam and the rotation of the tilted sample to achieve similar undercutting [63]. The method, termed reactive ion beam angled etching, uses an oxygen ion beam to mill the surface. The samples are first processed at a normal angle to achieve vertical etching, then tilted to an oblique angle to perform the undercut. They demonstrate racetrack resonators in polycrystalline diamond ($Q \sim 30\,000$) and single crystal diamond ($Q \sim 286\,000$). Uniformity is demonstrated by fabricating two racetrack resonators separated by 19 mm, with comparable quality factors and transmission spectra.

A recent development for bulk machining of diamond was the development of crystallographic etching and its use for fabricating microdisks by Khanaliloo et al. [64]. The process can be thought of as the analogue of the SCREAM process used in silicon microfabrication [65]. Starting from a single crystal diamond substrate, a 400 nm thick Si_3N_4 hardmask is deposited using PECVD and patterned via e-beam lithography (ZEP positive resist) and ICP RIE. The hardmask patterns are transferred into the diamond using directional etching. A second deposition of ~200 nm Si_3N_4 conformally coats the sidewalls, but is removed from the bottom of trenches using a short ICP etch. Unbiased oxygen plasma crystallographically etches the exposed diamond, while the sidewalls remain protected. Etching is continued until the desired undercut is achieved, resulting in free-standing structures. The crystallographic etch and it's remarkable properties are studied in detail in **§ 2.5.3**. This fabrication method was used to create diamond microdisks of ~1 µm thickness and ~7 µm diameter, with a faceted supporting pillar of ~4.6 µm. Optical characterisation reveals a loaded Q of $\sim 1.09 \times 10^5$. This fabrication

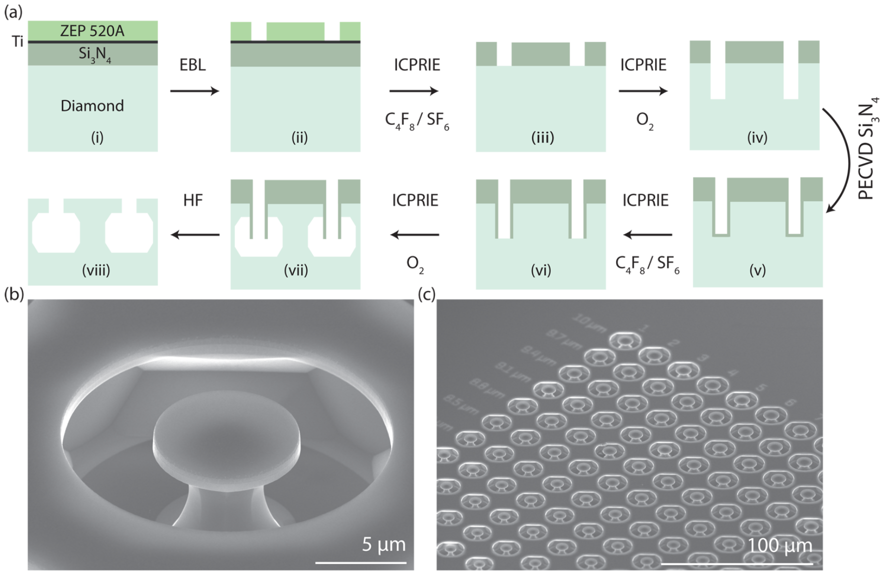

Figure 2.4 – Process flow for fabricating free standing single crystal diamond microdisk resonators using crystallographic etching. SEM images show the undercut and the sidewalls of the etched pit bordered by diamond crystal planes. The microdisk resonator stands on top of a faceted pillar, but the disk itself remains circular. Reproduced from [64].

process was subsequently improved on by Mitchell et al. [66]. The previously described process was optimized to reduce the pillar thickness supporting the microdisks, leading to pedestal waist thickness of less that 100 nm. While similar optical *Q* is reported like the previous work, a significant advancement is the observation of optomechanical backaction, discussed later in **§ 2.6.1**. After extensive process optimisation, *Q* was improved even further by a factor ~4 [67]. The authors investigated optimising the hard mask etching step, the anisotropic vertical diamond etch step, surface treatment and cleaning and the modification of the pedestal shape via an additional masking layer, which resulted in the observation of optomechanically induced transparency.

In a different trajectory, Mouradian et al. applied the crystallographic etching to fabricate nanobeam cavities in single crystal diamond [68]. In their work, the fabrication was carried out in a similar manner as described in [64], with the exception of using Al_2O_3 deposited via atomic layer deposition. This method is more conformal than PECVD, hence allowing the reduction of the thickness of the sidewall protection layer to 20 nm, which in turn enables the fabrication of smaller trenches. In comparison with the "angled-etch" method previously shown for nanobeam fabrication [61], these nanobeams have a rectangular cross-section. Optical measurements reveal an optical *Q* factor above 14 700.

The fabrication process for nanobeam cavities was subsequently extended to fabricate 2-dimensional photonic crystals as well by Wan et al. [69]. With a practically equivalent process flow, ~ 4 µm-wide, ~ 200 nm-thick planar slabs are fabricated, with optical cavities formed by designed defects in photonic crystal. The measured *Q* factor is 2670 to 6080 at 637 nm wavelength. Notably they demonstrate the simultaneous fabrication and release of photonic crystal slabs on the same substrate.

2.3 Diamond-on-insulator photonic platforms

The diamond-on-insulator (DOI) structure can be thought of as the analogue of the silicon-on-insulator (SOI) substrate, in this case diamond replacing the silicon device layer (not to be confused with silicon-on-diamond-type structures where diamond replaces the insulator layer). The structure consists of a diamond layer, on top of a low refractive index dielectric layer, for example silica, which is typically on top of a thick silicon handle layer.

A diamond-on-insulator photonic platform is a key technology for bringing the access to diamond light-matter interaction from laboratory to industry, enabling the industrial scale exploitation of colour centres for example for quantum information processing [70]. As with SOI, this technology enables the integration of passive and active structures in the same substrate, provides standard interfacing methods for fibers and can be packaged and integrated into larger optical and electronic systems.

The key component for fabricating a diamond-on-insulator structure is the thin diamond layer. For full control of the light propagation, the diamond layer has to be thin enough to support single-moded operation, in the scale of hundreds of nanometers of thickness. Since thin film supports the optical mode, the layer quality (absorption) and fabrication quality (sidewall scattering) of this layer is very important. In the following section different methods and their applications in literature are reviewed for creating this thin layer.

2.3.1 Diamond film growth

The most straightforward method of fabricating a diamond thin film on an insulating layer is the direct growth of diamond. The challenge for this approach lies in the production of a high quality thin film, due to the aggressive growth conditions for diamond and the difficulty of heteroepitaxy. In the subsequent section, the current state-of-the-art is reviewed for growing thin diamond layers on an insulating non-diamond substrate.

Fabrication of diamond-on-insulator structures were carried out by Wang et al. [71]. Nanocrystalline diamond film of 140 nm to 160 nm was grown on 1 µm thick SiO_2 on Si. The diamond film is patterned via a SiO_2 hardmask, patterned via e-beam lithography. Photonic crystal cavities are fabricated, with a Q factor measured as 585 at 631 nm. The same process was used to fabricate microdisks as well, which had a quality factor of ~100 [72]. FIB polishing was employed to smooth the sidewalls of the disks, but this didn't result in improved quality factors.

Rath et al. proposed the fabrication of such platform using a silicon carrier with silicon dioxide as insulating layer [73]. Diamond nanoparticles are coated onto the thermally oxidised (2 µm) silicon wafer to act as seed layer for the subsequent microwave-assisted CVD growth of a 600 nm microcrystalline diamond layer. The resulting layer is quite rough (R_q = 15 nm) with typical grain size on the order of 100 nm. Patterning is done with a thick HSQ e-beam resist and electron beam exposure, with pattern transfer using O_2/Ar chemistry. Ridge waveguides and grating couplers are fabricated and characterized. The propagation loss is measured as 5.3 dB mm^{-1}, with grating coupler loss being 5.0 dB at 1555 nm, with a 3 dB window of 50 nm. The grating coupler performance characteristics are comparable to ones achievable on classical SOI platforms. Using this platform, released slot-mode optical and optomechanical resonators are also fabricated [74], with an optical Q of 8500. Similarly, large diameter ring resonators are also shown, with a quality factor of $Q = 11000$ [75].

Improvements are demonstrated in growing the diamond layer by utilising an iridium buffer layer for growth by Riedrich-Möller et al. [76]. By engineering the lattice mismatch of the growth substrate (Ir/YSZ/Si(001)), the grown ~12 µm thick layer is single crystal diamond, even if rich in dislocations. To fabricate free standing membranes, the backside silicon layer is etched in windows using deep reactive ion etching. The buffer layers are removed via ion beam etching, and the diamond film is thinned, removing the lowest quality nucleation layers. Subsequently, FIB milling is carried out to pattern the layer into nanobeams and photonic crystal cavities. A final annealing at 1000 °C is carried out for 2 h in vacuum, followed by an acid treatment (H_2SO_4:H_2O_2, 1:1) and oxidation (420 °C, 2 h), to remove FIB damage. Q factors of 700 and 450 are reported for the nanobeam and photonic crystals, respectively.

2.3.2 Membrane thinning

Thin diamond films can also be fabricated by thinning down bulk crystals. Here the challenge lies in manipulating the thinned membranes and achieving uniformity and smoothness along the whole dimensions of the membranes. Recently, membranes as thin as 5 µm became available for commercial purchase [77, 78], which makes them an attractive starting point for many fabrication approaches.

Faraon et al. demonstrated a fabrication of a single crystal diamond-on-insulator type structure by thinning a 5 µm membrane [79]. The membrane was attached to a 2 µm thick thermally-grown SiO_2 layer on a silicon substrate. The membrane is thinned to 280 nm, then patterned using a Si_3N_4 mask and e-beam lithography. The hardmask is removed in a final etch that also removes ~300 nm into the SiO_2 layer. The fabricated microring resonators have a Q factor of 5000, limited by sidewall roughness.

Hausmann et al. starts the fabrication from a 20 µm slab [80]. Large diameter ring resonators and racetrack resonators are fabricated, with a measured Q of ~250 000. The transmission waveguide loss is estimated to be 1.7 dB cm^{-1}. This fabrication process was adapted for suspended structures later by the same group [81]. The diamond membrane is attached to a Si substrate for this work, before being thinned to ~250 nm and patterned via electron beam lithography and RIE. Nanobeam cavities are formed by the pattern, which are the undercut

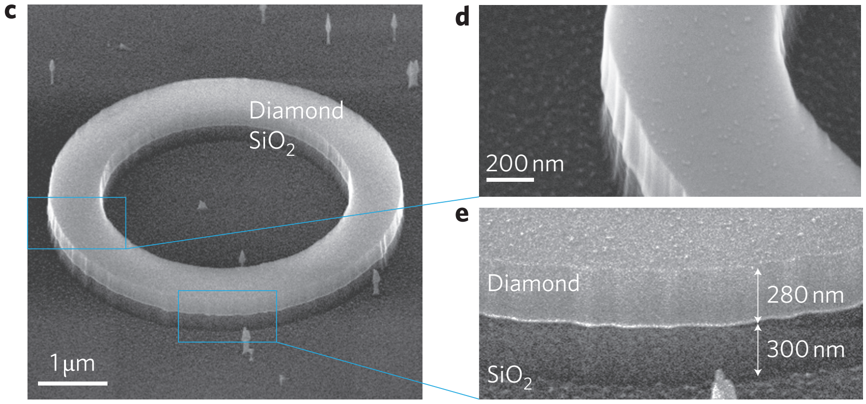

Figure 2.5 – Single crystal microring resonator fabricated via the membrane-thinning method. The insets highlight the sidewall roughness of the etched structures, as well as the transfer of the etch pattern into the insulator layer. Reproduced from [79].

and released by Si isotropic etching. Cavity modes are measured for the released nanobeams with Q factors up to ~ 6000. Two dimensional photonic crystal cavities are fabricated based on a similar process flow by Jung et al., attaching a thin single crystal diamond membrane onto a Si substrate [82]. In this work, the membrane is attached to a silicon substrate with windows via HSQ bonding, before final thinning to 264 nm. Focused ion beam milling is used to create the holes for the photonic crystal structure. The authors report a Q factor of 870 at 637 nm.

Similarly thinned membranes are used by Li et al. as well [83]. After transfer and thinning, Si patterned membranes are used as hard mask. The Si mask is fabricated from SOI wafers, enabling very high hardmask quality due to the single crystal nature of the material and the mature technology for Si microfabrication. Photonic crystal cavities were fabricated and characterized, yielding Q values of 4700 at 632.3 nm. This fabrication method was later used by Schröder et al. to fabricate 2D photonic crystals [84] with embedded Si vacancies, by local implantation via Si focused ion beam.

This platform is used by Gao et al. to fabricate integrated optics components [85]. The diamond membrane is thinned to 500 nm using Ar/Cl$_2$ plasma and patterned using electron beam lithography and Ar/O$_2$ plasma. Finally the samples are overcoated with 2 µm PECVD-grown SiO$_2$. The devices are then optically characterized, yield a waveguide attenuation of 2.3 dB mm^{-1}, a large improvement over the previous 6.5 dB mm^{-1} demonstrated by the same group in an earlier work [86]. The improvements are attributed to compensating for the wedge in the diamond membrane, along with smoother e-beam patterning.

Hill et al. demonstrated the integration of a thin diamond membrane with a Si photonic integrated circuit [87]. The membranes were thinned via ICP to 1 µm before bonded by drop casting onto the prestructured SOI wafer. Hybrid Si – diamond and Si – HSQ – diamond waveguides and resonators were fabricated via this method. The authors report ~ 30 800 for structures with HSQ and ~ 10 800 without.

Another method for obtaining a thin membrane via etching is carried out by Appel et al. [88], and subsequently improved on by Challier et al. [52]. The fabrication is carried out from thinly cut commercially available diamond plates with a thickness of 50 µm. The plate is sandwiched between a carrier wafer and a laser cut quartz cover slip that acts as the mask for the subsequent dry etch steps. The quartz mask's sidewall profile is engineered to have a strong retrograde profile (30°) to reduce mask redeposition and trenching effects. They report that these processes take less than 20 h to remove $\sim$ 50 µm of diamond, with the resulting membrane showing a uniformity of 400 nm to 800 nm, resulting in reliable fabrication of membranes down to 1 µm. Membranes of such thickness have the possibility of supporting well-confined optical modes if patterning is carried out. Similarly thinned membranes were demonstrated by Ali Momenzadeh et al. [89] and Pomorski et al. [90] using a diamond mask instead of quartz.

Membranes of suitable thickness can also be fabricated vertically [91]. In this case, reactive ion etching is used to mill many nanoslabs into the single crystal material, which can then be exfoliated and placed onto another substrate. While transferred slabs have been shown, devices have not yet been published using this fabrication method.

2.3.3 Diamond Smart-Cut

A promising method for achieving thin diamond single crystal diamond films employs a fabrication scheme similar to the SmartCut® process for SOI wafers.

The SmartCut® process employs high fluence ion implantation of H^+ ions into single crystal silicon [92]. The ions significantly damage the crystal lattice, but most of the damage is concentrated near the area where ions come to a stop (end of range). A second wafer, with a thermally grown SiO_2 layer, is bonded to the implanted wafer. Thermal annealing is carried out at 600 °C, which induces the blistering of the implanted region, forming H_2 and microcavities. The bonded second wafer acts as a stiffener during this step, suppressing the localised cracking of the layer, leading to full wafer splitting. The resulting surface is polished to specifications, removing the roughness caused by ion straggle.

Following the first report on achieving diamond membrane lift-off via implantation by Parikh et al. [93], there have been many publications investigating ion implantation induced graphitisation and using this phenomena to fabricate single crystal diamond membranes and membrane-based structures, which will be reviewed in detail in the following section.

An example of a successful implementation of the graphitisation - lift-off method for producing single crystal diamond membranes was carried out by Olivero et al. [94]. Following graphitisation caused by 2 MeV 1.5×10^{17} ion/cm^2 He^+ implantation, the layer was machined using 30 keV focused ion beam, creating micrometer-sized trenches. Afterwards the sample was annealed in 550 °C in air for 1 hour, for converting the damage layer to etchable amorphous carbon in the layer with damage exceeding the threshold and to anneal out ion damage

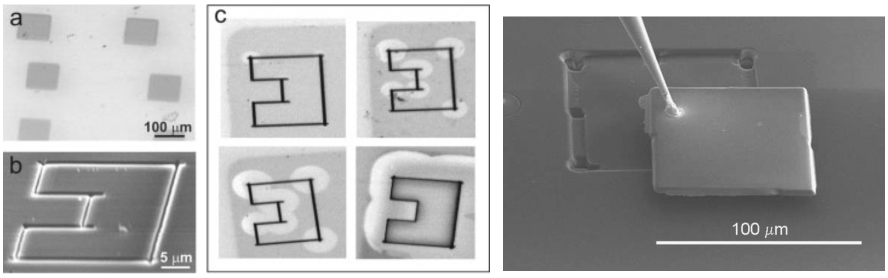

(A) (B)

Figure 2.6 – **(A)** Process flow for fabricating free-standing single crystal diamond devices using implantation and lift-off, followed by FIB patterning. Reproduced from [94]. **(B)** Single crystal diamond membrane fabricated via two-energy implantation and FIB-based liftout. The membrane is welded to a micromanipulator via localised Pt deposition. Reproduced from [95].

in the capping layer, where it didn't. The amorphous layer is then etched in boiling tri-acid etch. They remark that the now-exposed bottom surface of the single crystal capping layer is smooth ($R_a = \sim 2$ nm), attributed to the abrupt damage threshold. A final high temperature annealing (1100 °C, forming gas, 2.5 h) is performed to recover residual damage from both the initial implantation and from FIB processing. Cantilevers and suspended beam waveguides are fabricated, using diamond-air total internal reflection mirrors for coupling, machined during the FIB milling step.

In order to fabricate membranes thin enough to support single optical mode waveguides, Fairchild et al. proposed a two-energy implantation fabrication scheme [95]. The motivation behind the two energy implant is the difficulty of reducing the capping layer thickness to 200 nm without problems with strain induced cracking. Two implantations of He^+ are carried out with 1.8 MeV and 2 MeV, creating two amorphised layers, with a layer of ungraphitised diamond between. The authors observe that the graphitised layer corresponding to the second 2 MeV implantation is deeper than expected, likely because of the swelling caused by the first implantation, resulting in a 330 nm thick membrane. After annealing at 1260 °C, electrochemical etching is used to remove the amorphous carbon layers. FIB milling is used to cut a window into the capping layer, which is then lifted by bonding it via platinum deposition to a micromanipulator. This results in the thin single crystal diamond membrane remaining, supported at the edges. Further FIB processing is showcased to fabricate micro/nanostructures in the membrane.

A different approach for obtaining optical confinement was pursued by Wang et al. [96]. In their work, they employ low energy (180 keV), low fluence (2×10^{15} ions/cm^2) boron implantation to create the amorphous carbon. The capping layer is subsequently overgrown using MPCVD (300 nm). Structures are then formed by deposition and patterning of an Al/Ti hard mask layer using e-beam lithography (ZEP positive resist). Chlorine-chemistry (BCl_3/Cl_2) ICP is used to etch the metal layers, then O_2-based plasma is used to etch the diamond - amorphous carbon - diamond layers ~1.45 µm deep. Afterwards Ti/Al electrodes are patterned onto

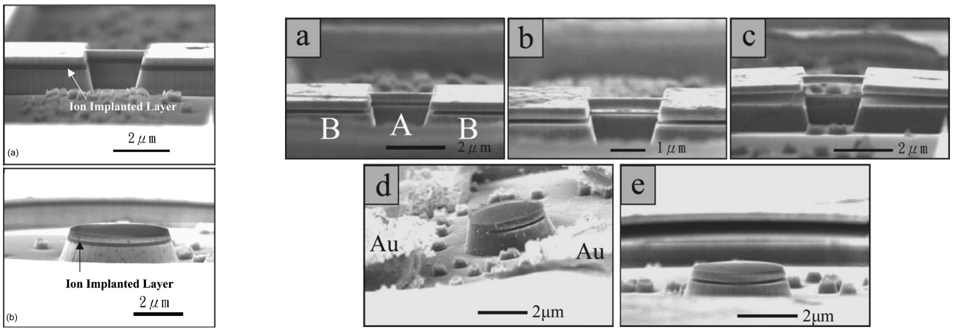

(A) (B)

Figure 2.7 – **(A)** SEM picture of implanted microstructures, the dark layer corresponding to the graphitised region. **(B)** Structures after local electrochemical release. Buckling of the structures after release indicate induced stress, a by-product of ion damage. Reproduced from [96].

the substrate for subsequent electrochemical etching. Deionised water is mixed with tap water (10:1), forming the electrolyte with a conductivity of ~80 µS. Voltages of 5 V to 10 V are used, with electrode spacing of 10 µm to 20 µm. The electrodes are arranged on both sides of linear structures (beams) and on four sides around circular structures (disks). It is remarked that a threshold voltage of 7 V to 8 V is required for the etching of the beam structures and 10 V for the disks, with a high 10 µm min^{-1} etch rate. The amorphous carbon is completely etched for the beam structures, and partially for the disks, leaving an amorphous carbon pillar. The finished structures were probed for optical modes, but there were none found (subsequent simulations showing that the 150 nm air gap revealed by removing the $\alpha - C$ does not provide optical isolation). SEM also reveals significant residual stress in the structures resulting in buckling after release (**Figure 2.7B**). This residual stress is attributed to the unannealed damage in the top device layer.

Hiscocks et al. utilises dry etching to fabricate ridge waveguides, achieving optical confinement using the graphitisation method with a single 2 MeV implantation and annealing [97]. The waveguide ridges (height: 1.5 µm, width: 3.5 µm) are defined using an oxide mask and photolithography, etched using oxygen plasma. FIB is then used to mill holes for the subsequent electrochemical release as well as 45° mirrors for coupling to the waveguides. The authors report successful multimode propagation in the waveguide.

Magyar et al. demonstrates the diamond lift-off process with an additional membrane thinning step, opposed to overgrowth of the membrane [98]. 1 MeV implantation of He^{+} was used to form the amorphous layer, which was annealed post-implantation at 950 °C for 2 h. The substrate was etched into 225 µm square mesas using oxygen reactive ion etching and then electrochemically etched. The mesas are detached from the bulk and were collected in a water droplet and transferred onto an oxidised silicon wafer via drop-casting. The membranes are transferred in both original orientation (initial top surface as top surface) and flipped orientation and then thinned using oxygen ICP plasma. The Raman signals are recorded from both membranes, showing reduction of the non-diamond signal from the flipped membrane where the etching removes the end-of-range damage, and unchanged for the membrane in the original orientation. This suggests that removal of up to 1 µm of the membrane enhances optical properties by removing unannealed ion damage. The resulting 200 nm thick membranes show strong luminescence and can be processed further into nanophotonic devices.

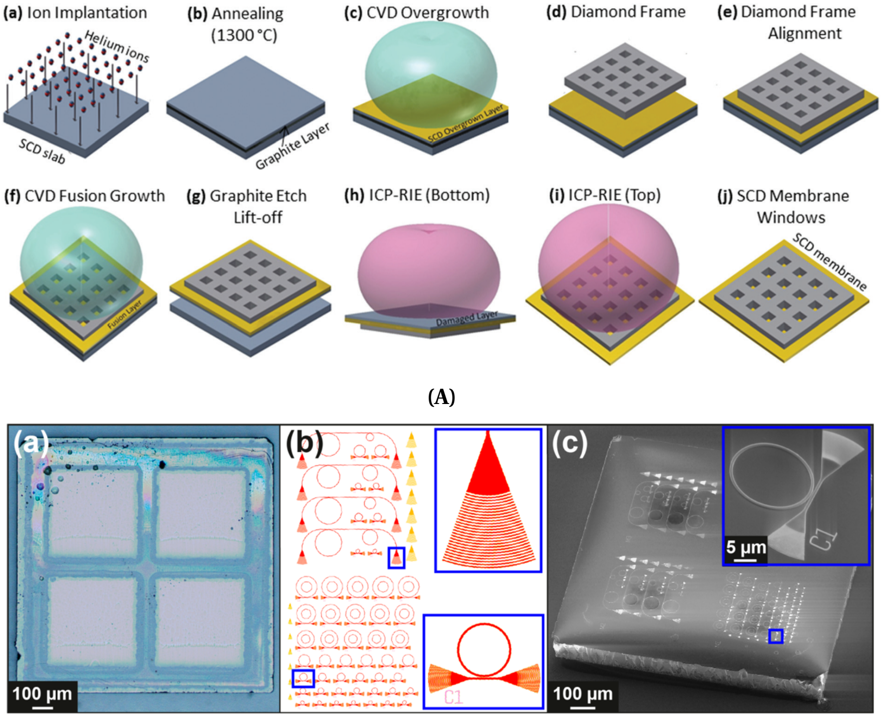

(A)

(B)

Figure 2.8 – **(A)** Process flow for fabricating SCD membrane windows using lift-off with a fused stiffener frame. **(B)** Fabricated SCD window substrate, with photonic devices fabricated on the platform. Reproduced from [99] and [100].

Piracha et al. shows an improved process flow for accessing and handling thin diamond membranes fabricated via the ion implantation lift-off technique [99]. Following the 1 MeV implantation, the substrate is annealed at ~1300 °C and overgrown using MPCVD. After overgrowth, laser cut poly- and single crystal diamond frames of 150 µm thickness are positioned on top of the substrates. Subsequently, the substrate - frame assembly is overgrown again, fusing the frames to the substrate. Electrochemical etching is used to separate the membrane from the bulk, followed by reactive ion etching on membrane side to remove ion damage. The membrane can be further thinned to the desired thickness, selected as 300 nm in the article. The authors carried out extensive characterisation of the resulting membranes, confirming high quality single crystal structure using Raman spectroscopy and the existence of luminescent NV defects using photoluminescence. This membrane fabrication technique was later extended to the fabrication of photonic devices [100]. The processed diamond membrane-frame assembly is glued to a carrier substrate using poly(methyl methacrylate) (PMMA), so that the frame is in contact with the adhesive. E-beam lithography is carried out with HSQ negative resist. Subsequently, the patterns are transferred into the membrane using a timed reactive ion etch, resulting in an etch depth of 380 nm. The resulting ridge-type photonic structures were characterised optically. They report a propagation loss of 7.2 $\mathrm{dB\,cm^{-1}}$ for the waveguides and a (loaded) Q-factor of 66 000 for the disk resonators. The authors comment on the possibility of the fabrication of fully etched structures on the platform by either using anchor structures or the augmentation of the membrane structure with a low refractive index material on the bottom side, such as PECVD SiO_2.

Bormashov et al. utilises the graphitisation-based lift-off process to fabricate large-area diamond Schottky diodes [101]. Low energy (450 keV) He^+ implantation is used to create the buried layer at 820 nm depth from the surface. MPCVD is used to overgrow the capping layer with boron doped diamond. Two layers are grown, the first heavily doped layer serving both as a source of holes during on-state and providing mechanical strength to the membrane during lift-off, and the second, optimally doped layer providing depletion in off-state. Electrochemical etching is used to remove the amorphous carbon layer and then the samples are annealed at 680 °C for surface termination. Schottky contacts are formed by depositing Pt on one side, and ohmic contacts are formed by depositing Ti/Pt/Au. The resulting diodes are characterized electrically, showing improved performance in almost all figures of merit versus diodes fabricated previously in 200 µm thick diamond substrates [102].

Bray et al. extends the fabrication shown in previously in [98] to engineer Schottky, p-n and p-i-n diamond junctions in single crystal diamond [18]. Boron doped single crystal diamond is implanted with 1 MeV He^+ ions to form the etchable layer ~ 1.7 µm below the top surface, which is then etched electrochemically. The membrane is transferred to a Ti coated substrate and thinned to ~200 nm. The device is characterized, showing rectifying behaviour due to the formed Schottky junction. A modified process is employed to fabricate p-n junctions. Following He^+ implantation, n-type diamond (P doping) is grown epitaxially (~200 nm). The transferred membrane shows diode-like behaviour with a high rectification ratio of $\sim 1 \times 10^4$, comparable to bulk diamond devices. Furthermore, the authors demonstrate p-i-n devices, by modifying the process to create an intrinsic diamond layer below the n-type layer. The intrinsic layer was grown in the presence of Si to form SiV colour centers. Electric characterisation shows diode-like behaviour for the p-i-n structure rectification ratio of $\sim 1 \times 10^6$, along with demonstration of electroluminescence of the SiV colour center.

As seen in this section, tremendous work has been invested in the diamond membrane lift-off process. To elucidate decisions taken in the fabrication section, the individual steps are examined in detail, namely the implantation and subsequent annealing step, the etching of the amorphised layer and the handling or bonding of the membrane for subsequent processing.

Implantation and conversion to etchable carbon

A key facet of the diamond material systems is the ability to host foreign atoms, which can form colour-centers with exceptional properties. Some of the most studied colour centers are the nitrogen vacancy center (NV) [16, 103–105] and the silicon vacancy center (SiV) [106, 107], but new centers are still being discovered.

The creation of these colour centers require the introduction of the foreign atoms into the diamond lattice, which can be done during growth [107] or via ion implantation. Ion implantation is the process of accelerating the dopant atoms to high energies and inserting them into the host material's lattice via bombardment. This process causes multiple effects depending on the material of the dopant and host, the angle and temperature of the implantation, the energy and fluence of the ions. The ion's path can be thought of as 'atomic billiards', as the ion collides with host atoms in succession, losing energy by each collision. These collisions can be classified into two phenomena: electronic stopping and nuclear stopping. During the first part of the ion's descent, the particle is too energetic for collisions and loses energy via electron-electron interactions or excitation/ionization. After sufficient energy is lost, the ion loses energy due to nuclear collisions in the material, leaving behind a high density of displaced host atoms, eventually coming to a stop [93]. The displaced host atoms leave empty lattice locations behind, known as vacancies. Vacancies can be thought of as pseudo-atoms, that can move in the lattice, if there is sufficient energy. At room temperature, vacancies are immobile. As a first approximation, ion implantation can be thought of as additively increasing the number of vacancies in the affected diamond region. This phenomenon of vacancy creation is also referred to as ion damage.

Diamond is a metastable phase of carbon [108]. Supplying enough disorder via ion damage and then performing providing energy in the form of annealing can change the phase into amorphous carbon [109]. The amorphous carbon phase has different properties from the diamond and these properties can be exploited for structuring. The first report on this phenomenon was by Parikh et al. [93], who identified the ion damage categorized into four regimes based on the ion-dependent fluence:

low fluence regime in this regime the ion damage is almost completely recoverable by post-implantation annealing

medium fluence regime the ion damage is not recovered by post-implantation annealing, a stable phase is formed

high fluence regime the implanted region is converted into an amorphous carbon phase by annealing

extreme fluence regime the implanted region spontaneously undergoes the phase transition to amorphous carbon without annealing

Both oxygen and carbon are used for implantation. The authors report that the fluence is an insufficient predictor for the threshold fluence for each regimes, but that the implantation depth has an influence, possibly due to the unconverted cap layer restricting the expansion of the damaged layer.

Locher et al. followed the same concept with oxygen implantation, but applied overgrowth, i.e. after implantation, a diamond homoepitaxial layer is grown on the implanted side of the substrate [110]. The aim of this overgrowth is to create a pristine layer of diamond that has no ion damage. They show via X-Ray and Raman study that the fluence of the implantation does not significantly alter the quality of the overgrown diamond layer. A similar procedure was carried out by Samlensi et al. [111], who performed ion channeling analysis using Rutherford Backscattering (RBS) experiments. They conclude that high quality single crystal film growth is possible after graphitisation treatment, without additional heat treatment post-implantation. Similarly to [110], they show that the template bulk diamond plate can be reused for repeating the membrane lift-off process to the same effect as the pristine diamond plate. Gippius et al. investigated the implantation of H^+, D^+ and He^+ species [112, 113]. While they remark that the behaviour of D^+ and He^+ are very similar, they observe the formation of hydrogen gas and island formation upon annealing when implanting with H^+. This gas formation can be seen as similar to the phenomenon during H^+ implantation into Si driving the Smart-Cut process [92]. The conversion to the graphite depends not on the fluence, but the level of radiation damage. Radiation damage depends not only on the fluence but also the implantation temperature, because the low temperature lessens the diffusion of vacancies. Implanted region swells, due to lower density, because of sp^2 bonds [114]. Molecular dynamics simulations show that cold implantation, followed by very high temperature annealing leads to a sharp $(\alpha - C) -$ diamond interface, which results in smooth diamond surfaces after amorphous carbon etching [115].

Membrane lift-off via hot implantation was demonstrated by Suk et al. [116]. Two implantations are carried out: a first hot implantation of 4 MeV C^+, and subsequently a room temperature implantation of H^+ at 380 keV, both targeting 2.3 µm depth. During annealing at 850 °C, the top diamond membrane self-cleaves, due to the formation of H_2 gas. The membrane has significant stress, and to prevent warping, a Ti layer is deposited before cleavage.

Bosia et al. proposes a numerical model for predicting structural changes induced by ion implantation [117]. Expanding on previous work on modelling the swelling caused by implantation [118], the authors derive a formula for describing vacancy density, which accounts for a saturation of defects. The vacancies are related to the decrease in density, and therefore, swelling of the material. The models were validated using 1.8 MeV He^+ implantation. Subsequent work carried out by the same group further refines these results [119]. Graphitisation is also being explored for microfabrication of microfluidics [120], surface micropatterning [121] and buried electrode fabrication for bioMEMS [122].

Quantifying ion damage

Depth-resolved or confocal **Raman spectroscopy** is a useful tool to quantify the ion damage of the substrate. Pristine diamond displays a single peak at 1332 $\mathrm{cm^{-1}}$ ("the diamond peak"), with no other peaks between 0 $\mathrm{cm^{-1}}$ to 2000 $\mathrm{cm^{-1}}$. Implantation produces a broadening and shift of the diamond peak, with the appearance of several other peaks, at 1445 $\mathrm{cm^{-1}}$, 1490 $\mathrm{cm^{-1}}$, 1630 $\mathrm{cm^{-1}}$ and 1680 $\mathrm{cm^{-1}}$ [123]. This study also reveals the evolution of these peaks during annealing, revealing a significant decrease of the peaks attributed to the amorphous carbon phase after annealing at 1200 °C, attributed to the annealing of the associated defects. The data reveals that the annealing behaviour depends on the depth where the defects are located - defects at the end of range anneal more completely than defects closer to the surface. Olivero et al. also reports the decrease in amorphous fraction both for 550 °C and 1100 °C annealing [124].

Photoluminescence can also help identifying the ion damage in diamond. Many defect centres are both luminescent and related to vacancies [125], allowing an indirect way of quantifying damage. Especially of importance is the GR1 defect center which is attributed to a vacancy in the neutral charge state (V^0). Many diamond samples also are naturally luminescent due to containing NV or SiV centres, the suppression of these signals can also point to lattice damage [57, 125].

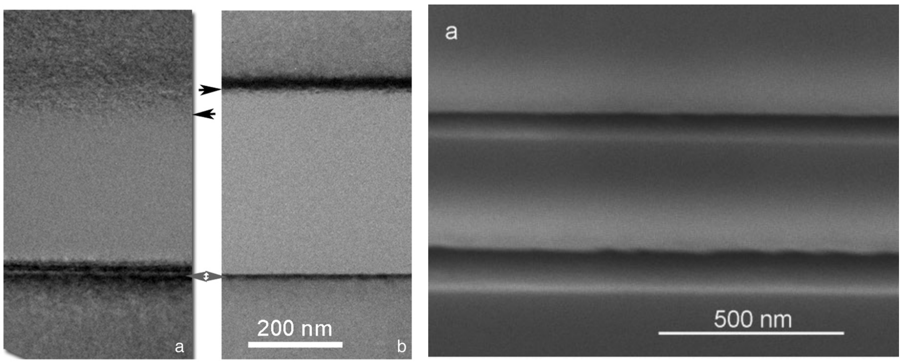

(A) **(B)**

Figure 2.9 – **(A)** Sharpening of the interface between amorphous carbon and single crystal diamond due high temperature annealing. The annealing facilitates the conversion of damaged diamond to amorphous carbon that has been implanted above the critical fluence and decreases the damage in diamond that received less. Reproduced from [126]. **(B)** Surface of diamond layers after removal of amorphous carbon in a two layer fabrication scheme, revealing a smooth, well-defined membrane. Reproduced from [95].

On the destructive sample testing side, **transmission electron microscopy (TEM)** can provide an extremely high resolution, if somewhat qualitative view of the implantation area. Furthermore, electron diffraction is a straightforward way of measuring the crystallinity of the material, allowing to measure the amount of crystalline and amorphous signal coming from the measured area. TEM also provides a precise measurement of the implanted layer depth and thickness, surpassing optical techniques where the depth of focus limits resolution to hundreds of nanometers. In a TEM study, Hickey et al. [126] investigated the implantation of Si^+ ions, below and above graphitisation threshold, with TEM cross-sectional imaging of the sample both post-implantation and after annealing. They observe the swelling associated with implanting and identify that the damaged layer is amorphous and not a graphite or diamond-like phase. TEM imaging also shows qualitatively the sharpening of the interface between the amorphous carbon layer and the crystalline diamond layer, along with the decrease of defect density, following the annealing step. For qualitative measurements, **electron energy loss spectroscopy (EELS)** has been used [127], along with **cathodoluminescence** measurement [128].

Transmission and absorption spectroscopy can also be used to measure the implanted layer, as some defects are absorptive [129]. Similarly, the refractive index contrast can be probed via ellipsometry [130].

Furthermore, **x-ray techniques** can be used to the measure the distortion of the lattice [119] or even identify individual dislocations via **x-ray diffraction topography** [128].

Amorphous carbon etching

As described previously, the highly irradiated diamond layer is converted into amorphous carbon ($a - C$). This layer has chemical contrast with diamond, which can be exploited to perform etching of this layer.

The first method used in literature is **chemical wet etching**. Graphite and amorphous carbon are very chemically resistant, but certain very powerful oxidisers are able to etch it. Some examples are hot chromic-sulfuric acid [93] and the "tri-acid" etch (HNO_3:H_2SO_4:$HClO_4$, 1:1:1) [94].

The second method relies on implanting **reactive species** into diamond, forming a volatile phase either during implantation or during annealing, thereby accomplishing separation of the capping layer from the bulk [93]. This method can be combined with supplying a reactive atmosphere during the annealing step [93] and exploiting the lower activation energy of the oxidation reaction ($C + O \longrightarrow CO_x$) for amorphous carbon than for diamond, but in this case, care must be taking that the diamond phase is not etched.

Amorphous carbon can also be etched using an **electrochemical etch** method. Marchywka et al. invented the method for etching implanted graphitised diamond layers [131, 132], based on previous empirical evidence of electrochemical oxidation of carbon materials [133]. The implanted sample is immersed into an low conductivity electrolyte, and high voltage is applied via electrodes. The authors demonstrate that no physical contact of the electrode with the implanted layer is required to perform etching. Platinum-iridium/platinum wires or graphite electrodes are used when a monolithic etching is performed, but the microfabrication of electrodes directly on the diamond substrate is also possible [96].

2.3.4 Diamond bonding

Bonding is the joining of materials in a permanent fashion. A variety of structures are enabled via wafer bonding (sensors, actuators) and it allows material combinations/thicknesses otherwise impossible via layer deposition. A complication faced when bonding diamond is the substrate size – commercially available single crystal diamond substrates are mostly chip-sized and techniques/equipment well adapted to wafers may perform suboptimally or not at all. This problem is present for other semiconductor materials, and there has been some work on reliable bonding of chip-size substrates [134, 135]. In the following section, different bonding techniques will be reviewed, along with demonstrations.

Metallic interlayer bonding Exploiting diamond's excellent heat conduction properties as heatsinks has been investigated for integration with active devices that are limited by power dissipation, like photodiodes and lasers. Metallic interlayer bonding is especially attractive for this application, as it is typically more forgiving of the bonding surface, one of which is typically already a high thermal conductivity metal heatsink, typically copper. An early work comes from Russell and Thomson, who fabricated avalanche photodiodes that were bonded via gold-gold thermocompression to a diamond cube [136]. Another option is to use solder to perform the joining of the active layers to the diamond, as demonstrated by Katz et al. using a gold-tin eutectic alloy solder [137]. Optimisation of the thin film stack on the submount and active device is required to prevent reaction of solder with the active layers and the failure of the bond [137, 138]. Similarly, deposition of bumps on the electrical contacts and subsequent flip-chip bonding was demonstrated for high performance photodiodes and ASICs [139, 140].

Interlayer bonding A thick organic interlayer can compensate for a highly textured surface (such as the waveguides fabricated in SOI), but still allows evanescent coupling between the two layers, therefore it is an attractive option for photonic heterogeneous integration, as demonstrated for bonding III-V dies to silicon circuits [141].

BCB bonding for free-standing diamond devices was also shown by Lebedev et al. with a complex thin film stack [142]. Nanocrystalline diamond was grown on a first Si wafer, followed sacrificial poly-Si deposition. A second Si wafer was oxidised, then metallised with Au/Ti. BCB is used as the adhesive layer, and the two wafers are bonded. Subsequently, the first wafer's Si bulk is completely removed by grinding and subsequent XeF_2 etching. The Au/Ti electrodes are fabricated on top of the NCD layer and the diamond layer is patterned. Finally, the poly-Si is etched in XeF_2, leading to free-standing NCD structures.

Spin-on glass can be used instead of an organic layer, which can increase the thermal budget of subsequent processing steps. Hydrogen silsesquioxane (HSQ) is a type of spin-on glass commonly used in microfabrication for e-beam lithography, but it can also be used for interlayer bonding. This is an organosilicon compound, where SiO_x groups form clusters bound to hydrogen ($[HSiO_{3/2}]_n$). Commercially available formulations of HSQ are spin-coatable liquid substances, but after solvent evaporation, it can be cured into a pure network of SiO_x. Bonding was demonstrated for attaching a diamond substrate to a Si window [82]. Thin diamond film bonding with an HSQ interlayer to an oxidised Si substrate was also shown by Tao et al. for nanomechanical resonator systems [143].

SiO_2 can also be deposited on diamond substrates via thin film deposition techniques. Bonding of ultrananocrystalline film diamond-on-insulator (UNCD diamond / SiO_2 / Si) stack to a thermally oxidised Si wafer was demonstrated by Bayram et al. [144]. To enable the bonding, 100 nm PECVD SiO_2 was deposited on top of the diamond layer. The PECVD SiO_2 was polished with chemical-mechanical polishing to smoothen the surface (resulting in a surface roughness of 0.45 nm rms). After rigorous cleaning of both surfaces, they are brought into contact in an wafer bonding system, in vacuum (1×10^{-4} mbar). During the bonding process a 10 kN force is applied to bring the surface into intimate contact and temperature is elevated to 550 °C, to increase the surface energy of diamond-oxide bonding. The authors report success with this technique, remarking on the necessity of densifying the PECVD layer to release trapped H_2 gas, that would form unbonded pockets.

Direct bonding Direct bonding or fusion bonding is a way of bonding two surfaces without the assistance of additional layers [145]. This bonding technique relies on getting the two mating surfaces in a very close contact, such as interatomic and intermolecular forces can keep the two surfaces together. The forces participating in the bonding determine the adhesion: van der Waals forces, hydrogen bonds, metallic, ionic and covalent bonds are all possible. While soft materials can be easily deformed plastically to bring into close contact, brittle materials will deform only elastically, which makes it more difficult to achieve good bonding conditions. The literature is rich on direct bonding of various brittle, semiconductor materials, especially silicon, which can serve as starting point for developing processes for diamond [146–149], for which there are comparatively fewer works. As Tong and Gösele [150] report, all materials that can form $H-F$, $H-O$ or $H-N$ bonds are potentially direct bondable. Diamond direct bonding was predicted by molecular dynamics simulations as well [151].

Significant research has been carried out into diamond-silicon direct bonding. This is motivated by the fabrication of SOI wafers, with the insulating layer being diamond, also termed silicon-on-diamond or SOD. Since diamond has higher thermal conductivity than thermally grown SiO_2, this could enable better thermal management of electronic and optical devices fabricated in the Si device layer [152]. It is also a good candidate for radiation-hardened SOI technology [153].

Polycrystalline diamond to silicon fusion bonding was demonstrated by Yushin et al. [152]. The diamond layer was deposited via MPCVD and polished to ~15 nm rms roughness. Bonding was carried out in high vacuum and and constant uniaxial stress of 32 MPa. Bonding was observed when the temperature during the process was above 950 °C. Scanning acoustic microscopy revealed that the fracturing of the diamond layer was found, increasing with fusion temperature, while XTEM revealed that the bonding interface of silicon and diamond was an amorphous interlayer containing significant amounts of oxygen. The formation of oxygen-rich interlayers is known for Si-Si fusion bonding. Similar experiments were carried out on highly oriented diamond (HOD) layers by the same group [154]. Here the amorphous interlayer was only observed near grain boundaries, whereas in areas without dislocations and sufficiently smooth diamond surface resulted in an abrupt Si – diamond interface. Notably the HOD layer used in this work has a roughness of 1 nm to 5 nm rms.

Besides a unique polishing method, Rabarot et al. demonstrated a thorough investigation of SOD substrate fabrication [53]. Even though the used CVD polycrystalline diamond layers were significantly smoothed, they are not yet smooth enough for direct bonding. To overcome this, a polysilicon bonding interlayer (0.5 µm to 1 µm) is deposited, which is then polished to 0.5 nm rms, to enable Si-Si fusion bonding. The Si surfaces are made hydrophilic via chemical treatment and annealed at high temperature (up to 1100 °C). The authors remark that since the diamond layer was encapsulated by the interlayer, no damage was observed due to the high temperature.

Surface activated bonding of Si and a single crystal plate was demonstrated by Liang et al. [155]. The as-received diamonds were repolished to a roughness of 0.82 nm R_a prior to bonding. The surface activation was carried out by Ar beam irradiation, before bringing the surfaces into contact. Partial bonding of the diamond substrate was demonstrated, attributed to non-uniform thickness of the diamond plate. TEM study shows a thin amorphous layer between the Si and diamond lattice, created by the Ar bombardment. The authors emphasise that the amorphous layer makes the bonding possible, as the layer can release the stress from lattice and thermal expansion mismatch between the two materials. Full bonding without voids based on this method was subsequently demonstrated by Koga et al. [156]. Liang et al. later demonstrated the bonding of single crystal substrates via Ar surface activated bonding to Si substrates [157]. The authors demonstrate high temperature stability of the bonded interface (1000 °C) and the bond withstanding a shear force of 300 N.

Nagata et al. demonstrated thin SiO interlayer bonding of nanocrystalline diamond layer grown on Si [158]. Chemical-mechanical polishing and sputtering was used to smooth the CVD-deposited SiO_2 layer to 0.2 nm. Surface activation is carried with O_2, N_2 and Ar gases, of which O_2 produces the largest bonded area (90 %+). Afterwards, annealing was carried out at 200 °C in vacuum.

Direct bonding of diamond has also been demonstrated for other semiconductor materials, where direct bonding of diamond can be exploited as a heat conductor located close to the active region. Sugino et al. successfully carried out bonding of p-doped polycrystalline diamond to GaAs [159]. The surface of the diamond layer was exposed to O_2 plasma, while the GaAs layer was rinsed with deionised water and placed in contact with the diamond surface. After 24 h of rest, the devices were characterised electrically, and the detection of photovoltaic phenomena indicates bonding and formation of a pn junction. Successful bonding of CVD polycrystalline diamond to AlGaN layers are reported, using a proprietary bonding method [160]. Other semiconductors are expected to be feasible to be direct bonded to suitable diamond surfaces, such as the demonstration of the bonding of ZnSe and sapphire to diamond [161].

	thermal budget	chip/wafer scale	optical properties	substrate requirements
metallic	-	+	-	+
adhesive – organic	-	+	+	+++
adhesive – SOG/HSQ	+	+	+	+
direct	+++	+	+++	-
van der Waals	+	-	+++	-

Table 2.1 – Qualitative comparison of bonding methods. +++ indicates excellent, or low requirements. + indicates suitable. - indicates poor or high requirements.

Van der Waals bonding Thin diamond layers can also be bonded via Van der Waals forces only. In these cases the diamond layer is thin enough that gap closing is not a problem, due to the thin layer's elasticity (**Eq.** (3.13), **Eq.** (3.14)). Such bonding was demonstrated using diamond membranes polished to 5 µm to 10 µm thickness [79, 80]. Membranes fabricated via the smart-cut method are also bondable in this fashion [98]. This method can produce well bonded sample, but require significant manual dexterity during the transfer/handling, as membranes of this thickness are extremely fragile.

Table 2.1 shows a qualitative comparison of the surveyed bonding methods for diamond bonding, for the aspect of optical integration.

2.4 Comparison of diamond photonic platforms

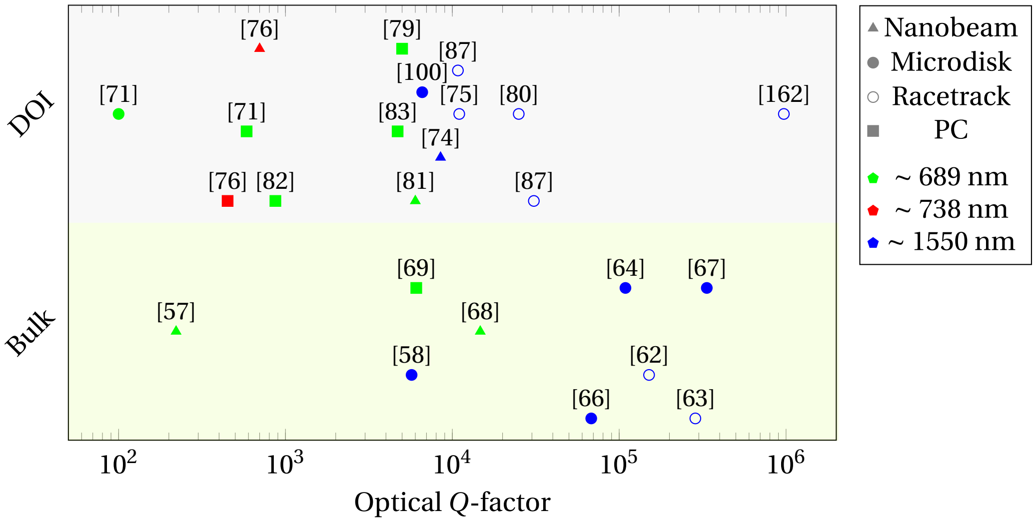

Figure 2.10 – Reported Q-factors of diamond optical resonators grouped by fabrication technique. The shape of the marker indicates resonator type, while the colour indicates the wavelength of operation. When multiple values were reported, the highest was taken. [DOI = diamond-on-insulator, PC = photonic crystal]

Bulk diamond micromachining has been used to demonstrate the highest optical quality resonators so far, using novel 3D machining techniques [61, 64], along with flexible, but less high quality serial focused beam techniques, such as FIB [58].

However these techniques share a limitation in the possibility of integration: either the realizable geometry is constrained, like in the case of crystallographic etching [64] or large scale photonic circuits are infeasible (focused beam). Integration with metallization or other layers is difficult, since the optical confinement arises from the waveguiding structures being etched out of the substrate, making subsequent depositions infeasible. However, the crystallographic etch process is commonly accessible in cleanrooms, requiring no specialized tools.

Diamond-on-insulator type platforms benefit from a close analogue of the SOI platform, which is extremely well studied and potentially adaptable to diamond. As demonstrated for Si, the integration of components (waveguides, resonators, couplers, conductors) is an achievable tasks.

Three general categories were shown for fabricating the diamond thin film part of the DOI structure. Direct growth of diamond on the insulator is the most straightforward method, but the grown layer will be polycrystalline in nature, which limits the achievable optical quality. While impressive results have been obtained in PCD [74], ultimately the material will limit performance.

Membrane thinning can be feasible alternative to growth, with several demonstrations of DOI structures. However, the thinning of the membrane is a significant challenge and the resulting membranes can display significant inhomogeneity [83, 87], which can hinder further processing. While it is possible to thin a membrane from a plate, most demonstrations use few-10 µm thick membrane for starting the fabrication. These substrates are expensive and difficult to handle and ship, due to their fragility. The thickness variation can also be significant due to the elastic deformation during polishing [87].

Diamond Smart-Cut, or implantation-based lift-out is a technique studied in detail for two decades now, but has been hindered by the ion damage the substrate sustains during implantation. However, optical resonators have been demonstrated [100], along with multiple mechanical resonators, that confirm that there has been significant progress towards eliminating this ion damage. The demonstration of electronics based on this method is another vote of confidence [18]. Although this method requires access to implantation facilities, the implantation and lift-off is a parallelisable and therefore scalable method, which is very promising for the industrial exploitation of diamond-on-insulator substrates.

Figure 2.10 shows a comparison of reported optical Q factors, separated into bulk and DOI-type fabrication technique. The operating wavelength and type of resonator is indicated to allow quick comparison.

2.5 Diamond etching

Due to the outstanding chemical stability of diamond and the high binding energy of C–C bonds, wet etchants typically cannot supply sufficient energy to break bonds and form etch byproducts. One known method of wet etching is to utilise molten salts, like KNO_3[163] or K_2CO_3 [164] at very high temperatures (600 °C+). In this case, oxygen from KNO_3 reacts with the carbon in diamond, resulting in chemical etching (with crystallographic anisotropy). However this method is extremely aggressive, incompatible with most cleanroom processes and difficult to carry out in a microfabrication environment, therefore rarely used. In the following section, some more commonly used etching techniques will be introduced, with their advantages and drawbacks.

While not the focus of this thesis, serial patterning techniques like laser cutting and focused ion beam milling are successful techniques for patterning diamond. The advantage of using FIB milling is the tremendous flexibility in etching 3D microstructures, demonstrated by the machining of nanobeams [57, 59], disk resonators [58] and solid immersion lenses [165]. The drawback of this method is the implantation of Ga^+ ions, which deteriorates the quality of the material [58]. The achievable geometries are also limited by the Gaussian nature of the ion beam [59]. Oxygen-based FIB milling can provide patterning without Ga deposition, but the damage range is ~ 10 times larger than Ga at 30 keV [166].

For fine milling, gas-mediated electron beam-induced etching can be an alternative FIB milling [167]. An oxidising precursor (O_2 or H_2O) can provide etching in the nanoscale, typically inside SEM or FIB/SEM system. The patterning follows the same serial concept as FIB, but the etch rate is lower and exhibits crystallographic selectivity.

Similarly, laser cutting can deliver high aspect ratio structures using femtosecond machining [168], but this method is limited to µm resolution.

A promising recently developed technique is dressed photon-phonon (DPP) etching [169]. Intense 325 nm UV light is used to dissociate an etching gas (in this case O_2), which etches the surface at protrusions, leading to a polishing effect.

2.5.1 Thermochemical etching

Crystal growth or thin film deposition can be thought of the opposite side of etching. This suggests that the high temperature growth process of diamond also has a counterpart of high temperature etching.

Shahin et al. demonstrated the structuring of NCD film via thermal etching [170]. Etching was carried out in a O_2 atmosphere, at 700 °C+ temperatures. Thick SiO_2 films proved to be the most effective masks against the etch. Vertical and lateral etching was demonstrated (mask undercut), with similar calculated activation energies. Exposing diamond to atomic oxygen has been shown to etch (1 1 1) and other facets, while (1 0 0)-oriented faces remained unetched

[171].

Another observed phenomenon related to high temperature is metal-catalytic etching. Metals with high carbon solubility (eg. Fe, Ni) deposited onto the diamond are capable of dissolving carbon into the metal, transporting to metal-air interface and desorbing it as gas. This technique is exploited as a form of polishing called hot lapping. Diamond patterning via this technique was reported by Ralchenko et al. [172]. Iron is shown as producing the highest etch rate, $8\,\mu\mathrm{m\,min^{-1}}$ which is significantly faster than typical plasma etches, but the etch does not produce a smooth surface. This technique can be used for nanopatterning by the use of nanoparticles [173]. In a more recent work, Nagai et al. also report extremely high etch rate ($8.7\,\mu\mathrm{m\,min^{-1}}$) for Ni catalytic etching [174]. The etch demonstrated for (1 0 0) substrates is strongly anisotropic, showing selectivity over crystalline planes. The authors also demonstrate polishing by applying the etch to a (1 1 1) diamond substrate.

2.5.2 Directional dry etching

Etching of diamond structures is also possible through directional plasma etching. In this case, the etching has a physical component, which is supplied by ion bombardment and a possible chemical component, where the ion species react with carbon atoms. The research into the structuring of diamond via dry etching concentrates on different aspects: etch rate, selectivity, verticality, sidewall and etch floor smoothness. There is significant empirical data available for different processes, which would be too long to list, but a few key studies and the chemistry used is shown.

Oxygen chemistry is very effective in removing diamond material [175] and is typically used as a high-etch rate processing step [88]. It can be effectively combined with argon for an increase in etch rate, at the expense of mask selectivity [176].

A drawback of oxygen/argon based etches is micromasking, i.e. the erosion, and subsequent redeposition of the masking material onto the etch surface, where it prevents the proceeding of the etch. To combat this effect, the chemistry can be altered to include a gas that chemically etches the masking material [177]. Due to the typical use of oxide-based mask, adding a fluorine-containing gas is an attractive option, especially since this gas is commonly available due to it’s use in Si micromachining [178]. Modifying the chemistry can also be used to alter the shape of the etched features [25].

Chlorine chemistry diamond etching has been reported to improve smoothness of the surface during etching, and has been used for polishing [52, 88]. Chlorine-based chemistries also exhibit a lower selectivity against typical particle contaminants (oxides) and against photoresist, which enables proportional etching, where low selectivity is desired [179].

A unique modification of the dry etching was demonstrated by Burek et al., where an angled Faraday cage was used to deflect the ion trajectories [61] (see **Figure 2.3**).

Hydrogen/oxygen (H_2/O_2) plasmas are selective over dislocations as demonstrated by Tallaire et al. [48]. Threading dislocations were etched faster than surrounding defect-free diamond, creating a characteristic inverse pyramid etch pits, with an XTEM study confirmed the presence of dislocations at etch pits. Similarly, high temperature etches combined with H_2, O_2/H_2 plasmas have shown to be exhibit selectivity over defects [47, 180, 181].

Ion beam milling is also possible for a purely physical etch [182], while ion beam polishing was shown by Mi et al. [46]. The drawback of ion beam patterning is the low selectivity of the process due to the small etch rate for diamond (an advantage for polishing applications however) and the resputtering of the masking material and diamond on the sidewalls (also called fencing). An interesting improvement can be the use of reactive ion beam etching with oxygen, demonstrated by Atikian et al. for the ion milling of free-standing structures [63].

2.5.3 Crystallographic etching

Some etch methods of crystalline materials are sensitive to the crystalline face being etched and exhibit a difference in etch rate for these faces. Such methods are extensively used in machining 3D microstructures from silicon [183] and are termed "crystallographic", to distinguish from directional anisotropy arising from ion bombardment typically encountered in dry etching. Silicon crystallographic etches are typically thought of as certain wet etch processes, like etching with KOH, TMAH and EDP. Notably, the exact composition of the etch bath and temperature has a strong influence on the plane selectivities [184]. Recently, dry etching was also demonstrated using thermochemical etching in Si, that exhibits a degree of crystal plane selectivity [185].

Crystallographic plasma etching was reported that was selective for dislocations [47, 48], but the real analogue of the Si crystallographic etching was first reported by Khanaliloo et al. [64].

The crystallographic etching is carried out in a standard deep reactive (ICP) ion etcher. The process is performed at high ICP powers and zero platen/bias power. This results in an almost thermal plasma (due to the missing ion acceleration) that is very dense (due to the high ICP power). In this sense, the etching performed is almost completely chemical in nature, thereby showing selectivity over the crystal orientation of the etched material. Some publications also utilise an elevated temperature to increase etch rate [64, 68]. Process pressure is also higher than typical dry etches for the same reason (15 mTorr to 22 mTorr), however etch rates are quite low ($<10\,\mathrm{nm\,min^{-1}}$) and non-linear for undercuts [64].

Further characterisation of this etch method was carried out by Xie et al. [186]. They found that with an increase of the bias from 0 W to 40 W, different crystalline planes can revealed for trenches in the $\langle 1\,1\,0 \rangle$ direction, starting from the $\{1\,1\,1\}$. Above 40 W, the crystallographic nature of the etch is no longer present.

This etching technique was employed with success to undercut nanobeams [68] and photonic crystal structures [69] as well.

2.6 Diamond MEMS and optomechanical devices

Diamond has excellent mechanical properties, which makes it an attractive material to fabricate micromechanical systems — or as Auciello et al. asks: "Are Diamonds a MEMS' Best Friend?" [187]. While the literature is rich with various diamond MEMS devices, like RF MEMS [187], bioMEMS [188], heaters [189], mechanical sensors [189], microfluidics [190], switches [191] and transducers [192], the discussion will be restricted to mechanical resonators.

Hemispherical polycrystalline diamond resonators were fabricated using a microfabricated glass mold, supported on a Si pillar [193]. Laser vibrometry is used to measure supported modes, revealing modes in the 100 kHz range, with quality factors up to $Q = 20\,000$ for the hemispherical resonator gyroscope mode of interest. In a later work, Saito et al. [194] demonstrates wineglass microcrystalline diamond resonators with a similar process, with quality factors up to $Q = 528\,000$.

Tao et al. fabricated diamond cantilevers with very high quality factors [143]. Single crystal electronic grade, single crystal optical grade, polycrystalline diamond and single crystal silicon cantilevers were measured using scanning force microscopy via an fiber-optic interferometer and compared. SC electronic grade cantilevers reach quality factors up to $Q = 1\,000\,000$ at room temperature, roughly 10-100 times as high as single crystal silicon, which has similar performance to the polycrystalline diamond cantilever. The authors also report that the quality factor is heavily dependent on the surface termination: O-terminated cantilevers outperform 10-fold the as-released cantilevers and F-termination also improving versus as-released, but only ~ 2-fold.

Naing et al. fabricated [195] electrically driven spoke supported ring resonators from microcrystalline diamond (and polysilicon). The authors also present a very comprehensive description of the resonator design, along with fabrication and characterisation. Resonators with a resonant frequency of 899.6 MHz (with $Q = 77200$) and 2970 MHz (with $Q = 42900$) were demonstrated under vacuum operation.

Free-standing doped-NCD beam, cantilever and disk resonators were fabricated and characterised via laser Doppler vibrometry by Lebedev et al. [142]. Q-factors are $\sim 1 \times 10^4$ for cantilevers and $\sim 1 \times 10^3$ for beams and microdisks. The authors identify the grain boundaries and doping as the cause of the observed low Q-factor.

Wu et al. used the graphitisation undercut method to fabricate cantilevers [196]. Long duration annealing was carried out after fabrication at 500 °C in oxygen atmosphere, which etches defects resulting from the implantation. Signficant improvement of the Q-factor was measured ($Q = 30\,000$ to $434\,000$) after 380 h, accompanied with a small decrease in frequency (70 kHz).

2.6.1 Optomechanical devices

Optomechanics, or cavity optomechanics is a branch of physics devoted to studying the interaction between light and mechanical vibrations. The first developments of this field was from the gravity wave detection community, with theoretical background laid out by Braginsky in the 1970s. Later, when the first experimental device with an optical microresonator coupled with mechanical modes was realized in 2005 by Rokhsari et al. [197] the interest in the field increased dramatically. In the spirit of brevity, only one application of cavity optomechanics (optomechnical oscillators), and one cavity configuration (whispering gallery mode) is discussed here, and from an engineering perspective — the reader is referred to the excellent treatise of the topic by Aspelmeyer [198] for an in-depth view on this topic.

For the optomechanical interaction to occur, the mechanical and the optical modes have to be located in the same place. This has spawned a number of different designs: beams, double beams, disks, and toroids. The creation of optomechanical device requires both good mechanical and optical performance. This requires designing a mechanical resonator with quality factor as high as possible, which supports a co-located optical cavity with a sufficiently high quality factor.

Optomechanical oscillators are of great interest for integration of frequency references [199], frequency comb generation [200] and sensing [201, 202] and have been fabricated from a wide range of materials, including doped SiO_2 (PSG) [203], SiN [204], Si [20], and $LiNbO_3$ [205].

Diamond optomechanical devices Demonstrating optomechanical behaviour in diamond is a challenge, considering the relative immaturity of diamond microfabrication and the strict requirements on the resonators. In general there are three variants of fabricated diamond optomechanical resonators, which are compared in the following section. In general, optomechanical behaviour improves by performing the experiment in vacuum (removal of air damping) and at cryogenic temperatures (removal of thermoelastic damping), but cryogenic and vacuum operation is undesirable outside of laboratory applications.

The first demonstration was done in polycrystalline diamond by Rath et al. [74]. Free-standing waveguides are fabricated by patterning waveguides in PCD, then locally etching the support SiO_2 beneath. Slot mode resonators are realized by closely spaced waveguides, which exhibit a mechanical quality factor $Q = 11\,200$ at 3.8 MHz. In a later work, this system is augmented with electrostatic actuation [206]. This allows for a direct measurement of the mechanical Q factor of the system, by applying a radio-frequency electrical excitation to the system and measuring the optical output power. Two mechanical resonators are fabricated per device in a Mach-Zehnder interferometer configuration: light is evanescently coupled to each mechanical resonator, with one resonator being electrostatically actuatable. A mechanical quality factor of 9600 at 13.8 MHz is reported.

Optomechanics was demonstrated by Burek et al. for devices fabricated using the "angled-etch" technique [207]. In this case, free standing one dimensional nanobeam cavities were used, with a triangular cross-section arising from the fabrication method. A highly confined electrical field is created by forming two guided-wave mirrors using elliptical holes in the beam, where it couples to mechanical modes (via moving boundary and photoelastic effects). A mechanical quality factor of 4100 was reported for a 5.52 GHz mechanical mode.

In a parallel trajectory, optomechanics was also demonstrated via the crystallographic etch-based diamond SCREAM process shown by Khanaliloo et al. [64]. The first method uses a suspended diamond nanobeam coupled to a tapered fiber to create the optomechanical cavity [208]. The authors report a mechanical quality factor of the order of 1×10^5 in cryogenic conditions for frequencies in the MHz range. Measurement of optomechanics was performed by Mitchell et al. for a microdisk system fabricated via the diamond SCREAM process [66]. A strong dependence of the mechanical Q on the support pillar diameter was observed, with clamping loss preventing the observation of mechanical resonances for pillars with a diameter larger than 500 nm. The best mechanical quality factor of ~9000 is reported for microdisks of 5 µm diameter with a pillar diameter <100 nm.

2.7 Diamond microoptics

Microoptics fabricated in single crystal diamond represent an inspiring endeavor, thanks to their exceptional material properties [209]. Diamond exhibits a high refractive index (2.4 at 635 nm [21]) and low absorption over a wide spectral range spanning from ultraviolet to far infrared. Furthermore, it provides high thermal conductivity, which reduces the thermal lensing effect [210] and a remarkably high laser induced damaged threshold (LIDT), 20 times better than fused silica [22]. These properties enable compact, high power laser components and spectrometers operating in the visible and UV range that are not accessible with other materials.

Although diamond microoptics requires microfabrication (opposed to ruled or molded gratings), microfabrication provides greater flexibility in patterning, gives access to a wide range of materials in addition to the typically employed grating substrates (quartz, plastic), such as silicon [211], gallium nitride [212] or gallium arsenide [213], and inherently enables surface treatments, such as distributed Bragg reflector (DBR) or anti-reflection (AR) coatings, in the same manufacturing environment. Current research efforts address the improvement of microfabricated gratings for astronomy [211], long-wavelength operation [214], microspectrometers [215, 216], external cavity lasers [217] and large-area gratings [218, 219]. In such applications, the extraordinary optical, mechanical and thermal properties of single crystal diamond are of high practical and functional value.

Another interesting application area for microfabricated diamond diffractive optics is for hard x-ray applications. Hard x-ray pulsed sources can output extreme power densities that traditional x-ray materials (gold thin film) are unable to handle. The high thermal conductivity coupled with low x-ray absorption makes diamond an intriguing material for these applications, even for extremely bright pulsed sources, like x-ray free electron lasers (XFEL) [220, 221].

2.7.1 Refractive diamond microoptics

Template-grown CVD diamond refractive lenses were demonstrated by Woerner et al. [222]. A template substrate was patterned with spherical impressions of 2 mm to 5 mm diameter and 4 mm to 7 mm curvature radius using grinding and polishing. A diamond film is deposited via MPCVD onto the patterned substrate. The growth side is then polished and the film is removed from the template. Individual lenses are laser cut from the film. Since the fabricated lenses correspond very well to the impressions in the template, very high fidelity of reproduction was achieved, corresponding to less than 1 % deviation from a perfect spherical surface.

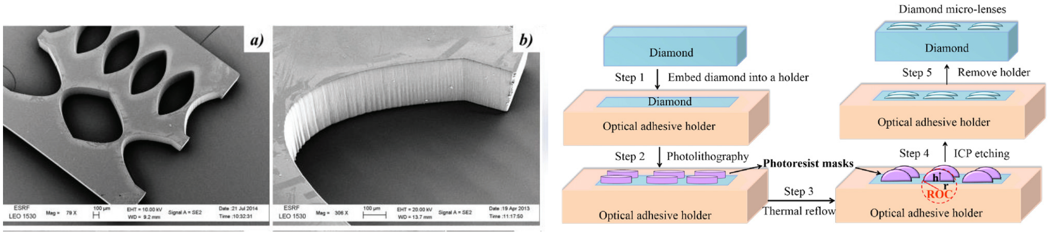

(A) (B)

Figure 2.11 – **(A)** Compound refractive lenses fabricated by laser cutting. Reproduced from [168]. **(B)** Process flow for fabricating microlenses via thermal reflow. Uniform spincoating of the small diamond substrate is achieved by embedding it into a holder. Reproduced from [223].

Polikarpov et al. demonstrates the machining of single crystal diamond lenses using laser micromachining [168]. Planar parabolic compound refractive lenses were fabricated with a frequency-tripled Nd:YAG laser (355 nm), while individual planar spherical lenses were fabricated using a pulsed picosecond Nd:YAG laser (1064 nm). The picosecond laser machining shows improved sidewall verticality and smoothness, compared to the UV laser, with rms surface roughness decreased from 1.3 µm to 1.2 µm. Parabolic two-dimensional lenses are also demonstrated with the same process, showing 5 % error from the design profile.

An effective technique for the fabrication of microlenses is photoresist reflow. Photoresist is spincoated onto the substrate, and then patterned to define the desired shape and volume of the lenses. A reflow step is applied, where the photoresist becomes liquid again, and surface tension changes the shape to be spherical. Subsequent etching transfers this pattern into the substrate, enabling scalable, reproducible fabrication of 3D shapes for lenses [179, 224, 225]. This technique was used to fabricate microlenses for a diamond Raman laser, where the diamond acts as a cavity and as the Raman gain material [10].

An example of such fabrication process is the work carried out for single crystal substrates by Liu et al. using reactive ion etching [223]. Photoresist thermal reflow was used to create the spherical photoresist patterns, which was transferred into the diamond by reactive ion etching using Ar/Cl_2, chosen for the low selectivity of this step (1:10), enabling large radius of curvature (13 mm or more), corresponding to a height of 1.7 µm. The lenses exhibit an extremely smooth surface of 0.18 nm RMS roughness. Zhu et al. later showed a similar fabrication process, where the reflow step was performed using solvent saturation [226]. Different solvents were investigated, which lead to different curvature, dependent on reflow time and solvent. This work was later extended to high fill factor (~90 %) microlens arrays using the thermal reflow method [227]. Polycrystalline diamond was used to fabricate microlenses by Karlsson et al. [228]. Since the etching scales the resist profile with the selectivity, the resulting diamond lenses are not perfectly spherical, but the error is small due to the shallowness of the lens. The phase error was measured with a Twyman-Green interferometer to be less than 31 nm, indicating high fidelity of reproduction.

To increase the height and curvature of the lenses, the diamond etching step has to be of higher selectivity. Since photoresists typically do not resist oxygen-based plasma chemistries that etch diamond effectively, a hardmask can be introduced. One approach was demonstrated by Li et al., where silica microspheres were used as a self-assembled hardmask monolayer [229]. The height of the resulting microlenses can be tuned by changing the selectivity or by changing the gas mixture. For the same goal, Zhang et al. use a transferred silicon hardmask [230]. Spherical caps are fabricated in an SOI wafer using the thermal reflow method, and are subsequently transferred onto the diamond substrate using pick-and-place. The selectivity of the diamond etch using SF_6/O_2+Ar can be tuned by changing the ratio of SF_6, with reported selectivities between 1:7 and 1:13.

The reflow method shown is only suitable for fabricating positive lens elements. For negative elements, Lee et al. demonstrates the use of hot-embossing [231]. Positive lenses are fabricated in a Si master using thermal reflow. Photoresist is spincoated onto the diamond substrate and the Si master is placed on top. The assembly is heated, causing the photoresist to soften, creating the inverse topography of the master, which is then transferred into the diamond substrate via ICP RIE.

The intriguing properties of diamond colour centers and the possibility of interrogation via optical means prompted research into the fabrication of diamond solid immersion lenses (SIL), to facilitate coupling of light into and out of various colour centers. The defect center is located at the centroid of the sphere defining the SIL, therefore all rays incident on the surface of the sphere are normal and suffer no refraction. This results in an increase of the numerical aperture by the refractive index of the SIL, in this case ~2.42.

Siyushev et al. uses a combination of laser and mechanical processing to fabricate a SIL of 1 mm diameter with a flatness better than 10 nm rms roughness [232]. The SIL confers a more than sixfold improvement in collection efficiency over an unprocessed surface, which is still below the theoretical maximum, due to imperfect alignment of the lens to the defect.

Hadden et al. utilises FIB micromachining to define SILs [233]. The lenses are situated in trenches, which further increases collection efficiency. The best SILs fabricated have an enhancement of ~10. The authors remark that SILs are also helpful with the excitation - the beam can be focused to a smaller volume due to the elimination of refraction, reducing the unwanted background fluorescence (improving the signal-to-noise ratio). Marseglia et al. demonstrates the automation of the fabrication of SILs over defects [234]. Marks are fabricated on the surface of the diamond substrate, that are registered by the confocal microscope, which identifies the defects. The FIB system aligns the data from the microscope to the marks, thereby accurately and reproducibly aligning the SIL to the defect.

2.7.2 Diffractive diamond microoptics

Diffraction gratings are key elements in the optical toolbox. A periodic change in the optical path length gives rise to interference, which can be exploited as a frequency selective element. Diffraction gratings are found in numerous optical systems, including monochromators [235], spectrometers [215, 216, 236], beamsplitters [237], continuous wave [217] and pulsed lasers [238]. These are commonly fabricated by mechanical ruling [239], where the grooves are created by mechanical material removal, or by microfabrication technologies based on photolithography and subsequent etching procedures [240].

Diffractive microoptical components are attractive to fabricate, even for a material system like diamond where the fabrication is less mature than conventional materials, like silica. Diffractive components work by exploiting interference - this means that the structures cause optical path length deviations comparable to the wavelength of the used light. Especially with a material with such a high refractive index as diamond, this requires machining only of small amounts of material (>1 µm for visible light). Coupled with the difficulty of machining diamond, this can mean easier exploitation of material system than for refractive structures. Furthermore, subwavelength structures can act as an anti-reflective layer, which can make up for the lack of material experience with optical coatings on this substrate. In the following sections, diamond diffractive microoptical systems and their fabrication procedures are reviewed. Where applicable, optical characterisation results are shown.

Fu and Ngoi fabricated diffractive elements in a polycrystalline 1.5 µm thick diamond film on fused silica using 50 keV Ga FIB milling [241]. The authors report a diffraction efficiency of 73 %, and remark that the fabrication of one DOE structure takes ~ 20 min.

Blazed diffraction gratings and diffractive optical elements were fabricated in polycrystalline diamond by Karlsson et al. [243]. Continuous relief structures were exposed by electron beam lithography, which were transferred into diamond using Ar/O_2 ICP RIE, with a selectivity of 1:10. The authors report a smooth transferred surface, but attribute most of the deviation from the theoretical diffraction efficiency to deviation from the ideal resist profile.

Diffractive structures are also very useful as anti-reflection layers in combination with other optical elements. A subwavelength periodic structure is formed, which acts as a modulation of refractive index, creating an index gradient between diamond and air, suppressing

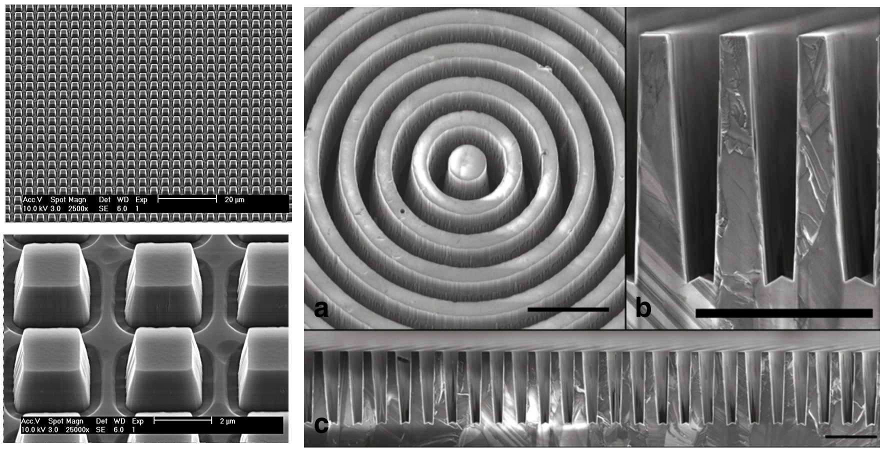

(A) **(B)**

Figure 2.12 – (A) Anti-reflective microstructures (moth-eye) fabricated in polydiamond for far-IR (10.6 µm). (B) Circularly symmetric half-wave plates, fabricated via a hardmask resputtering-based process to maintain sidewall angle with high aspect ratios. Scale bars are 10 µm long. Reproduced from (A) [228] and (B) [242].

Fresnel reflections in a wavelength-dependent way. To augment the fabricated microlens system, Karlsson et al. fabricated antireflection structured surfaces for the infrared spectral region [228]. Sputtered Al was patterned using e-beam lithography and etched using chlorine chemisty ICP RIE. The definition of the anti-reflection layer increases transmission from 71 % to 97 % when applied on both sides, for an illuminating wavelength of 10.6 µm (typical for CO_2 lasers). AR layers were also fabricated by Martínez-Calderon et al. using laser-induced periodic surface structuring (LIPSS) via femtosecond laser pulses [244]. Nanostructuring was carried out by pulsed laser light at different wavelengths, resulting in grooves of different morphologies. According to modeling carried out by the authors, these patterns can raise transmission by 12 % compared to an unstructured surface.

Diffractive optical elements (DOEs) are also very useful for shaping and transforming beams. Karlsson et al. demonstrates a binary DOE fabricated in polycrystalline diamond, designed as a fan-out element (16-way beamsplitter) [245]. Sputtered Al was patterned via contact photolithography. The diamond etch was carried in Ar/O_2 plasma, with an etch depth of 3.84 µm (for 10.6 µm operation) or 224 nm (for 633 nm operation). Uniformity error of 4 % is reported for red light.

High aspect ratio gratings were fabricated by Forsberg and Karlsson [242]. Thick aluminium is used as hard mask that masks against strongly biased Ar/O_2 plasma. The process employs multiple hardmask layers and pattern transfers to create the desired Al hardmask. A critical problem addressed with this method is the erosion of the mask layer during the aggressive diamond etch step. The hardmask geometry undergoes evolution during etching that leads to faceting, which accelerates the erosion due to the increased sputtering yield of the lower angles, eventually receding from the edges of the diamond bar. To combat this effect, the mask layer thickness is increased to 1.7 µm, which enables 13.7 µm deep grooves in the diamond. The article also elaborates on the bottom surface roughness as a function of initial hardmask geometry: it is observed that vertical sidewalls prevent micromasking from the resputtering of the hardmask. When the hardmask has become faceted, the redeposition occurs, but the etch floor is not longer in line-of-sight for the sputtered atoms.

The grating fabrication technique was subsequently refined by Vargas Catalan et al. [246]. Fabrication was carried out in polycrystalline diamond, with a hardmask stack similar to previous work [242]. Solvent-assisted microcontact molding is used to define the grating patterns in the hardmask stack. A Si master is patterned using e-beam lithography, used to fabricate a PDMS stamp. Photoresist is coated onto the diamond with the hardmask, and the stamp is positioned on top of the resist. The substrate is placed into solvent-saturated atmosphere (ethanol), which permeates the PDMS stamp. The PR softens, and fills the patterns in the stamp due to capillary forces, which is then used to pattern the hardmask and subsequently the diamond substrate. Optimisation of the etch parameters results in the control of the sidewall angle between 2.1° to 4.2°. The authors demonstrate greater control of the maximum etch depth by periodically resputtering the Al hardmask. Due to shadowing, the Al layer is thicker at the top of the groove, than at the bottom. A short etch is able to remove the mask material from the bottom of the groove, enabling the continuation of the etch process. An aspect ratio of 1:13.5 and a sidewall angle of 1.55° is demonstrated with this approach.

Half-wave plates are also demonstrated for the mid-IR by Delacroix et al. [247]. Subwavelength gratings were optimised to work in the N-band (8 µm to 13 µm). The design employs gratings of trapezoidal profile, that were optimised to be tolerant of fabrication errors. An antireflective grating was fabricated on the backside to decrease transmission losses. The fabricated structures show increased transmission compared to the original plate (89 % to 95 %), along with a retardance of $(180.08 \pm 3.51)°$ over the N-band. Similar fabrication was shown for quarter-wave plates by Forsberg et al. [248]. In addition, free-hanging gratings are fabricated in a polycrystalline diamond thin film on silicon. After the patterning of the diamond layer using ICP RIE, the underlying Si bulk is etched in a modified anisotropic Si etch, that undercuts the grating, leaving it free-hanging in a silicon frame. Crossbars were added to the grating lines to enforce buckling in the same direction. The authors note that a free-hanging grating can be advantageous in reducing transmission losses (no bulk Fresnel losses / no AR layer needed), a less demanding fabrication (without a large index substrate, the grating lines can have a larger period while retaining subwavelength properties) and better production scalability but the resulting devices are more fragile and difficult to handle.

Similarly microfabricated subwavelength gratings were demonstrated for coronagraphy (imaging of objects close to a star) [249]. Annular groove phase mask subwavelength gratings were fabricated for both near infrared (1 µm to 3 µm) and visible (400 nm to 700 nm), along with vortex phase masks with a topological charge of 4. An interesting technique shown in this article is the ability to tune the depth of gratings post-fabrication. To decrease the depth of the fabricated gratings, photoresist is coated, filling the grooves. Subsequent etching decreases the groove depth, due to slower etch of the PR at the bottom of the groove. Increasing the groove depth is performed by Al resputtering, similarly to previous work [246].

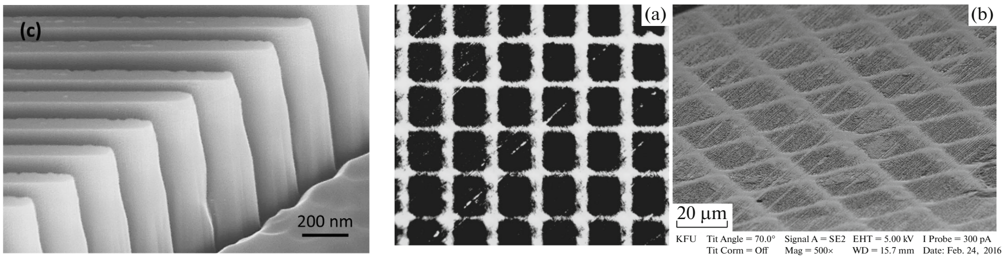

(A) **(B)**

Figure 2.13 – **(A)** X-ray diffraction gratings fabricated via e-beam patterning of HSQ and a chlorine chemistry etch. **(B)** Diffraction gratings fabricated via selective graphitisation induced via ion implantation. Reproduced from **(A)** [250] and **(B)** [251].

Another option for creating the periodic change in optical path length required to produce diffraction is to change the refractive index of diamond, instead of etching away material.

Such fabrication was carried out with ion implantation as a way of graphitising selected areas in diamond by Stepanov et al. [251]. Boron ions with an energy of 40 keV were implanted with a high fluence of 1.43×10^{18} ion/cm^2, masked by nickel grid with 40 µm square openings. SRIM [252] simulation indicates that the boron atoms are deposited in a ~100 nm-thick layer resulting in graphitisation due to the high fluence (see **§ 2.3.3**). The graphitised layer expands due to lower density of amorphous carbon ($\rho_{a-C} = 2.09\,\frac{\text{g}}{\text{cm}^3}$ to $2.23\,\frac{\text{g}}{\text{cm}^3}$) compared to diamond ($\rho_{Diamond} = 3.47\,\frac{\text{g}}{\text{cm}^3}$ to $3.55\,\frac{\text{g}}{\text{cm}^3}$) and the refractive index changes to $n_{a-C} = 2.1$ to 2.223, thereby creating the optical path difference.

An investigation into tungsten-relief and diamond-relief gratings for high energy hard x-ray diffractive optics revealed that the diamond gratings withstand a fluence of 59 000 mJ/¢m^2 at 8.2 keV, 118 times the amount measured for tungsten gratings before damage occured [253]. The damage manifested in the diamond gratings as unintended graphitisation. An innovative way of improving diffraction efficiency for diamond nanofabricated Fresnel zone plates were presented by David et al. [254]. The electron-beam lithography structured diamond structure was filled with Ir, deposited conformally via atomic layer deposition. The high density of iridium confers an increase in phase-shifting, while the diamond fins serve as an effective way of cooling the metal to prevent damage.

Microfabricated x-ray gratings are demonstrated by Makita et al. [250]. A 500 nm HSQ layer is used with a chromium adhesion/conduction layer 30 nm to create the grating patterns. The grating pattern is exposed via electron-beam lithography resulting in grating lines with 30 nm to 4 µm pitches. The etch process first transfers the electron-beam written pattern into the chromium using chlorine/oxygen chemistry, then transfer the pattern into diamond using an oxygen-based recipe. The HSQ layer is cured before diamond etching to increase recipe selectivity (300 °C, 40 minutes). The diamond etching is continuously tuned every 1 µm to

2 µm to maintain sidewall angle. The resulting structures have an aspect ratio between 10 and 20.

Continuing this line of research, suspended gratings were fabricated by Kujala et al. [255], somewhat similarly to the free-hanging gratings previously demonstrated by Forsberg et al. [248], on a suspended CVD diamond membrane attached to a Si frame. A diffraction efficiency map of the first order was measured, indicating an efficiency variation of 20 % across the whole grating. The variation is attributed to a non-flat diamond substrate, resulting in variation in the e-beam-written patterns due to focus error.

2.8 Conclusion

The interest in diamond microfabrication has seen a tremendous growth over the last decade, spurred by the commercially available and affordable high quality substrates. While the field is much less mature than the microfabrication of silicon (and it can be argued that it is more difficult), techniques are being developed that enable devices with surfaces and features that are comparable to the ones found for silicon. Nevertheless, it is clear that diamond does not compete with silicon and III-V materials for the choice of material photonic circuits, rather the aim is to enable new applications that can harness the material properties and colour centres of diamond.

3 Diamond-on-insulator platform

This chapter describes the motivation, design and fabrication of a diamond-on-insulator platform, from substrate preparation to patterning and release. Cleanroom processes are described in detail along with the characterisation of the steps, to enable reproduction of these results. The chapter discusses treatment of as-received samples for smoothness and flatness, the process and steps of creating a diamond-on-insulator substrate via ion implantation and membrane lift-off, the transfer and bonding of the membrane and finally the patterning and release.

Creating a single crystal diamond-on-insulator (DOI)) substrate involves producing a diamond membrane of suitable thickness (<1 µm) and bonding it to a substrate (preferably oxidised silicon, as in the case of silicon-on-insulator). As seen in the state-of-the art overview, several approaches are possible for manufacturing thin diamond membranes (**§ 2.3**). While the thinning approach seems attractive, thin diamond membranes are expensive to purchase, their thinning is not reliable enough for integrated optics applications (thickness variations up to 1 µm) and their handling is difficult. In contrast, the diamond smart-cut process can be applied to commercially available (thick) plates, which can also be reused for manufacturing multiple membranes. The so far demonstrated DOI processes relying on diamond smart-cut have a significant drawback: they require lifting off the membrane before bonding it [18, 98]. To overcome this drawback, the proposed process flow in this thesis uses die bonding to bond the still thick (therefore easy-to-handle) diamond plate before releasing the membrane.

The overview of the process flow for creating a diamond-on-insulator substrate and devices is shown on **Figure 3.1**, while subsequent sections describe individual steps in detail. The process is carried out on commercially available diamond plates (typical dimensions 2.6 mm x 2.6 mm x 0.3 mm). The as-received diamond plates then receive treatment to improve surface

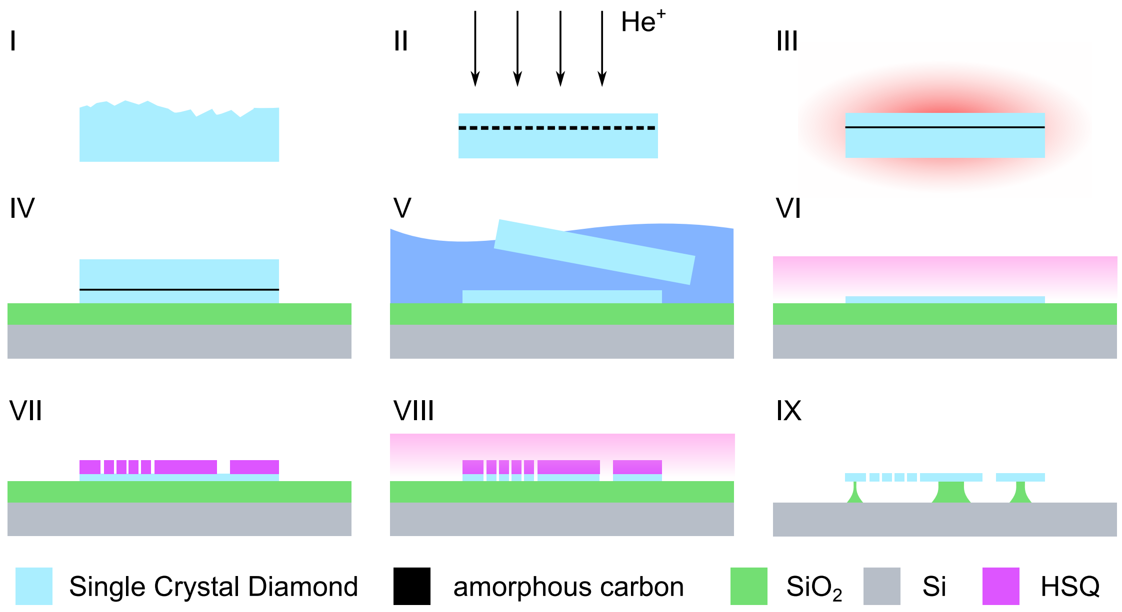

Figure 3.1 – Typical process flow fabricating a diamond-on-insulator platform and devices. **I**, Substrate surface refinishing. **II**, Light ion implantation to create buried damage layer. **III**, High temperature vacuum annealing to recover damage in cap layer and to convert damage layer to etchable carbon. **IV**, Bonding to insulator (SiO_2) on handle wafer. **V**, Carbon etching and bulk lift-off. **VI**, Diamond film thinning to target. **VII**, Device patterning via e-beam lithography. **VIII**, Vertical etch to transfer patterns into diamond. **IX**, Release of free-standing structures in vapour HF.

quality. The diamond is then implanted with light ions to create a highly damaged buried layer. The diamond is then annealed at high temperatures to recover the crystal structure of the cap layer and to facilitate the conversion of the damaged layer to an etchable carbon phase. While this was not in the scope of this thesis, at this point the diamond substrate can also be overgrown homoepitaxially, which creates a pristine diamond layer (optionally doped). Subsequently the diamond is bonded to a thermally oxidised silicon substrate. The amorphous carbon phase is etched, lifting off the bulk diamond piece. The remaining membrane is then cleaned and optionally further thinned to the desired thickness. The diamond layer patterned via photolithography or preferably e-beam lithography and ICP etching. Finally, for the creation of free-standing devices, the oxide layer is etched away in vapour phase HF, resulting single crystal diamond devices suspended on SiO_2 supports on a Si handle substrate.

3.1 Platform design

In this section, the DOI platform's thin film thicknesses are designed through the optical modelling of devices to be fabricated. For these simulations, finite element modelling is carried out in COMSOL Multiphysics.

The simplest type of waveguide in a DOI system is a rectangular waveguide. The waveguide

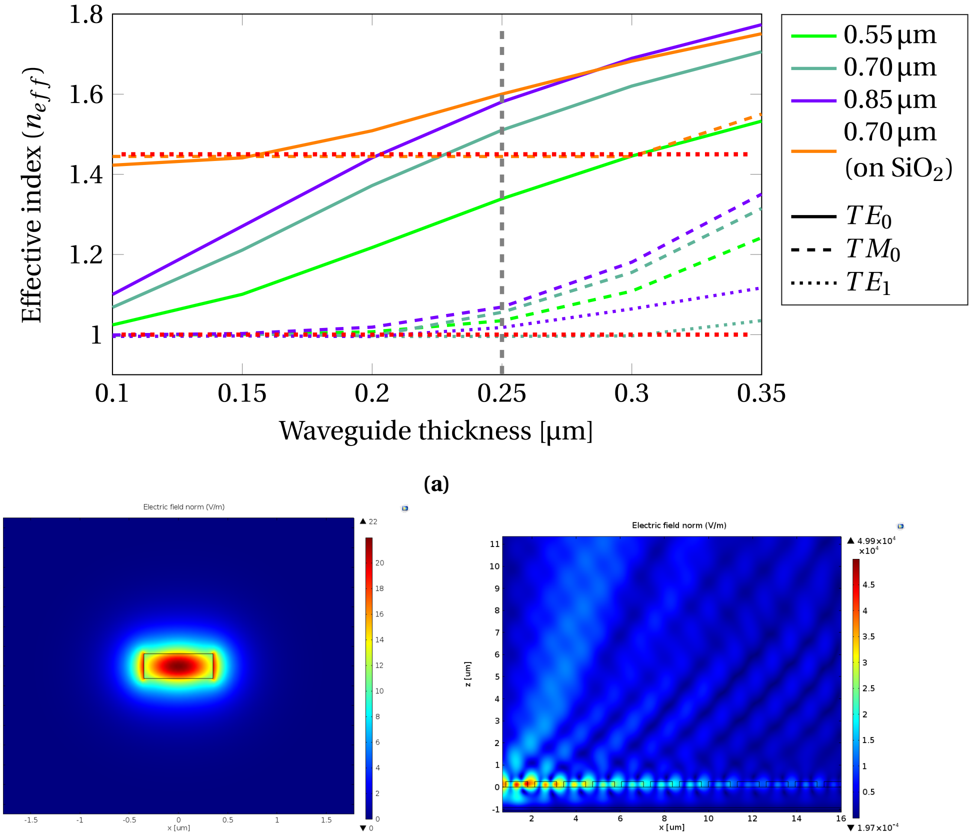

(a)

(b) **(c)**

Figure 3.2 – **a)** Mode analysis for a suspended single crystal diamond strip waveguide at 1550 nm wavelength. As the width and thickness of the waveguide increases, additional modes are allowed to propagate. The dashed vertical line indicates the design width, which ensures single mode propagation for widths up to 700 nm. Calculation results for a strip waveguide on a SiO_2 substrate is also shown, indicating that for 700 nm width and 250 nm thickness, the waveguide is still guiding and single mode. **b)** Waveguide cross-section with the electric field norm ($|E|$) plotted for the TE_0 mode. **c)** Electric field norm of the designed linear grating coupler. The light is propagates in the waveguide and is coupled out into free-space, where the overlap is calculated with fiber guided mode to determine efficiency (47 %).

is designed to ensure single mode propagation to control propagation characteristics. The single mode condition was determined by mode analysis of the waveguide cross-section using COMSOL, where single mode operation is shown by only a single mode having an effective refractive index (n_{eff}) above the surrounding media. **Figure 3.2a** shows the effective indices of modes for different cross-sections, both for a suspended and a strip waveguide on SiO_2. The horizontal dashed lines indicate cut-off for propagating modes. The dashed vertical line shows the chosen waveguide thickness of 250 nm, which allows single moded operation up to 700 nm width for both suspended and strip waveguide configurations (**Figure 3.2b**).

Other waveguide geometries are also possible, like the rib waveguide, which is frequently used for SOI platforms [256]. However due to the additional processing requirement (+1 lithography and etch), this was not investigated in this thesis.

To interface with the optical device on the platform, light needs to be coupled in and out. An advantage of a platform is that it is possible to define light circuits, that can be interfaced with using standard tools, instead of probing individual devices. Grating couplers allow high efficiency coupling to guided wave structures from fibers. A grating coupler was modelled and optimised using COMSOL and MATLAB for 1550 nm operation. The optimised coupler has a period of 1311 nm, 76 % duty cycle and a 937 nm air gap above the Si substrate (**Figure 3.2c**). The simulated efficiency for a linear coupler is 47 %.

3.1.1 Optomechanics

A device of interest on a free-standing diamond platform would be optomechanical devices. These devices can exploit the high stiffness of diamond to reach very high frequency of operation, which is beneficial for increasing the stability of frequency references. In this section, a brief introduction is given to optomechanics and finite element element modelling is shown for the design of optomechanical oscillators to show the feasibility of such devices in a diamond-on-insulator platform.

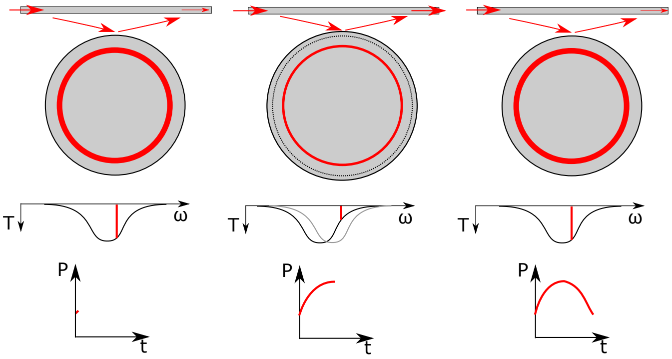

Figure 3.3 – Simplified illustration of the time-domain behaviour of optomechanical oscillation in a whispering-gallery mode resonator. The shift in the resonance of the cavity is induced via radiation pressure, which in turn decreases coupling to the resonator, shifting back the resonance. The periodic occurrence of this phenomena gives rise to a modulation of the incoming continuous wave light.

For the optomechanical interaction to occur, the mechanical and the optical modes have to be located in the same place. This has spawned a number of different designs: beams, double beams, disks, and toroids. The creation of optomechanical device requires both good mechanical and optical performance. This requires designing a mechanical resonator with quality factor as high as possible, which supports a co-located optical cavity with a sufficiently high quality factor.

If the parameters of the mechanical and optical resonators are known, the solutions for their coupling are known analytically for several resonator configurations. For a disk or a ring resonator with a whispering gallery optical mode and a radial mechanical mode, the equations governing the interaction are [257]:

$$|G| \approx \frac{\omega_{cav}}{R} \tag{3.1}$$

$$g_0 = G \cdot \sqrt{\frac{\hbar}{2 m_{eff} \Omega_M}} \tag{3.2}$$

where G is the frequency pull parameter, which shows how the resonant frequency changes by moving the boundary of the resonator and g_0 is the optomechanical interaction strength, which is a useful way of describing diverse optomechanical systems. Furthermore R is the radius and ω_{cav} the angular frequency of the optical whispering gallery mode and m_{eff} is the effective mass and Ω_M the frequency of the mechanical mode.

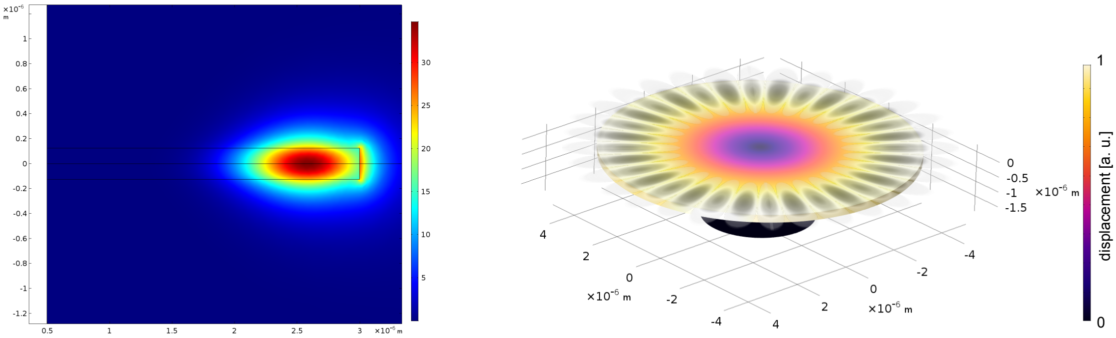

(a) **(b)**

Figure 3.4 – **a)** Profile of the whispering gallery mode inside a r = 5 μm diamond disk (azimuthal mode number $m = 17$). The optical resonance is at λ =1.51 μm. **b)** Mechanical radial mode of a r = 5 μm diamond disk supported on a 500 nm oxide pillar. Superimposed is the optical whispering gallery mode (in grayscale) inside the resonator to show co-located mechanical and optical fields. The radial mode is at 1.053 GHz, indicating gigahertz-range optomechanical oscillators are possible with this configuration.

The radius of the resonator has to be chosen sufficiently large, so that the radiative losses of the resonator (simulated here) will be smaller than sidewall scattering and absorption (**Figure 3.4a**). The mechanical properties of the resonator were modelled using COMSOL. The mode shown in (**Figure 3.4b**) has a frequency of 1.05 GHz, a quality factor of 1.34×10^5 and an effective mass of 6.3698×10^{-14} kg. Simulated optomechanical parameters of the resonator shown in (**Figure 3.4b**) has $G = 243\,\mathrm{GHz\,nm^{-1}}$ and $g_0 = 34.1$ kHz for 1550 nm operation, which means the power threshold for oscillation [203] (assuming a Q_o of 50000) is 231 μW, which is achievable is laboratory settings.

3.2 Quality of as-received samples

All processing were carried on commercially available diamond plates, sourced from different suppliers. For an integrated photonic platform, three main factors can be identified that govern the quality of the realisable structures: top-face roughness, sidewall roughness and absorption. Similarly, for microoptical structures the parameters are surface roughness, absorption, flatness and parallelism (especially for transmission-type devices). Absorption is primarily determined by substrate growth quality, while sidewall roughness is a product of the etching process and used material stack. Surface roughness, flatness and parallelism are primarily determined by the polishing regime employed. However this polishing can introduce defects in the top surface, such as polishing pits and create dislocations that extend below the surface due to the extreme mechanical stress. **Figure 3.5a** shows the schematic of the top surface of a diamond plate, along with the possible defects encountered.

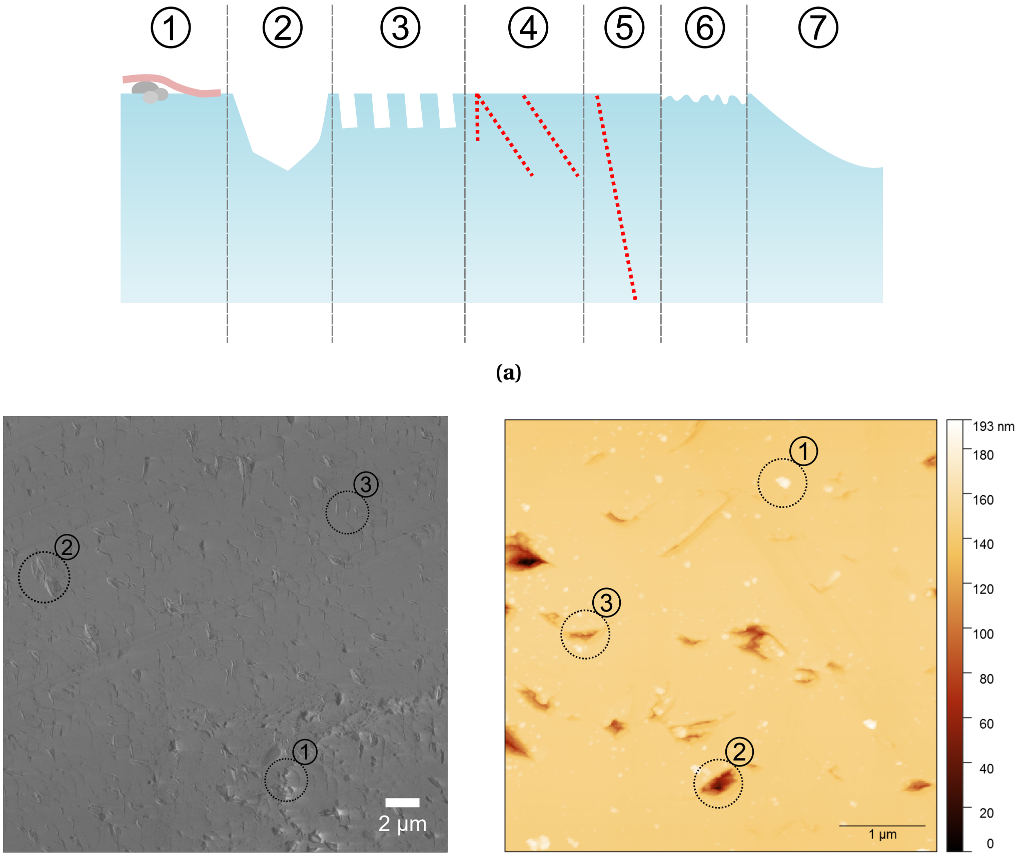

(a)

(b)

(c)

Figure 3.5 – **a)** Overview of defects in diamond plates. **1**, Surface contamination: slurry particles, organics. **2**, Polishing pits (up to hundreds of nm depth). **3**, Polishing tracks, shallow. **4**, Surface dislocations caused by contact polishing, extends few µm into the bulk. **5**, Bulk dislocations, caused by crystal growth. **6**, Surface roughness, set by polishing. **7**, Surface flatness / parallelism, set by polishing. **b)** SEM and **c)** AFM surface profile of as-received sample, showcasing surface defects **1**-**3**.

The strict requirements for producing high optical quality components show the need for high-quality diamond substrates. When as-received samples don't meet the requirements for the application, additional processing can be carried to improve the surface quality. As shown in **Table 3.1**, a number of diamond samples were tested to characterise the surface properties.

Sample	$\mathbf{R_a}$ [nm]	**P-V flatness** [nm]	**Defect density**
supplier #1, general grade	<30 (<1)*	150 to 500	high
supplier #1, optical grade	<5 (<1)*	100 to 200	high
supplier #2, optical grade	<3	100 to 500	low
polisher #1	<2	1000 to 1300	low
polisher #1, extra flat	<2	200	low
supplier #3, optical grade	<30	400 to 1000	low
supplier #3, mechanical grade	<30	600	low

Table 3.1 – Quality of as-received samples. Mean roughness (R_a) indicates datasheet specified values, except values labelled with *, which denote local roughness between defects measured via AFM. Roughness measurements are measured via AFM (Bruker Dimension FastScan). Defect density estimated via optical microscope and SEM. Peak-to-Valley (P-V) values are extracted from optical profilometry (Sensofar S Neox, Veeco Wyko NT 1100) data after removing a fitted plane. Supplier #1: Element Six, supplier #2: Lake Diamond, Supplier #3: Dutch Diamond, Polisher #1: ALMAX Easylab (samples polished: supplier #1 general grade)

While plates are typically smooth enough between defect pits, some samples exhibit large defect density (resulting in a large mean roughness). While pits only decrease bonded area, they reduce fabrication yield, especially problematic when large area photonic circuits need to be fabricated. Unfortunately, flatness is not a common requirement of diamond plates, and as such are typically not guaranteed by suppliers. Achieving a highly flat surface is a challenge, where scaife polishing mounting can greatly influence results. The tested substrates also display large variance in this parameter. From the table it is apparent that it is difficult to obtain substrates that are both flat and smooth at the same time.

In the following section the two approaches are described: improve the smoothness of samples that meet the flatness criterion (200 nm) (or smoothing) or improve the flatness of samples that meet the roughness criterion (1 nm rms) (or flattening), ideally in a way that preserves the other property during the process. These criteria are derived from the requirements for direct bonding (**§ 3.6**), but are also important for optics.

3.3 Ion beam polishing

Ion beam etching (IBE) is a physical dry etching method utilising a broad beam of accelerated ions. When using argon ions, the primary etch mechanism is sputtering. The advantage of using IBE is that all materials are susceptible to etching, allowing the machining of hard and/or chemically inert materials. The disadvantage of this method is the low selectivity across most materials (close to 1 : 1 for most material combinations) and the redeposition of sputtered material on the sides of the mask, leading to a phenomenon known as fencing. A property of sputtering is that the etch rate is sensitive to the incident angle of the ions due to a change in the deposited energy. The exact shape of the function of the etch rate versus angle ($ER(\alpha)$) depends on the material, but all are similar in that there is an increase in etch rate until a maximum and then the etch rate drops as the angle becomes grazing. This leads to the application of ion beam etching as a polishing method, since roughness (**Figure 3.5**) is characterized by high frequency height changes, which means large changes in surface angle, so the angle selectivity property can be exploited. On the contrary, flatness is difficult to improve as low-frequency, small angle changes will lead to only small differences in etch rates, which results in prohibitively large process times.

High angle ion-beam polishing (based on [46]) was carried out on diamond substrates. Substrates were cleaned in hot Piranha (100 °C, 30 min) and HF (concentrated, 15 min), before performing a substrate cleaning ion beam etch (Veeco Nexus, LOW, 10°, 15 min). This etch highly selective for diamond and can remove contaminations that remain even after wet treatment. Subsequently, high angle IBE is carried out (HIGH, 60°, 30 min). During the polishing, evolution of thin filaments are observed (**Figure 3.6a**), surrounded by pillar-like structures. The change in etch rate in the vicinity of the filament is attributed to crystallographic dislocations, based on the frequency and that there were no new filaments observed after repeating the etching process on the same sample (which would suggest micromasking). The filaments also withstand acids and show no material contrast under energy-dispersive x-ray (EDX).

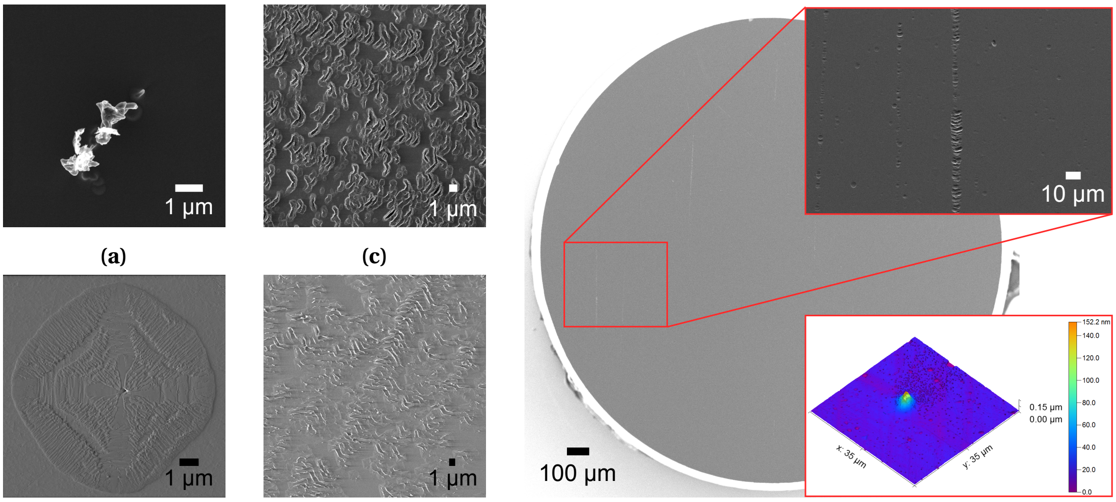

(a)

(c)

(b)

(d)

(e)

Figure 3.6 – IBE/thermochemical etching surface refinishing. **a)** Filament observed after high angle IBE polishing. **b)** Preferentially etched holes observed after thermochemical etch, attributed to dislocations. **c)** Roughening of as-received surface after 10 min and **d)** 120 min 750 °C thermochemical etch. The smoothness of the surface **d)** is not recoverable by IBE, due to the merging of the defect pits. **e)** Surface smoothed, optical grade, circular diamond substrate under SEM. Top inset shows magnified image: defect density is greatly reduced, some deep pits remain. Bottom inset shows AFM measurement of a remaining pillar-like defect.

For removing these features, a thermochemical etching step is performed before any IBE treatment. As seen in previous work, elevated temperature H_2 and H_2/O_2 plasmas preferentially etch dislocations [47, 48]. The samples annealed at 750 °C for 1 h show etch pits of similar density as the filaments (**Figure 3.6b**). After this heat treatment, further ion beam polishing do not reveal filaments. However, the thermochemical etch exhibits both crystallographic and isotropic etching, which results in a roughening of the original surface (**Figure 3.6c**), therefore the etch time is kept short (10 min) to preserve a surface that is still characterised by etch pits and therefore smoothable by IBE. Subsequent high angle IBE (HIGH, 60°, 30 min) removes the surface defects. The samples prepared this way show greatly reduced defect density, while preserving surface roughness, however the dislocations are not etched completely, as evidenced by column-like structures revealed during the IBE etching (**Figure 3.6e**). These structures have very small aspect ratios that make them unremovable by further IBE processing.

The shown polishing method of ion beam etching combined with thermochemical etching shows greatly reduced defect density, while preserving smoothness. However further processing is required to remove the small columnar protrusions that are observed, which are detrimental for direct bonding.

3.4 Substrate flattening via 3D printing

The idea for flattening the substrate is based on measuring the deviation from the ideal substrate flatness and correcting the deviation by etching the substrate by the difference between the measured profile and ideal flat profile.

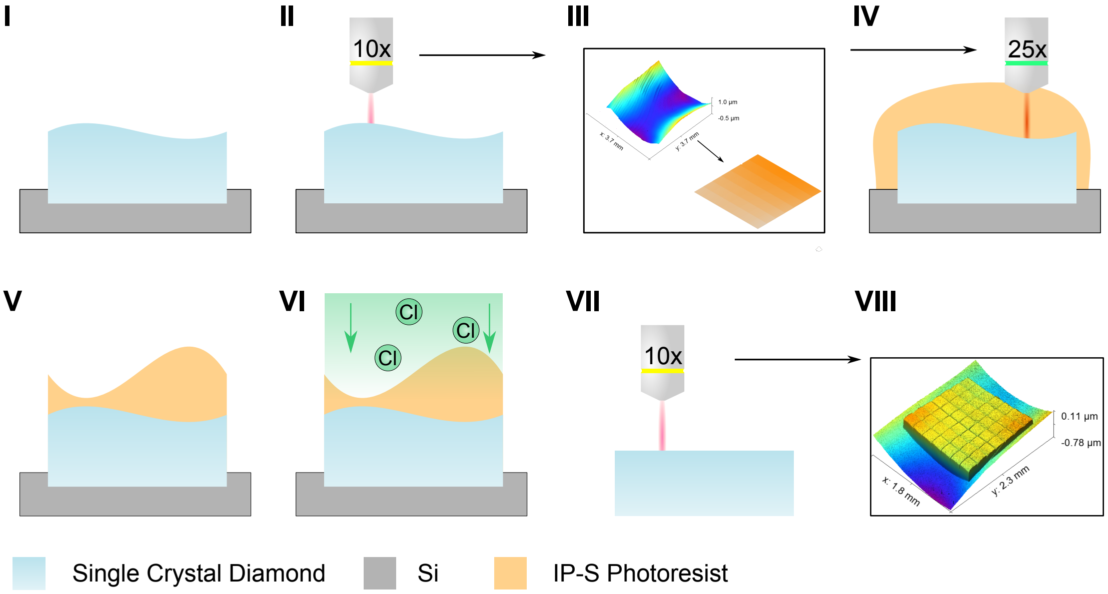

Figure 3.7 – Process flow for 3D printing-based flattening. **I**, Diamond substrate cleaning and attaching to carrier wafer. **II**, Initial surfaces is optically profiled. **III**, Height data is converted into complementary surface. **IV**, IP-S photoresist is dispensed and exposed in the NanoScribe system using a 25x objective. **V**, Resist development in PGMEA and IPA. **VI**, Cl_2-based ICP proportional etch. **VII**, Optical profiling of the flattened surface. **VIII**, Evaluation of the flattening performance.

For this method, there needs to be a characterization method that records the surface profile of the substrate, a patterning method that creates a layer that governs the amount of etching carried on each point of the substrate and an etching method that transfers the patterns into the substrate. The methods used and their alternatives are described in the subsequent section.

Optical profilometry is a fast, non-contact method to measure the topography of a substrate. Vertical Scanning Interferometry (VSI) or White Light Interferometry (WLI) uses fringe contrast to find surface height. The sample is scanned vertically through the whole height range, and the Z position corresponding to the maximum fringe contrast is recorded for each pixel. These maxima are assembled into a topography image of the substrate. The field size is determined by the magnification of the objective, but multiple images can be taken and stitched to create a composite image spanning multiple field-of-views. For optical profiling, a Sensofar Neox S system was used with the Nikon 10X DI objective in VSI mode. 3-by-3 fields are taken and stitched together to form the topography image. An image is taken of the topography of the carrier substrate to measure the tilt of the sample with respect to the carrier, since extending the scan range to cover the carrier degrades stitching accuracy and the stitched image has visible error.

The NanoScribe Photonic Professional GT is a tool for additive manufacturing using two photon polymerisation. 780 nm femtosecond laser light is focused to crosslink a volume of resist, with the required energy for crosslinking gained only when two photon are absorbed simultaneously. A single point of exposure forms a volumetric pixel, or voxel. The size of the voxel depends on the laser power and used objective. The exposure of complex patterns is achieved by moving the illuminated spot in X, Y and Z, forming a potentially 3D structure of exposed photoresist. Since the objectives have a working distance of ~300 µm, the substrates were sunk with respect to the carrier substrate to prevent accidentally crashing into diamond plate during movement. This was achieved using standard lithography and Bosch-process silicon etching **Figure 3.7**, etching square recessions of ~230 µm depth. The diamond plates are mounted in the holes using mounting wax (QuickStick 135). The carrier wafer is mounted into holder, which is loaded onto the Nanoscribe stage. The system is designed so that the holder is flat, and the holder being mounted onto the stage so that the tilt of the holder (and by extension, the carrier substrate) is zero with respect to the X-Y axes of the stage. The precision required in Z displacement of the writing requires the use of the piezo for moving the write head, and the large area writing requires the use of the galvo scanner. In this writing mode, a galvo scanner deflects the beam to provide scanning over the field of view of the objective, while the Z displacement is controlled by a piezo translating the stage. The writing proceeds in the X-Y plane line by line, then the Z coordinate is stepped (layer-by-layer writing).

Once the height profile is obtained via a profilometry method, it is converted into an exposure job suitable for the NanoScribe tool, applying corrections so that exposed surface matches the designed surface precisely.

First, the raw height data is treated using a scanning probe microscopy data treatment software (Gwyddion [258]). Binning (2x2) is applied to the height images to reduce processing requirements. The tilt of the substrate image is extracted as reference. The profile of the diamond chip is rotated to align the edges of the diamond plate with the $x-y$ axes, then the image is cropped to discard a small region along the edges where the profile is unreliable. Next, the tilt is extracted and removed from the profile. To prevent measurement errors and point-like defects influencing the writing, the image is low-pass filtered (2D FFT filter) with a radius of $2\,\mathrm{mm}^{-1}$. The image values are inverted and shifted ($v_i = -v_i + min(\mathbf{v})$), so that the image values are greater than 0. The maximum height value is recorded and the image is exported as a 16-bit TIFF image. For additional correction of the written data, the source image is further processed using image processing software ImageMagick [259].

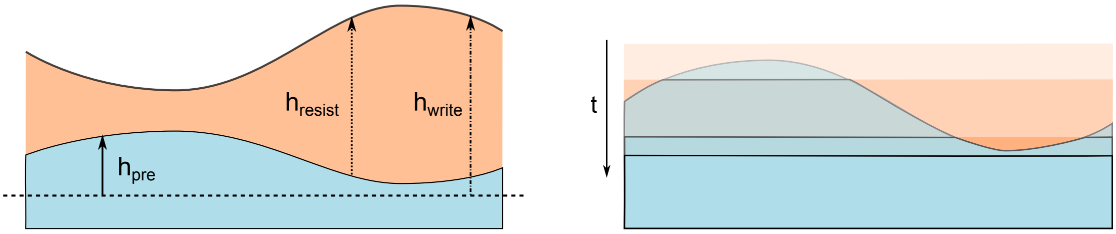

(a) **(b)**

Figure 3.8 – **a)** Schematic for determining the resist height to be written (h_{write}) based on the measured height (h_{pre}). The writing of the resist happens relative to a plane, with voxels written inside material lost, therefore the written height has to account for the original topography to arrive at a resist profile (h_{resist}) that is correctly scaled with the selectivity S of the proportional etch. Difference in the reference height (dashed line) for h_{pre} and h_{write} only results in a constant offset and therefore not a concern for the process. **b)** Surface evolution for a theoretical etch process which has a selectivity (S) of 1. In this case, the written height needs to be a constant value, to produce a flat surface result.

$$h_{write} = \left(1 - h_{pre}\right)\left(\frac{1}{S} - 1\right) + C \tag{3.3}$$

$$h_{resist} = \left(C + \frac{1}{S} - 1\right) - \frac{h_{pre}}{S} \tag{3.4}$$

$$h_{final} = S \cdot \left[\left(C + \frac{1}{S} - 1\right) - \frac{h_{pre}}{S}\right] + h_{pre} = S\left(C + \frac{1}{S} - 1\right) \tag{3.5}$$

The resist image is transferred into the diamond using a proportional etch, for which selectivity S is defined as ${}^{ER_{diamond}}/{}_{ER_{resist}}$, which will be typically smaller than 1 for most plasma etches. To account for this selectivity, the source image is scaled by $\frac{1}{S} - 1$, yielding a resist surface described by **Eq.** (3.3), of which the resist thickness is given by relating it to the original surface (**Eq.** (3.4)), which corresponds to scaling the resist by the selectivity and an offset (**Figure 3.8**). A constant height C is added to ensure the writing is always above the diamond surface. A constant height offset only changes the etch time required to completely etch the resist, but not the shape of the resulting profile. During the etch, the resist profile will be proportional to the diamond surface by S, leading to a final profile obeying **Eq.** (3.5), a constant (flat) surface. An example surface evolution is shown on **Figure 3.8b** with $S = 1$ to elucidate the validity of the calculations.

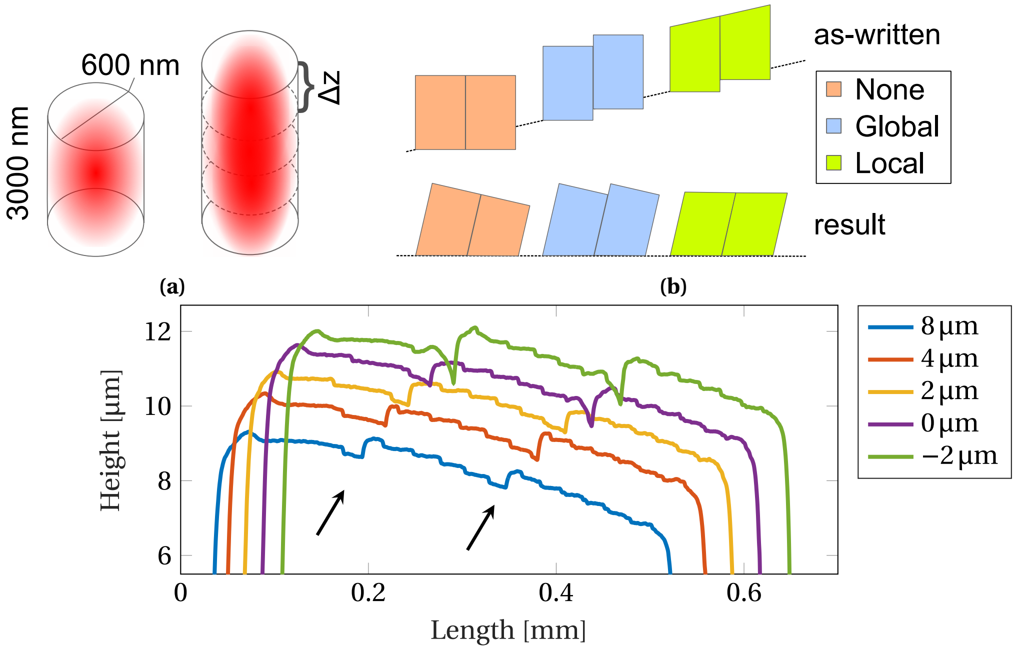

(a) (b)

(c)

Figure 3.9 – Improving writing performance. **(a)** Resolution in the Z direction is increased by overlapping voxels, making the effective resolution the overlap distance ΔZ. **(b)** Effect of tilt compensation. The top image show the written patterns for a tilted substrate, while bottom image shows the resulting resist structures with respect to the surface, highlighting the importance of performing both global and local correction to arrive at a flat surface. **(c)** Resist profiles of three adjacent fields, with different amount of overlap (negative overlap meaning separation). Arrows mark the location of the overlap, where a protrusion can be observed for overlapping fields, while zero overlap and separation result in a hole. Profiles have been offset for easier comparison.

The resolution of the written pattern depends on the voxel size, which in turn primarily depends on the used objective. For this particular application, it is desirable to have large X-Y voxel size to decrease writing time (low X-Y resolution), but high Z resolution for smooth written features. To increase vertical resolution, voxels are overlapped (**Figure 3.9a**), leading to structures that combine fast writing with high Z resolution, allowing the use of the 25x objective. A ΔZ of 150 nm was used to expose the structures.

The image is split up into square fields based on the field of view of the objective ($a < 300\,\mu\text{m}$, chosen size is 200 µm). No overlap between the fields results in a trench developing between fields, due to the shrinkage of the resist (**Figure 3.9c**), while overlap results in a protrusion with a height related to the number of layers in the overlap area, due to increased ambient dose. The structures are exposed without overlap to prevent protrusions, since protrusions are detrimental for bonding surfaces.

The tool uses an autofocusing system based on Zeiss Definite Focus II, but it is not reliable when multiple optical interfaces are present (such as resist-diamond-resist/air/QuickStick/silicon), resulting in either the system not focusing, unpredictable shifts of focus versus the resist-diamond interface or focusing on the silicon surface. The accuracy of the focusing is limited to approximately ~1 µm, which is not feasible when the exact height is required to be written. Since profile data is available of the height, a manual focusing and tilt correction scheme is used.

The piezo can address coordinates between [0, 300] µm, thus the focusing is performed by resetting the piezo, then moving to the lowest corner of the diamond and moving the objective to focus (setting $Z_{piezo} = 0$ at the lowest corner). For subsequent fields, to prevent structures to be written either inside the substrate or above it due to substrate tilt, the written data is offset in Z by the piezo (global tilt correction) based on the measured tilt of the plate (calculated via subtracting the plate tilt from the carrier tilt). Additional compensation of the pattern is applied for the tilt of the substrate. Since the aspect ratio is very small, the projection of the written pattern to the actual surface is approximated as a plane offset – shear is neglected. The tilt of the substrate is extracted as a plane given by a_x, a_y, a_{xy} $(P = a_x \cdot x + a_y \cdot y + a_{xy} \cdot x \cdot y)$ and a gradient is generated with a matching slope and added to each field (local correction). Then each field is offset based on the global position, to match the bottom of the field to the diamond surface (global correction). **Figure 3.9b** shows the effect of correction: uncorrected (pink) structures waste time writing inside the substrate and produce an error proportional to the tilt. Global correction reduces wasted time and the error is reduced, but the profile is discontinuous. Applying local correction on top of global correction results in a continuous, flat profile.

The written height has a non-1:1 relationship with the programmed height, likely due to using a high overlap during writing, which causes exposure of the resist outside of the voxel. Since an offset in the resulting structure height does not influence the flattening process, only the linear scaling factor is identified, which is ~0.75 for 150 nm ΔZ. It is important to note that this linear scaling is not an error of the piezo translation, therefore the manual focusing and tilt correction offsets must not be corrected with this factor. It is expected that the choice of ΔZ influences the value of this scaling factor.

The data for writing is generated from each pre-distorted image, converted via the Describe command-line mode. The height data is discretised into equidistant levels that are constant across fields to prevent steps and assembled into a field-by-field writing program. A sample writing program [260] and the code used to generate it [261] is available.

Photoresist (IP-S) is dispensed onto the diamond plate and the wafer is loaded into the machine. Manual focusing is performed according to the previous description. Once the exposure is completed, the resist is developed in PGMEA for 17 min and in IPA for 5 min. The resist layer profile is measured back to ascertain exposure fidelity via mechanical profiling (as optical profiling can be unreliable due to multiple reflections occurring at the air-resist and resist-substrate interfaces and due to the possibility of discontinuities/high angles surfaces in the resist). Transfer of the resist pattern into the substrate is performed by deep reactive ion etching. A chlorine-based recipe is used (STS Multiplex ICP, 800 W coil power, 300 W platen

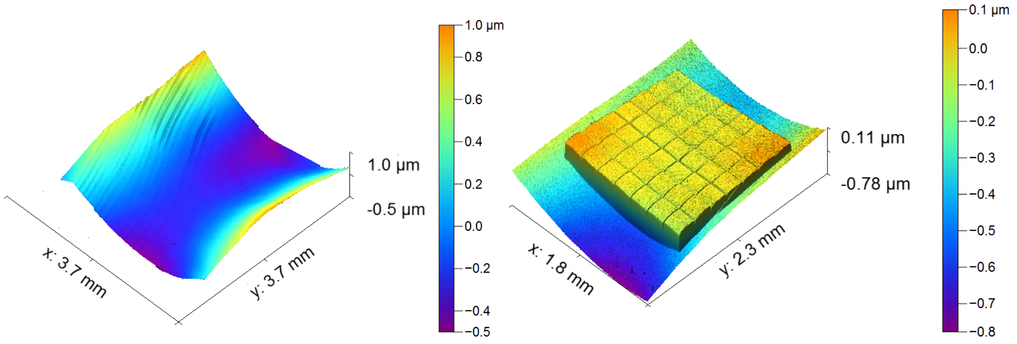

(a) **(b)**

Figure 3.10 – **(a)** Surface profile before and **(b)** after flattening process, measured via interferometry. On the central area, where patterning was carried out, the peak to valley flatness is better than 100 nm, corresponding to a ~4 fold improvement over the same central area.

power, 5 mTorr chamber pressure, 40 sccm Cl_2 and 25 sccm Ar, etch rate 64.5 nm min^{-1}), which provides low selectivity ($S = 1:15$) and smooth surfaces [179]. 150 nm ΔZ steps are transferred as 10 nm steps in the resulting surface. The etching time is not critical and is chosen to ensure that all resist is etched away. Optical profiling and AFM is used to characterise the resulting surface, shown on **Figure 3.10**.

A better than 4-fold reduction of peak-to-valley topography has been achieved via 3D printing based flattening, resulting in a P-V flatness better than 100 nm on a 1.4 mm × 1.4 mm area. Currently this figure is limited by the precision of the identification of the linear scaling factor and etch selectivity, and can be improved further. The processed diamond surface may have added roughness compared to the unprocessed one: the noise of the piezo drive is superimposed upon the resulting surface, multiplied by the selectivity (S), along with a stepwise discontinuity arising from the layer-by-layer writing process. In practice, the smoothing property of the etch significantly reduces this effect, and the low selectivity transforms steps into slopes (**Figure 3.11b**). Ideally, the piezo could be driven directly with tilt compensation signal, instead of discretising, which would eliminate the stepwise discontinuity. Further reduction of ΔZ might be feasible to reduce discontinuities, but non-contact polishing techniques, such as IBE polishing could possibly improve the final roughness [46].

3.5 Implantation

In this section, the implantation part of the process flow for the DOI platform is examined. For a reliable fabrication, the implantation effects should be predictable via modelling and the results quantifiable by measurement.

The simulation of the effect of implantation concerns primarily the distribution of vacancies created by the implanted ions and their relation to graphitised matter. For the calculation of the effective vacancy distribution, the linear distribution is first numerically simulated

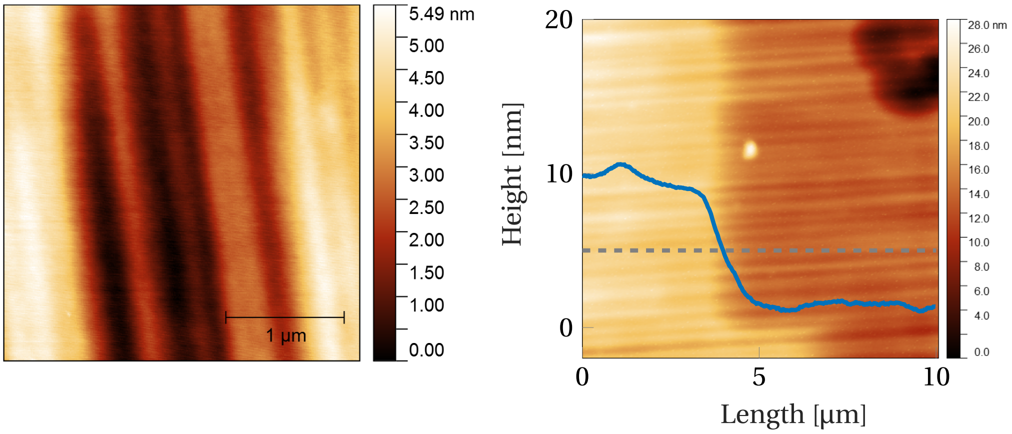

(a) (b)

Figure 3.11 – **a)** AFM measurement of the surface of the flattened area after etching shows that the roughness is unchanged with respect to the original polishing. The vertical grooves are a byproduct of the scaife polishing process and are not produced by this technique. **b)** AFM measurement of a resist step transferred into diamond. The gray dashed line shows where the blue profile was extracted. As expected, a ~10 nm step is observed, which equals the ΔZ multiplied with the selectivity $(1:15)$. Due to the low selectivity, the step is also smoothed laterally, with the slope angle below 0.5°.

via TRIM [252], denoted with $\lambda(z)$. During this simulation, it is assumed that each new implanted ion arrives in a pristine material. However in the real material, there are additional phenomena to account for to accurately model the implantation effects [119]. The first effect is that vacancies can recombine with self-interstitials:

$$P_{rec}(F,z) = \frac{\rho_V(F,z)}{\alpha} \tag{3.6}$$

where P_{rec} is the recombination probability based on the fluence F and depth z, $\rho_V(F,z)$ is the vacancy density, α is the empirically derived parameter for saturation vacancy density, or in other terms, when the density of vacancies reach α, any further implantation will only move atoms, but not create new vacancies. Using this formula, the effective distribution can be calculated, accounting for saturation:

$$\rho_V(F,z) = \alpha \left[1 - \exp\left(-\frac{\lambda(z)F}{\alpha}\right)\right] \tag{3.7}$$

The mass density can be calculated by assuming there is a linear relationship to vacancy density (no vacancies($\rho_{Diamond}$) → α vacancies(ρ_{aC})):

$$\rho(F,z) = \rho_d - (\rho_d - \rho_{aC})\left[1 - \exp\left(-\frac{\lambda(z)F}{\alpha}\right)\right] \tag{3.8}$$

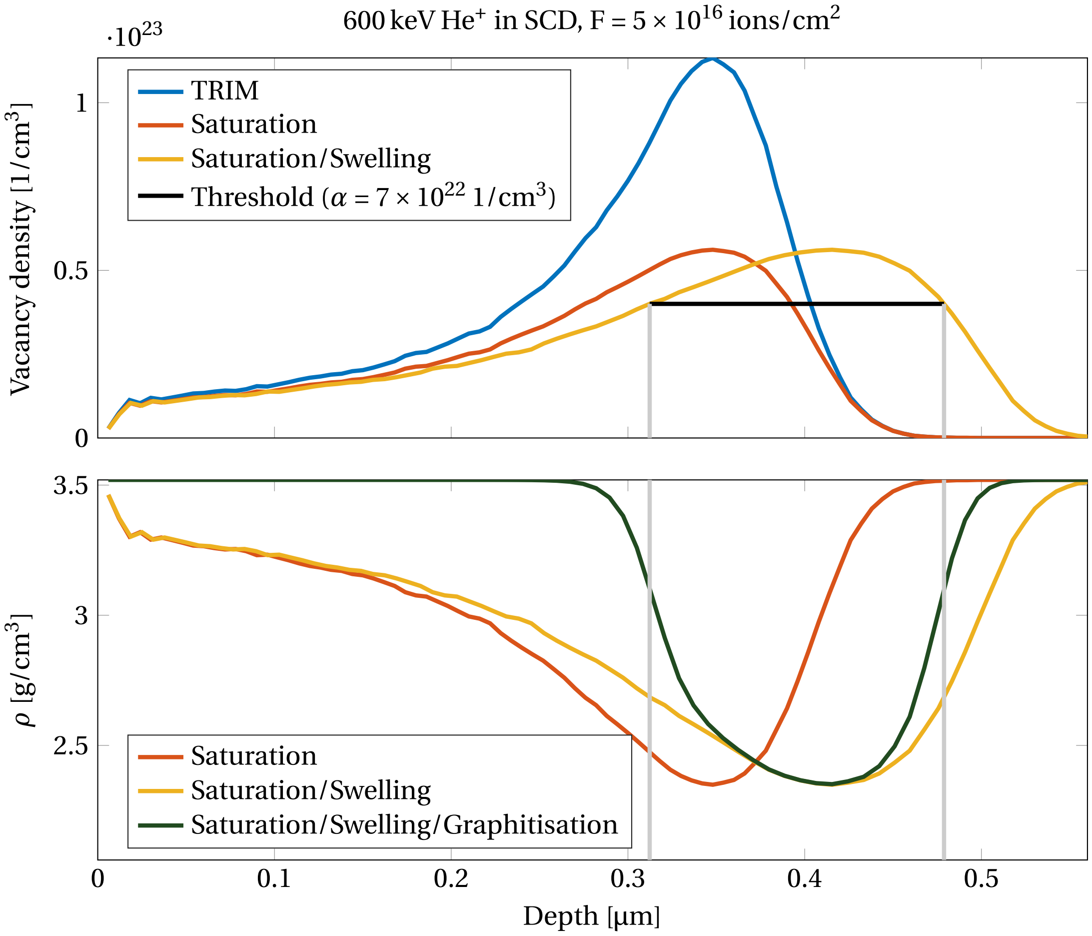

Figure 3.12 – Simulation of vacancy density and mass density distribution, based on Monte-Carlo ion collision cascade simulation [252], taking into account the saturation of vacancies, swelling of the implanted region and eventual graphitisation at room temperature [119] ($\beta = 1 \times 10^{-8}$). The diamond is capped with 1.4 µm-thick Al layer to reduce implantation depth. The grey lines indicate the region that undergoes irreversible graphitisation due to the implantation (the vacancy density is above the threshold α), with a thickness of 166 nm at a depth of 313 nm.

The diamond material also undergoes swelling during implantation, which will distort this distribution. To account for this effect, the depth coordinate is rescaled, based on the change in density:

$$z_i \rightarrow z'_i = z'_{i-1} + \frac{\rho_d}{\rho(z_i)} \Delta z \tag{3.9}$$

This modified z'_i is then used to evaluated $\rho(z')$ and $\rho_V(z')$ to get the distributions accounted for swelling. ρ_{th} is introduced, which is the threshold vacancy density, above which the layer transforms to amorphous carbon. This threshold value is then used to identify the region of graphitised diamond. The empirical parameter β (typical value 1×10^{-8} for room temperature implanting) controls the transition between diamond and amorphous carbon, which depends on the implantation temperature and post-implantation annealing. Using this, the density can be calculated, accounting for graphitisation:

$$\rho(F,z) = \rho_d - (\rho_d - \rho_{aC})\left[1 - \exp\left(-\frac{\lambda(z)F}{\alpha}\right)\right] \times \frac{\exp\left(-\frac{z - z_{th2}}{\beta}\right)}{\left[1+\exp\left(-\frac{z-z_{th1}}{\beta}\right)\right]\left[1+\exp\left(-\frac{z-z_{th2}}{\beta}\right)\right]} \tag{3.10}$$

Where z_{th1} and z_{th2} denote the start and end coordinate of the region where ρ_{th} is reached (the graphitised region).

Using these equations, the implantation of 600 keV He$^+$ was simulated. The ion energy was constrained by the accelerator, so to achieve a thinner membrane, a stopping layer of Al was used **Figure 3.12**, deposited via evaporation. The diamond sample was irradiated at the HES-SO Ionlab-ARC facility, using a tandem linear accelerator (Dynamitron) with a fluence of 5×10^{16} ions/cm^2. The system uses raster scanning of a small Gaussian ion beam spot over the surface of the sample, performing scans until the desired fluence is reached. The average implantation current was 6.37 nA.

Post implantation, the Al layer was stripped. To quantify the implantation depth, ellipsometry was attempted, along with spectral reflectometry. These techniques confirmed that there was a change in the optical properties of the diamond, but the fitting of the data was unsuccessful due to the difficulty of fitting a gradual change in refractive index and absorption.

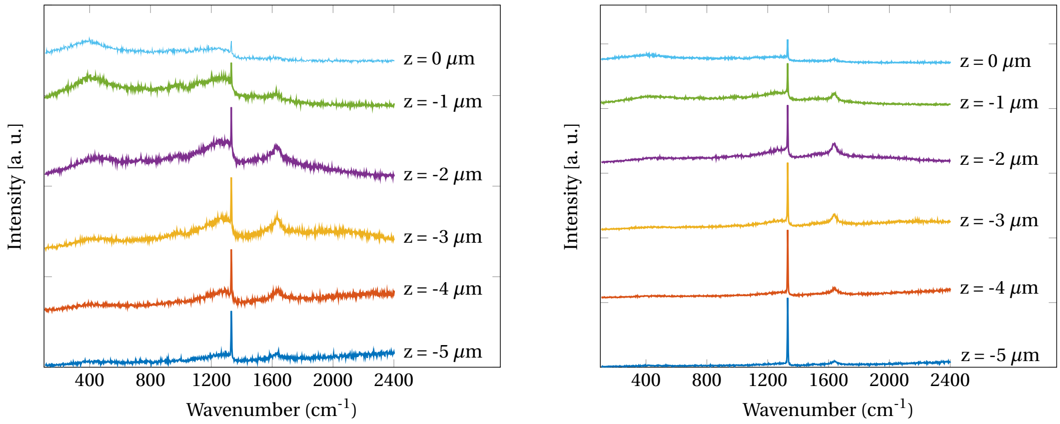

(a) As-implanted

(b) Implanted and annealed

Figure 3.13 – Depth-resolved Raman spectroscopy of the **(a)** implanted diamond and the **(b)** implanted+annealed diamond sample. The implanted sample shows additional peaks attributed to amorphous carbon, which are significantly reduced by high temperature annealing, indicating a regeneration of the ion damage.

Raman spectra were recorded for both an implanted and an implanted and annealed sample (Renishaw InVia, **Figure 3.13**). A silicon sample was used to estimate sampling volume of the microscope, which yielded a thickness of ≈ 2 μm. This means that quantitative analysis would be difficult with the technique, especially since the depth scale is not calibrated ($z = 0$ μm corresponds approximately to a focused spot on the surface). However, the recorded spectra clearly show the additional peaks corresponding to amorphous carbon (most prominently at 1630 cm^{-1}). The annealed sample also shows much higher intensity of the "diamond" peak, attributable to regeneration of the layer.

For more accurate measurement, transmission electron microscopy (TEM) lamellas were prepared using the FEI Nanolab FIB/SEM system[1]. The diamond chips were found to charge during FIB processing because of the Ga^+ implantation, so aluminium is sputtered before machining to ground the sample during processing.

Measurement of a prepared lamella was carried out on a FEI Talos TEM at the Interdisciplinary Centre for Electron Microscopy (CIME) EPFL [262]. Selected area diffraction and dark field imaging confirms the existence of an amorphous layer of carbon buried in the diamond. Bright field imaging shows the damage layer extending slightly from the amorphous area, with nanocrystalline carbon dotting the transition region in black (**Figure 3.14b**). In good agreement with simulation results (**Figure 3.12**), the layer appears approximately at 413 nm, with 53 nm thickness. The difference in amorphised layer thickness (and therefore depth) can be caused by lower than design fluence, due to error in the scanning of the beam.

Post-implantation, annealing is carried out to finish conversion of the damaged layer to amorphous carbon, sharpen the transition between the cap crystalline layer and the a–C layer and to remove damage from the cap layer. Since diamond readily oxidises (burns) at temperatures > 600 °C in ambient, the annealing is carried out in under high vacuum, since high temperatures (>1000 °C) increases regeneration of the lattice. Annealing of the sample was carried out at 1250 °C, 1×10^{-5} mbar for 1 hour. Transmission electron microscope imaging of the annealed sample shows a regeneration of the damage in the capping layer, along with a sharpening of the interface (**Figure 3.14c**).

3.6 Bonding

Following the implantation and annealing, the diamond substrate is bonded to the oxidised Si chip. The ideal bonding solution for joining the diamond substrate is direct bonding due to the high thermal budget and the lack of other materials that can be located near optical fields (causing absorption).

In general, direct bonding requires three properties of the surfaces to be joined: flatness, smoothness and cleanliness.

Contamination of the surfaces can manifest in adsorbed layers and particles. Particles cause unbonded regions (voids), acting like spacers between the two surfaces. Particles can cause voids many times larger than the particle diameter due to this effect. Adsorbed contaminants can inhibit the adhesion and can outgas during annealing steps.

---

[1] FIB lamella preparation by Teodoro Graziosi

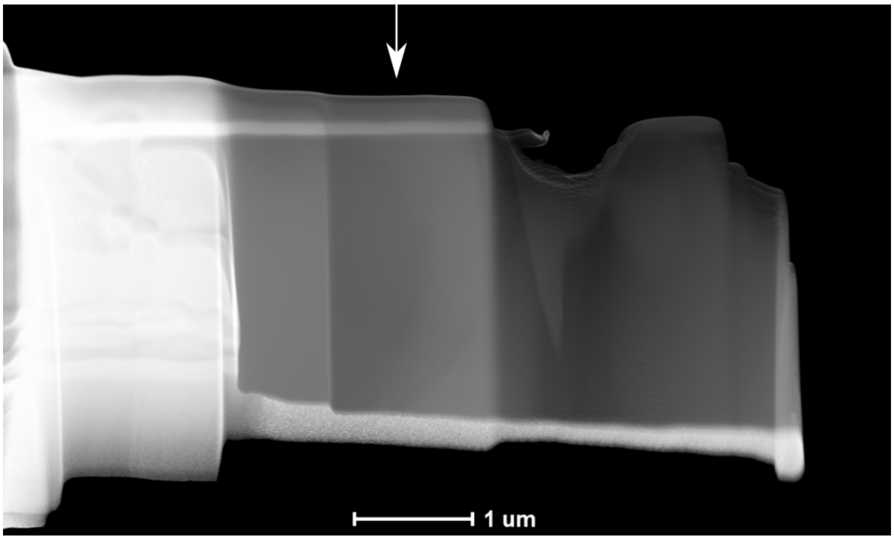

(a) STEM image of the lamella, showing density contrast. Lighter gray band is the graphitised layer.

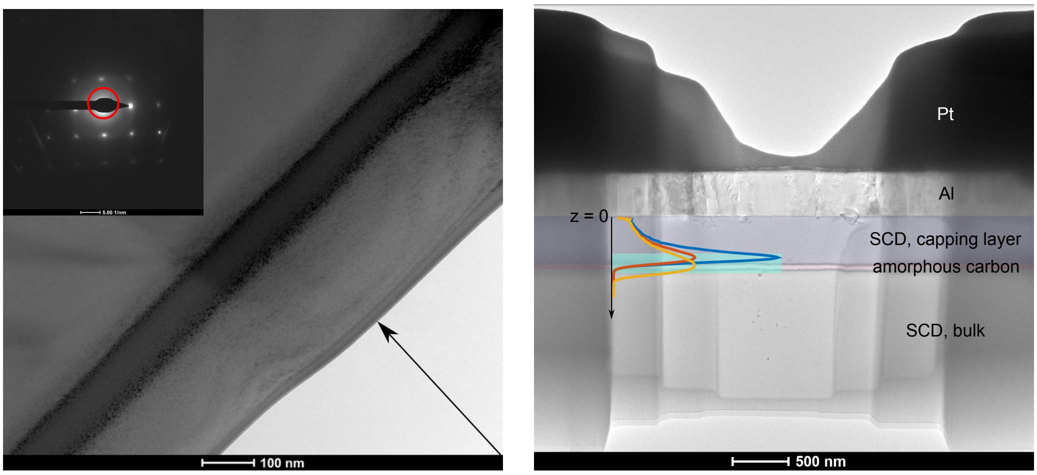

(b) TEM Bright Field image of the implanted region, ⟨1 0 0⟩ zone axis. Inset shows diffraction and the position of the objective aperture.

(c) TEM image of the implanted region after annealing at 1250 °C, ⟨1 0 0⟩ zone axis. Overlaid are the numerical simulation of the graphitisation (**Figure 3.12**), with the predicted amorphous carbon region highlighted in blue.

Figure 3.14 – S/TEM images of an implanted diamond lamella, arrows show the direction of implantation. The graphitised region is appears 413 nm, with 53 nm thickness, surrounded by an inhomogeneous nanocrystalline carbon phase. Upon annealing the nanocrystalline carbon signal is reduced, showing the recovery of the diamond layer and a sharpening of the transition.

The bonding surfaces need to be smooth to achieve bonding. If the surfaces are rough, only a small area can come close enough to form the bonds required, however the surface asperities can deform to get closer contact. The model for the description of the role of roughness in bonding was proposed by Gui et al. [263]. A dimensionless adhesion parameter (θ) is calculated based on a rough surface with a Gaussian height distribution of asperities with spherical caps contacting a flat rigid plane (**Figure 3.15b**):

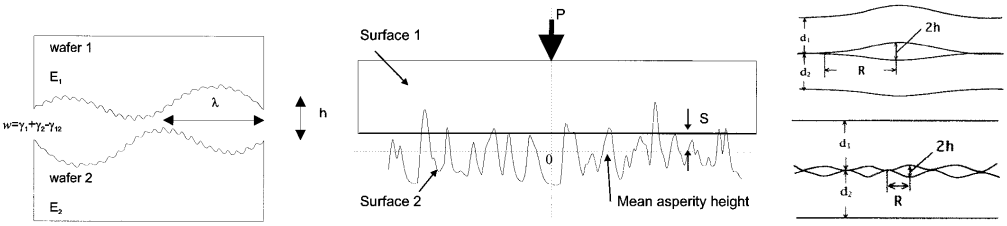

(a) (b) (c)

Figure 3.15 – **(a)** Schematic of two surfaces coming into contact for direct bonding. The surfaces exhibit both high frequency (roughness) and low frequency (flatness) non-uniformity. **(b)** Schematic for modeling adhesion in the presence of roughness: a rough surface with asperity heights obeying a Gaussian distribution contacting a flat rigid surface. **(c)** Schematic for modeling gap closing for non-flat substrates: a gap of lateral extension R and height of $2h$ between wafers of thickness d. **(a,b)** reproduced from [263], **(c)** reproduced from [150].

$$\theta = \frac{E^*}{w}\sqrt{\frac{\sigma^3}{R}} \tag{3.11}$$

$$w = \gamma_1 + \gamma_2 - \gamma_{12}; \qquad E^* = \frac{4}{3}\left[\frac{E}{1-\nu^2}\right] \tag{3.12}$$

where ν is Poisson's ratio, E is the Young modulus, w is the specific surface energy of adhesion (related to γ_x, the surface energy and γ_{xy}, the interface energy) and σ and R describe the rough surface statistically — σ is the standard deviation of the Gaussian distribution and R is the radius of the caps.

The adhesion parameter θ is used to define three regions of bonding regimes:

nonbonding regime, $\theta > 12$
In this regime the effective bonding energy and real contact area is effectively zero, no bonding is possible between the two surfaces.

adherence regime, $1 < \theta < 12$
The real area of contact and effective bonding energy increases with decreasing θ. Bonded area is typically less than 100 %.

bonding regime, $\theta < 1$
Maximum effective bonding surface and bonding energy. Bonded area is ~ 100 %, if the other direct bonding criteria (cleanliness, flatness) are fulfilled.

As roughness determines the microscopic contact possible during bonding, flatness determines the macroscopic contact. Atomically flat surfaces are difficult to produce, but the two surfaces can elastically deform (bend) to have larger area in contact. Tong et al. derived an elastomechanical approximation for predicting how large of a surface flatness non-uniformity will still result in the deformation of the surface and bonding, instead of forming voids [150].

	R_q[nm]	σ[nm]	R[µm]	η	$\sigma \cdot R \cdot \eta$
diamond	0.522	0.34	2.45	87	0.073
SiO_2 [268]	0.242	0.143	312.18	4.36	0.1947
combined	-	0.36	17.17	-	-

Table 3.2 – Roughness parameters of diamond, wet grown silicon dioxide and the combined representative roughness of the two surfaces being mated.

The approximation considers two wafers of the same material and thickness (**Figure 3.15c**). The first case considers a gap with a lateral extension (L) much larger than the gap height ($L > 2 \cdot h$):

$$h \leq L^2 \left[\frac{w}{1.2 \cdot E \cdot d^3}\right]^{1/2} \tag{3.13}$$

with E being Young's modulus, w the specific surface energy of adhesion and d is the wafer thickness. The equation shows that thinner and more compliant wafers will make gap closing easier. Similarly, if the lateral extension is below the gap height ($2 \cdot h$):

$$h \leq 2.6 \left[\frac{L \cdot w}{E}\right]^{1/2} \tag{3.14}$$

Applying these calculations to diamond-silicon dioxide bonding, it can be seen that for the mating of two surfaces, both surfaces will have some degree of roughness. However, the Young's modulus of diamond ($E = 1080$ GPa [264]) is much larger than the one of oxide (wet grown, $E = 57$ GPa [265], $\nu = 0.17$ [266]), so the deformation of diamond during the bonding process is neglected. The roughness parameters of the diamond surface is calculated from profiles of AFM scan of a fine polished diamond (ALMAX Easylab) using a MATLAB script ([267]), while the roughness parameters for wet thermal oxide were used from [268]. The extraction of the surface parameters was performed so that the resulting values obey $\sigma \cdot R \cdot \eta \in [0.05, 0.1]$ [263].

The roughness values for the two surfaces are combined together: the R mean asperity cap radius is calculated as the density-weighted mean of the two radii ($\left(R_1 \cdot \eta_1 + R_2 \cdot \eta_2\right) \cdot {}^1/_{\eta_1+\eta_2}$), while the standard deviation of the asperity height σ is calculated from the standard deviation of the sum of two independent Gaussian distributions ($\sqrt{\sigma_1^2 + \sigma_2^2}$). The values for the individual and combined surfaces are shown in **Table 3.2**.

While the specific surface energy of adhesion (w) is not known for diamond and oxide, the value is expected to be in the range of adhesion energies found for silicon – oxide/silicon – silicon bonding. The reported values for w are $0.7\,\mathrm{J\,m^{-2}}$ to $0.8\,\mathrm{J\,m^{-2}}$ for Si-oxide [145], $0.1\,\mathrm{J\,m^{-2}}$ to $0.15\,\mathrm{J\,m^{-2}}$ for hydrophilic Si-Si [145, 263] and $0.03\,\mathrm{J\,m^{-2}}$ for hydrophobic Si-Si bonding [145]. This yields a θ value between 2.6 for weak bonding and 0.9 or smaller for strong bonding. This shows that at least partial bonding of diamond and SiO_2 surfaces can be attained using direct bonding methods, if the surfaces are suitably smooth and flat.

For determining the maximum peak-to-valley flatness, a surface energy of $9.57\,\mathrm{J\,m^{-2}}$ [264] is used. For this case, the mechanical contribution of the thin oxide is neglected, and only a slab of diamond and silicon is investigated. The Young's modulus of silicon is 165 GPa [6], so as a simplified model, only the deformation of silicon is taken into account (the bow of the Si wafer is neglected over the small area of the diamond chip as well). Considering a "dome" or a "saddle"-type topography (typical for the samples used in this thesis), the largest separation between the peak and the valley (lateral extension of the non-uniformity) is half of the diagonal of the chip (~1.83 mm), which results in a maximal bondable peak-to-valley topography of 197 nm, if the adhesion energy is considered as $0.1\,\mathrm{J\,m^{-2}}$ (standard 525 µm-thick Si wafer).

Experimental plasma-enhanced direct bonding of diamond to oxidised silicon wafers and chips were carried out. Both bonding surfaces are exposed to oxygen plasma in barrel etcher (500 W, 5 min, Tepla Gigabatch). Immediately afterwards the diamond chip is dipped into DI water and placed on the SiO_2 surface with activated surfaces touching, and the water is evaporated by gently blowing N_2. At this stage, a thin layer of water can provide adhesion even in cases where the mated surfaces will not support bonding, so the assembly must be tested by heat treatment or applying water to the bond, both of which immediately debond the surface if the direct bonding was unsuccessful. Diamond chips with surface flatness below 100 nm were successfully bonded in this fashion, as well as partial bonds achieved where the topography of the chip permitted this. The bonds were stable in water, vacuum and during annealing up to 600 °C, indicating successful adhesion of the surfaces. However, since flattened substrates were not available at the time, an alternative, HSQ interlayer process was investigated.

HSQ interlayer bonding was carried out to perform bonding of the substrates with topography unsuitable for direct bonding. HSQ (FOX-16, Dow) was spin coated onto a silicon chip at 2000 RPM, resulting in HSQ layers of ~0.95 µm thickness. Immediately after coating, the diamond chip was placed into contact and the assembly was transferred to a heated press, where 0.15 MPa pressure was applied, before heating to 250 °C ($10\,^{\circ}\mathrm{C\,min^{-1}}$) for 1 h. Afterwards, the sample was let to cool down to room temperature, before removing the pressure. The samples very reliably bonded in this fashion, and optical inspection reveals no colour on the bonded area, suggesting close to 100 % bonding. Unfortunately, debonding occurs on annealing in an oven (300 °C+), possibly due to the release of the elastic energy of the diamond plate or outgassing/volume change of the HSQ layer.

3.7 Membrane preparation and patterning

For etching the amorphous carbon layer, the electrochemical etch method was used [131], since it offers superior etching times to the chemical etch method, the latter being diffusion-driven. Furthermore, the chemical etch method utilises hazardous acids ($HClO_4$), to which the electrochemical etching is preferable.

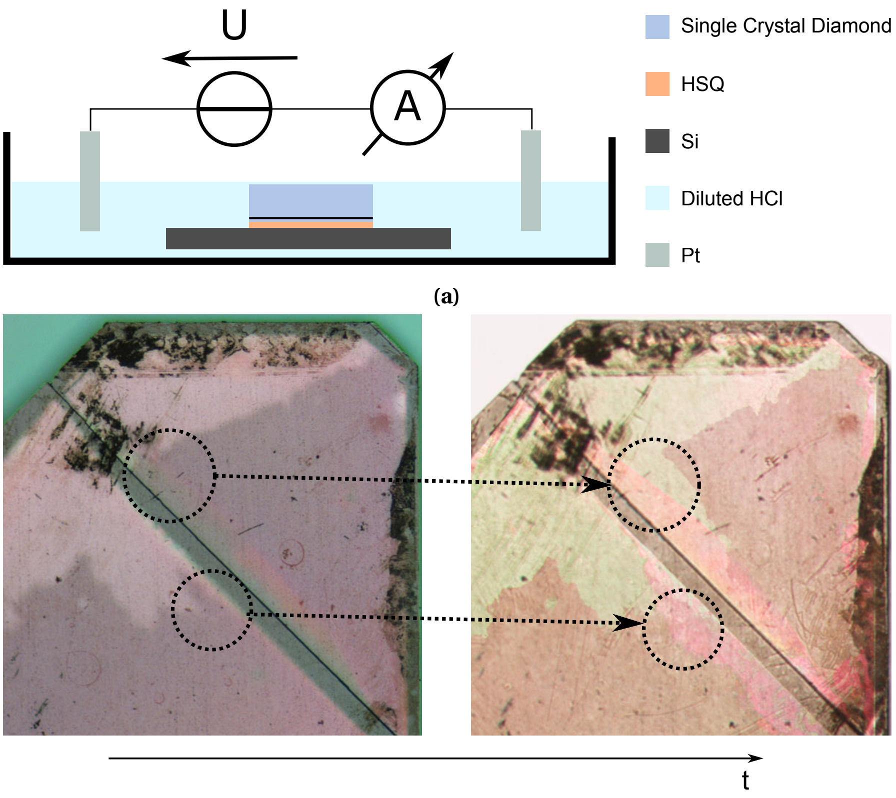

(a)

(b)

Figure 3.16 – **(a)** Electrochemical etch setup. DC voltage (70 V) is applied to two platinum electrodes. The electrodes are immersed into a diluted HCl electrolyte, and placed on the sides of the diamond die. **(b)** Optical microscope images showing the progression of the carbon etching, with highlighted areas that show the portion of layer etched during the time interval between the two images. The areas where the amorphous carbon is removed appear lighter due to the reduction in absorption.

The sample is immersed in a diluted 0.015 %, 0.00487 mol L^{-1}) HCl that serves as the electrolyte. Platinum wires are placed in the vicinity of the chip from two sides, at approximately 3 mm from each other (**Figure 3.16a**). 70 VDC is applied, which results in current in the range of 10 mA to 20 mA, depending on the level of the electrolyte. During the etching the electrolyte needs to be regularly replenished, since it is continuously electrolysed into H_2 and O_2. Etching time is estimated at 16 hours, after which partial debonding occurred (etch time estimation is difficult due to the non-constant electrolyte level and current), possibly due to the fragility of the thin diamond cap layer and stress from the HSQ bonding method. However, membrane fragments remain bonded, with typical sizes on the order of 0.05 mm. The shape of the membrane pieces have sharp angles, which are another indication of the preservation of the crystalline nature of the capping layer (**Figure 3.17a**). The remaining amorphous carbon is removed via IBE (−5° angle, 300 V, 15 min), a process that has high selectivity against non-diamond material. This process also etches the exposed HSQ (**Figure 3.18a**). Atomic force microscopy measurements reveal defects mimicking original surface defects in the diamond, along with added roughness of the membrane that is attributed to the roughness in the metallic stopping layer, transferred via ion implantation. The rms roughness of the layer was measured to be between 6 nm to 16 nm (**Figure 3.17b**).

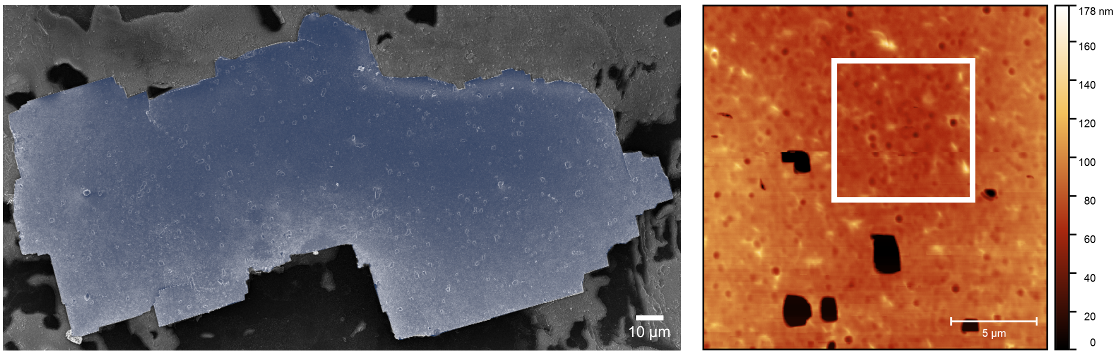

(a)

(b)

Figure 3.17 – **(a)** SEM image of a single crystal diamond membrane piece after the electrochemical etching (blue). The surface mimics surface defects from the original plate. Inset shows HSQ disks patterned on such a membrane. **(b)** AFM measurement of the surface of diamond flake after cleaning. The surface displays defects from the original surface and added roughness from the metallic stopping layer, yielding an rms roughness of 15.8 nm. With the deep pits excluded (white region), the rms roughness is 6.1 nm.

Following the preparation of the membrane, electron beam lithography is used to define the structures. In this case, disks were exposed in HSQ (FOX-16, ~500 nm thickness), with diameters of 5 µm. After development (1 min, 25 % TMAH, 25 %), the HSQ patterns were transferred into the diamond using vertical etching (**§ 4.3**, 4 min). The underlying HSQ was etched using IBE (−5° angle, 300 V, 30 min), and then the silicon was etched to form free-standing pillars (SF_6/C_4F_8 chemistry Bosch process, 3 min), to enable tapered fiber probing of the structures. To enable release, HSQ was cured at 420 °C for 1 hour, which removes the remaining organic component in the resist, leaving only SiOx. After the curing, HF vapour release of the structures was performed (1 cycle, 300 s, 75 Torr). The etch rate of the vapour HF system has to be greatly reduced, as cured HSQ is much less dense than the typical SiO_2 layers and therefore etches much faster. A released disk fabricated using this method is shown on **Figure 3.18b**. To prevent the fencing occurring during IBE etching, the patterning method was improved to use ICP RIE etching of the HSQ layer, resulting in fence-free disks (**Figure 3.18c**).

3.8 Discussion and conclusion

Diamond-based optical devices require sophisticated microfabrication techniques, especially if commercial exploitation is the goal. While the material properties are excellent, the processes for manufacturing high quality substrates and their patterning is much less advanced than silicon and other semiconductor material systems. The techniques outlined in this chapter have various applications. Preparation of flat and smooth optical substrates from diamond are a prerequisite for many devices, although in this case this process was carried out to

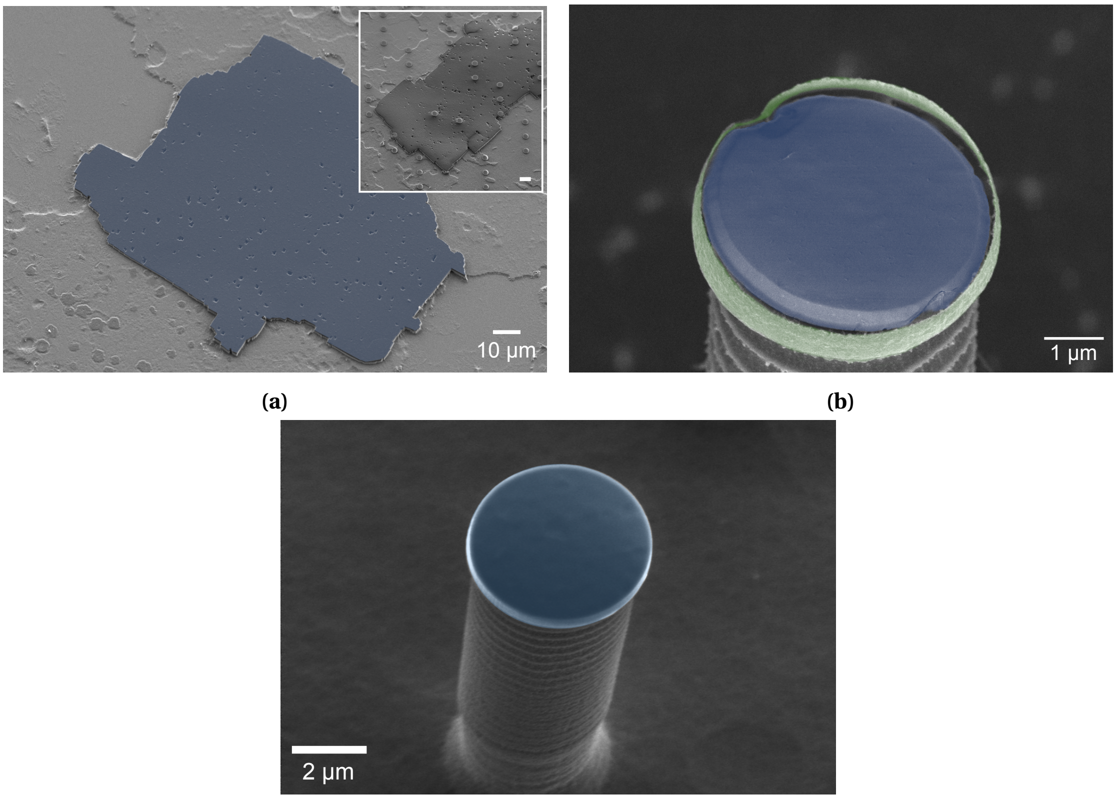

(a) (b)

(c)

Figure 3.18 – **(a)** SEM image of a single crystal diamond membrane piece (blue) after IBE cleaning. The surface mimics surface defects from the original plate. Inset shows HSQ disks patterned on such a membrane. **(b)** Colourised SEM image of a released microdisk, single crystal diamond highlighted in blue. The green fence is a byproduct of the ion beam etching process.**(c)** Colourised SEM image of microdisk fabricated with a modified process showing defect free disk geometry and smooth surface.

promote flatness for bonding applications. It is expected that this process can yield extremely flat substrates that preserve the smoothness imparted on them by scaife polishing, thereby allowing the combination of low roughness and high flatness in a process.

Diamond-on-insulator type substrates are an extremely attractive proposition, for creating a scalable platform for guided-wave optics in diamond. In this chapter, the transfer of single crystal diamond membranes was demonstrated using an HSQ bonding process. The membranes were created using He^+ implantation. Cap layer thickness was measured via TEM and found to have good agreement with modelling results. The bonding of membrane pieces was achieved using an adhesive – HSQ based bonding process. The transferred membranes have been characterised by SEM and AFM, revealing high quality, with uniform thickness and smooth surface. Furthermore, free-standing disks have been demonstrated via a release of the HSQ layer.

While the lift-off method has been known for a long time, the development of the process to bond thick diamond plates is the crucial step for commercialization, as membrane transfer processes are difficult to scale. This demonstration of the feasibility of this process opens up the way to such industrial efforts. Furthermore, the development of the substrate smoothing and flattening processes promises the additional improvement of performing direct bonding of the diamond substrates, which allows the integration of diamond membranes without the HSQ interlayer, improving the optical, mechanical and release process properties.

4 Development of etching and microfabrication for SCD microoptics

This chapter describes the development and application of diamond plasma etch processes and microoptical devices that have been fabricated via these techniques. Three different diamond dry etch procedures are described and characterised, named crystallographic, deep and vertical. These etching methods shape the diamond substrate optimised for a distinct goal, that enables the fabrication of devices with novel geometries. Along with the introduction of each etch, a microoptical device fabrication flow is shown, that makes use of the properties the etch imparts on them. For each process, the steps are shown in detail to facilitate reproduction of these methods, and the devices are characterised to qualify the process.

4.1 Crystallographic etching

Crystallographic etching is a novel technique for diamond microfabrication that allows defining quasi-3D structures that can lead to exciting applications for MEMS and microoptics. In this section, a process is shown using crystallographic etching for the fabrication of diffraction gratings, along with investigation into the geometry produced by this dry etching method.

The microfabrication process is carried out on commercially available general grade single crystal diamond plates (**Table 3.1**, Element Six, Lake Diamond) with typical dimensions of 2.6 mm x 2.6 mm x 0.3 mm and $\langle 100 \rangle$ crystal orientation (**Figure 4.1**). The plates are first cleaned in acetone and IPA, then 60 nm of Al_2O_3 is deposited using atomic layer deposition (ALD). Alumina represents an excellent hardmask for this etch process, with selectivity better than 400:1. The other tested hardmask material etch rates and approximate selectivities are shown in **Table 4.1** The diamond plate is fixed to a wafer using mounting wax (QuickStick 135) to ensure thermal contact during diamond etching and facilitate handling. Subsequently

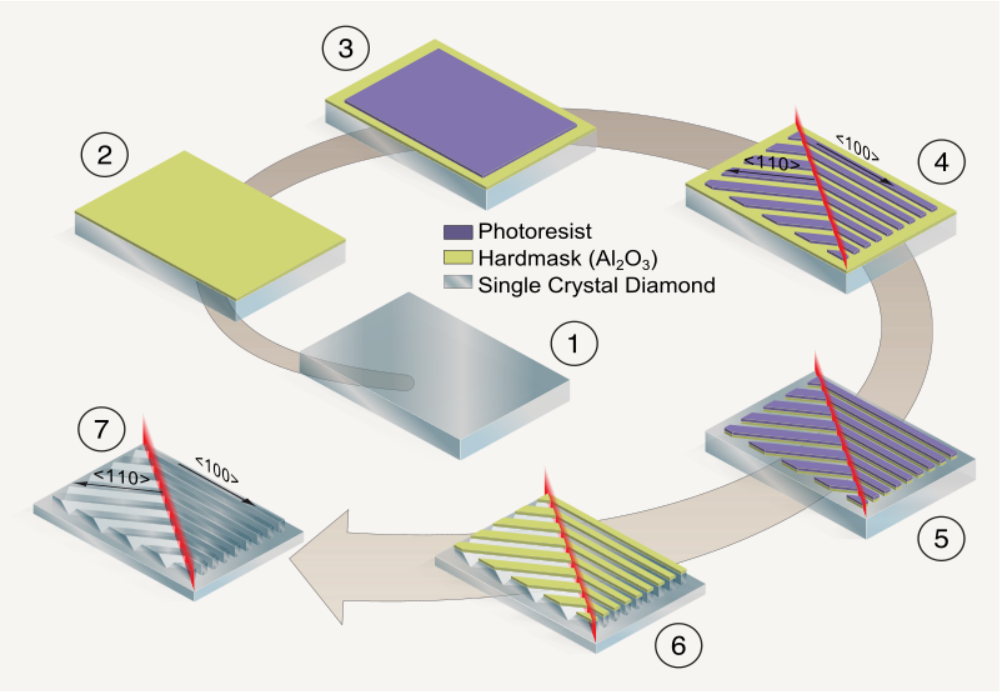

Figure 4.1 – Schematic representation of the microfabrication process for diffraction gratings in single crystal diamond: **1)** substrate cleaning **2)** Al_2O_3 deposition **3)** photoresist spincoating **4)** photoresist patterned with lines along either $\langle 1\,1\,0\rangle$ or $\langle 1\,0\,0\rangle$ direction **5)** alumina hardmask dry etch **6)** diamond dry etch resulting in grooves with profile dependent on direction.

photoresist (AZ ECI 3007) is spincoated onto the chip (400 nm thick).

Spincoating on small substrates is more difficult than on wafer-scale, since for uniform coating the centripetal force needs to overcome the adhesive force trapping the photoresist at the edge of the chip, which leads to a significant edge bead. This edge bead needs to be removed in order to have a close contact between the photomask and the photoresist during exposure for high-resolution pattern transfer. A two-cycle photolithography exposure approach was developed to completely remove the edge-bead region on the small substrate. After the photoresist spin coating, a first exposure is performed on a 0.5 mm-wide frame covering the inside of the four edges of the diamond plate, with a high dose adapted to the important thickness of the edge bead. In a subsequent first development, the edge bead is removed allowing to perform a closely contacted exposure of the central region using a photomask with the dense groove pattern (**Figure 4.2**).

The grating lines are exposed using contact lithography, aligned to the chip edges. Two samples were fabricated one with grating lines in the $\langle 1\,1\,0\rangle$, the other with grating lines in the $\langle 1\,0\,0\rangle$ direction. The alumina hardmask is etched in a deep reactive ion etcher using chlorine chemistry (STS Multiplex). Afterwards, diamond etching is carried out using reactive ion etching (SPTS APS) with oxygen plasma, utilizing high ICP power (2000 W) and zero platen bias power (15 mTorr process pressure, 30 sccm O_2 gas flow, 25 °C). Etching time was 70

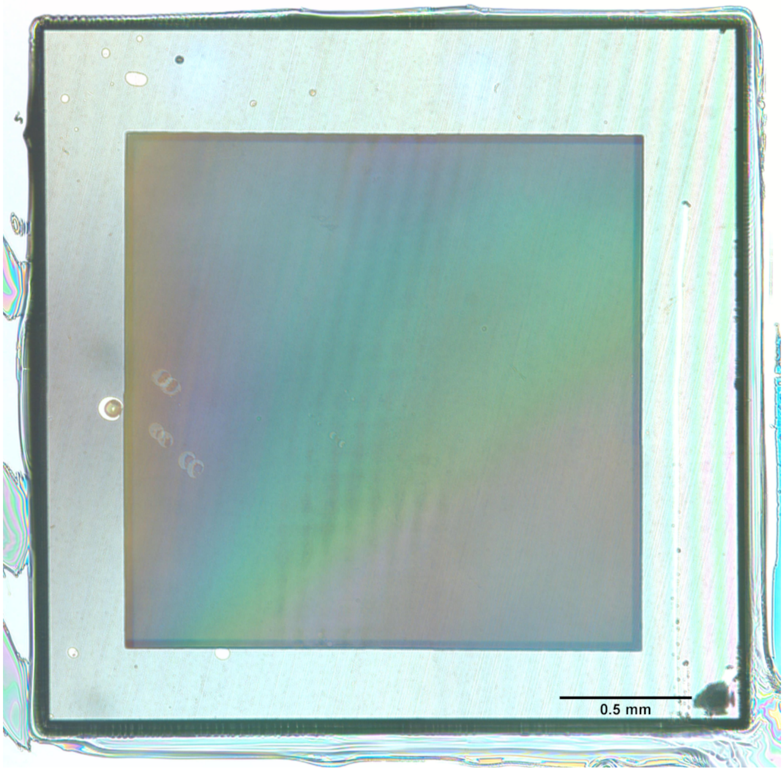

Figure 4.2 – Optical micrograph of a diamond chip (2.6 mm x 2.6 mm), after two-cycle lithography. Uniform exposure of the grating lines is possible over a large area (~4 mm) due to the removal of the edge-bead, which results in flat contact of the photomask with the resist. Flat contact reduces linewidth variation of the exposed pattern, improving the quality of the resulting grating.

minutes for the ⟨1 1 0⟩ gratings and 35 minutes for the ⟨1 0 0⟩ gratings, resulting in etch depths of 2.65 µm and 1.37 µm, respectively. After etching, the chip is released from the carrier wafer and the hardmask is stripped in concentrated hydrofluoric acid.

	SiO_2, sputtered	SiO_2, wet	Si_3N_4, LPCVD	Al_2O_3, sputtered
Etch rate [$\mathrm{nm\,min^{-1}}$]	10.23	3.25	3.14	0.08
Selectivity	3.4 : 1	10.76 : 1	11.14 : 1	437 : 1

Table 4.1 – Etch rate and selectivity of common hardmasks against the crystallographic plasma etch. Blank wafers with the indicated thin film were etched for 50 min with unbiased O_2 plasma (SPTS APS, 2000 W ICP power, 0 W platen bias power, 15 mTorr process pressure, 30 sccm gas flow, 25 °C). Spectral reflectometry (NanoSpec 6100) was used to measure the wafers on 25 points before and after the etch. The average of the measured values is reported.

Atomic force microscopy (AFM) was carried out on a Bruker FastScan using an EBD2-100A ultra-high aspect ratio probe (nanotools GmBH) (tip length: 2 µm). High aspect ratio tips are required for the measurements in order to accurately profile the roughness on the sidewalls and to measure the sidewall angle with respect to the surface, since using standard AFM tip geometries the sidewall surfaces cannot be reached. For the vertical sidewalls, the sample was tilted with respect to the probe cantilever (tilt angle 16°) to acquire accurate geometry and roughness. During post-processing the measured geometry was rotated by the tilt angle. In all cases, the scan direction was chosen to be perpendicular to the grooves and the probe symmetry axis to minimize the influence of the probe geometry. Reference angle measurements were taken on a KOH etched silicon sample to calibrate the measurements. Roughness values were taken from a groove sidewall with background removed to flatten the measured area. Angle measurements were also performed by SEM image analysis, and Focused Ion Beam (FIB) cross section, but were found to be limited in precision to 5°. **Table 4.2** summarizes the measurement results.

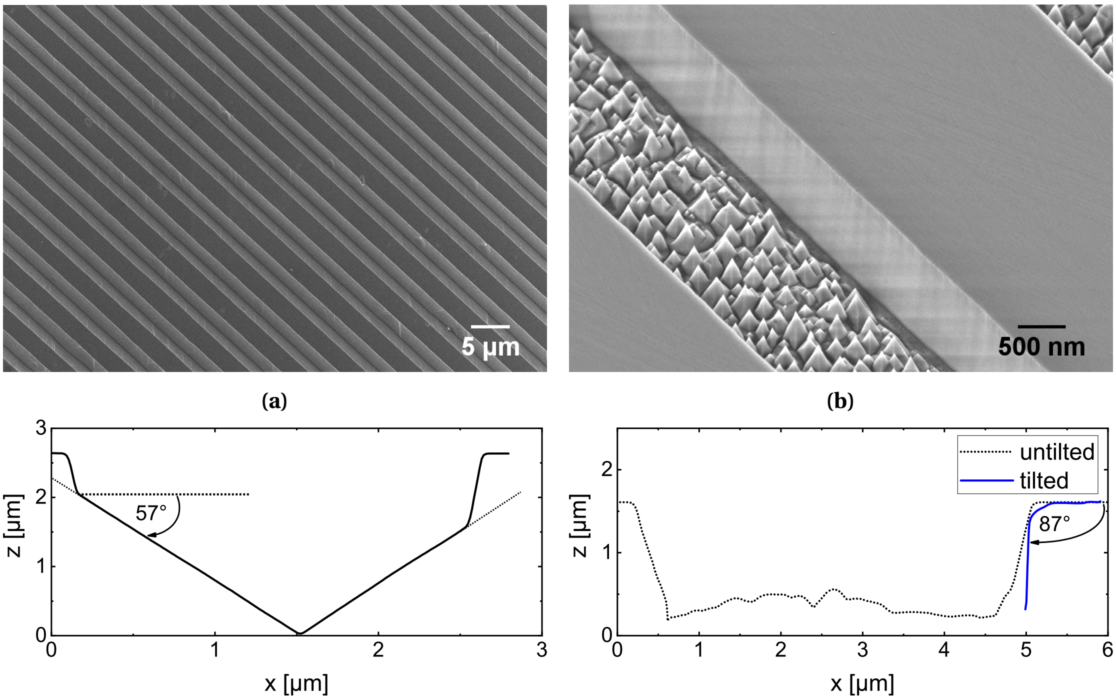

(a) **(b)**

(c) **(d)**

Figure 4.3 – **(a)** Scanning electron microscope (SEM) recording of $\langle 1\,1\,0\rangle$ gratings revealing V-shaped grooves **(b)** extracted profile across a single V-groove in the $\langle 1\,\bar{1}\,0\rangle$ direction, showing hardmask undercut (true groove shape indicated with dashed line) and a 57° sidewall angle **(c)** SEM recording of $\langle 1\,0\,0\rangle$ gratings showing a single grating groove with well-defined vertical sidewalls and **(d)** extracted profile across a single groove in $\langle 0\,1\,0\rangle$ direction. The blue line corresponds to an AFM profile measured with a tilted sample and correction applied.

The grooves fabricated in the $\langle 1\,1\,0\rangle$ direction have a pitch and depth of 5 µm and 2.65 µm, respectively, as seen in **Figure 4.3a**. We observed an asymmetry of the etched groove shape, which can be attributed to the misalignment of the gratings with respect to the $\langle 1\,1\,0\rangle$ direction, resulting in an undercut of the mask (**Figure 4.3b**, dashed line). This effect is commonly observed in silicon gratings fabricated by crystallographic wet etching [269].

The angle of the gratings with respect to the surface plane is 57°, measured via high-aspect ratio probe AFM (**Figure 4.3b**). The sidewalls of the $\langle 1\,1\,0\rangle$ groove are smooth with exception

V-Groove angle	(57.4 ± 3.3)°
V-Groove surface roughness (R_a)	22 nm
Rectangular groove angle	(87.47 ± 0.50)°
Rectangular groove surface roughness (R_a)	5 nm

Table 4.2 – Summary of measurements results using ultra-high aspect ratio tip atomic force microscopy.

of steps occurring due to groove misalignment, yielding a total R_a of 22 nm. Exclusion of the steps results in a mean roughness (R_a) better than 5 nm (**Figure 4.4b**).

The grooves realized in the ⟨1 0 0⟩ direction have a pitch and a depth of 4 µm and 1.37 µm, respectively (**Figure 4.3c**). The AFM measurements revealed an almost vertical sidewall with an angle of 87° (**Figure 4.3c**). We observed the sidewalls of the ⟨1 0 0⟩ grooves to be extremely smooth, with a measured R_a below 5 nm (**Figure 4.3b**). We also noted the roughening on the bottom of the trenches, which is attributed to masking by remaining hardmask material due to an insufficient overetch or initial roughness in the exposed area [52]. Subsequently fabricated structures employed ion beam polishing (based on [46] to improve surface roughness before the crystallographic etch process. For these structures, the etch floor roughness was greatly reduced, indicating that surface quality is determining factor for this feature.

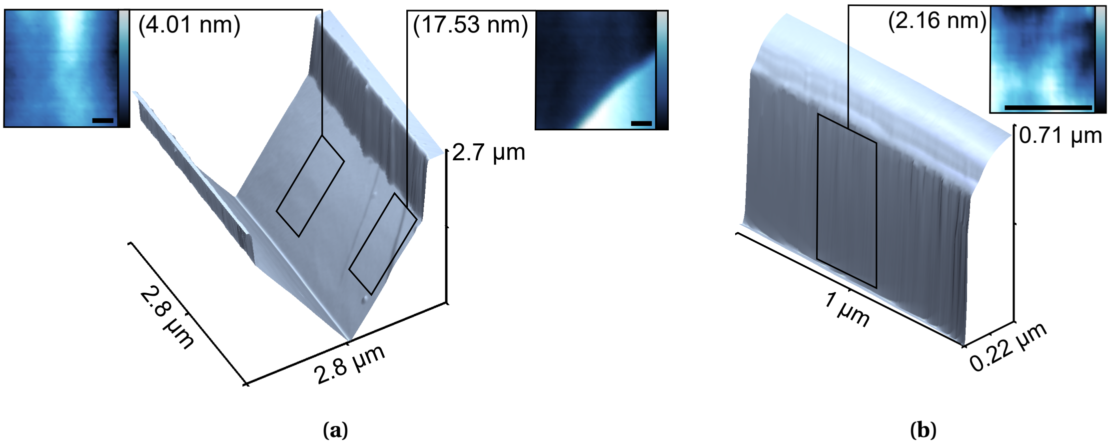

(a) **(b)**

Figure 4.4 – Atomic force microscope (AFM) surface profile of a **(a)** ⟨1 1 0⟩ grating V groove and a **(b)** ⟨1 0 0⟩ grating vertical groove. Insets on panel **(a)** show the otherwise smooth sidewall featuring steps due to misalignment of the patterns to the true ⟨1 1 0⟩ direction, raising the overall roughness of the profile. In contrast, the sidewall of the vertical grooves show no steps and are uniformly smooth. Scale bars in insets are all 100 nm, mean roughness (R_a) is indicated in parentheses.

4.1.1 Etch modelling

Modelling of the etch process for the grooves in the ⟨1 1 0⟩/⟨1 0 0⟩ direction was based on the continuous cellular automata method [270, 271]. The simulation starts by defining the simulation volume and an opening in the mask. Viewing a crystal with a (1 0 0) top surface, the lattice can be described as alternating layers of carbon atoms of location and bond configuration. The simulation is initialized by creating atoms for the layer in the non-masked area and assigning them to "etch front". Atoms represent a continuous state of etching: they start at 1 "integrity" and they are removed from the lattice at 0. During each etch cycle, the atoms belonging to the etch front are examined. For each atom, the number of neighbouring atoms are calculated, that indicates which crystalline plane the atom belongs to. Only the planes of the lowest order ((1 0 0), (1 1 0), (1 1 1)) were modelled, under the simplification that influence of higher order planes can be neglected [270]. Subsequently, the etch rate corresponding to the plane is used to decrease the integrity of the atoms. Whenever an atom is removed from the lattice, the neighbours revealed are added to the etch front. Newly revealed atoms always possess the opposite bond configuration. In addition, if the removed atom's integrity would've become negative, the new atoms will begin etching with a delay, preventing the clamping of the etch rate. After a set number of iterations (800), the remaining atom integrities are assembled into a surface (**Figure 4.5a**).

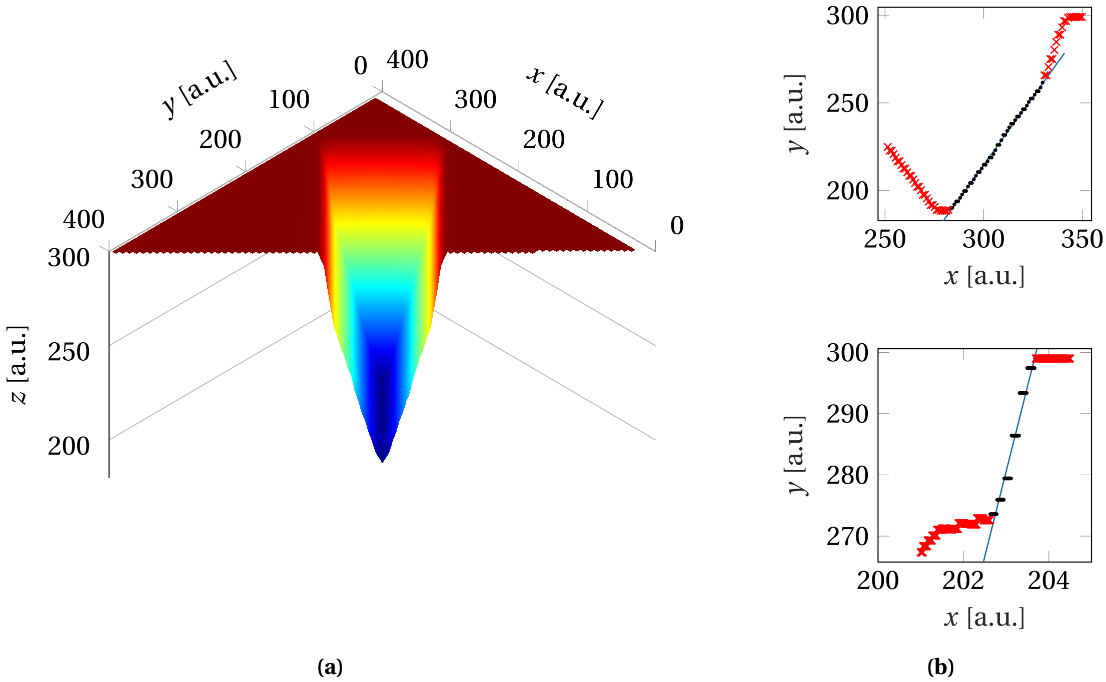

(a) (b)

Figure 4.5 – Crystallographic etch simulation via the continuous automata method. **a)** Cutaway of a simulated etch surface of a mask aperture along ⟨1 1 0⟩ direction. **b)** Extracted profiles of V-groove (top) and vertical groove (bottom) simulations. The blue lines show a linear fit to black points, which constitute the sidewall. The fitted lines subtend an angle of 57.3° and 87.9°, respectively, to the x axis.

To account for the directional etching characteristic of reactive ion etching, the model was extended by including an additional etching component, applied only on cells in line-of-sight of the mask opening (eg. directly exposed to the plasma). These etch rates are termed directional-($x\,y\,z$), depending on which crystalline plane etch rate they contribute to. Two dimensional profiles were extracted across trenches (in the ⟨1 1 0⟩ direction). Etch rates were fitted to the experimentally obtained profiles. Etch ratios of 0 : 1 : 20 : 10 : 10 : 25 ((1 0 0), (1 1 0), (1 1 1), directional-(1 0 0), directional-(1 1 0), directional-(1 1 1)) yield angles of 57.3° and 87.9°, respectively ([272]).

The etch rate of ((1 0 0)+direction(100)) was measured during etching by measuring the step height of the groove via AFM. The etch rate was initially 52 nm min^{-1} measured at 9 min, stabilizing at 34.6(26) nm min^{-1} (from 20 min). The crystal plane selectivity effectively show that the {1 0 0} planes are not attacked by this etch, and that the progression of the etch floor observed is only due to the residual ion bombardment. This observation is in good agreement with the fact that very tall vertical sidewalls were observed for extended etch times (**Figure 4.6**).

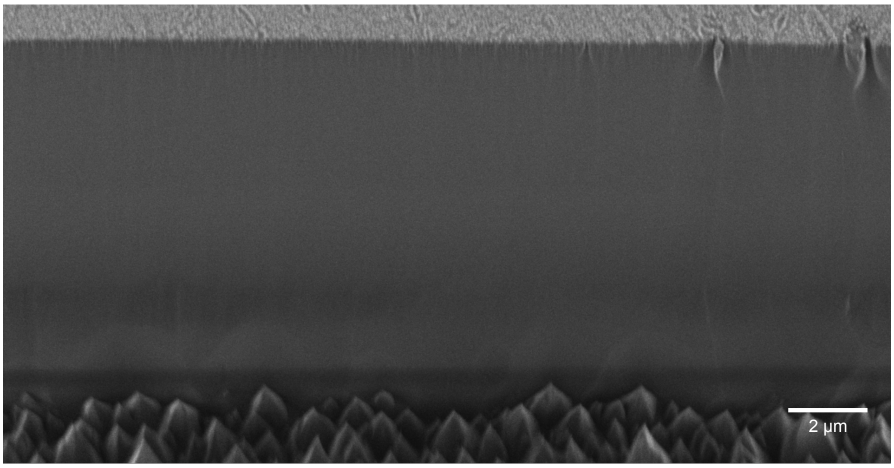

Figure 4.6 – Vertical sidewall after 8 hours 45 minutes of crystallographic etch. In accordance with the prediction of the etch modelling, the sidewall is very close to vertical and has a smooth sidewall. The height of the feature is ~9.5 μm.

Using the same process flow, trapezoidal cross-section (not fully etched groove) beamsplitter gratings were also demonstrated. In this case the etch is timed to achieve the required groove depth, optimised numerically. The pitch of the grating was measured to be 3.82 μm, with a depth of 170 nm and duty cycle of 35.5 % (**Figure 4.7**) [273].

4.1.2 Triangular grooves

The fabrication of crystallographically etched gratings can be extended to fabricate gratings of purely triangular profile. The fabrication takes advantage of the inherent biasing of the ICP zero-bias etching and the finite selectivity of the ⟨1 1 1⟩ plane. When fabricating V-groove gratings (patterns along the ⟨1 1 0⟩ direction), extended etch times will reveal an undercut of the profile as previously shown (**Figure 4.3**). The evolution of the profile with the etching is shown in **Figure 4.8a**, where the progression of the etch undercuts the bar, shaping the profile from a trapezoid to two opposite triangles. The etch selectivity, and the amount of directional etch contribution influence the dimensions of the triangles. Continuing the etch leads to completion of the undercut and a release of the top triangular beam. Alternatively,

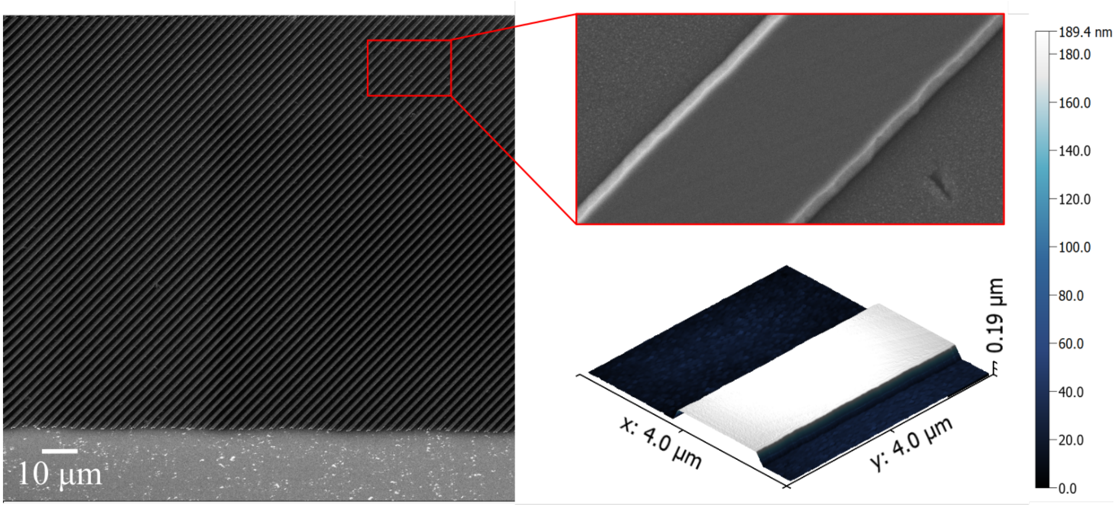

a) b)

Figure 4.7 – Geometrical characterisation of trapezoidal cross-section beamsplitter gratings. **a)** SEM image of resulting grating shows uniformity over large area, with inset showing a single groove **b)** AFM profile shows single grating groove with angled sidewalls, with an etch depth of 170 nm.

the etch may be stopped earlier, and the beams can be mechanically detached. Mechanical detachment (scratching) of the beams can result in particles and debris, so a PDMS-stamp based removal can be a good alternative. The resulting triangles are extremely sharp, if the etch is timed correctly. Three distinct surfaces can be identified (**Figure 4.8a**): the surface marked in green **(A)**, that is unexposed to the directional etching, which will evolve to subtend an angle of 54.7° with respect to the (1 0 0), a true {1 1 1} plane; the surface marked in yellow **(C)**, that is exposed to the directional etching, which will have an angle greater than 54.7°, depending on the directional contribution (~57° in our experiments); and the surface marked in red **(B)**, which is unexposed to the directional etching, but due to the interface between **(B)** and **(C)**, the angle is between 54.7° and the angle of **(C)**.

A disadvantage of this fabrication method is the sensitivity to grating line thickness – difference in grating line thickness translates to a change in undercut time. The total groove depth and undercut time can be expressed based on the known angles, the period and duty cycle (b bar width and g gap width) and the etch rate for each planes (the **(B)** planes are considered to subtend 54.7° with respect to the top surface):

$$h_{total} = 2 \cdot h_1 + h_2 \qquad h_1 = \tan(\alpha)\frac{b}{2} \qquad h_2 = \tan(\alpha')\frac{g}{2} \tag{4.1}$$

$$t_{undercut} = \frac{d_1}{ER_{111}} + \frac{d_2}{ER_{100}} \qquad d_1 = \frac{\cos(\alpha)}{\frac{b}{2}} \qquad d_2 = \tan(\alpha')\frac{g}{2} \tag{4.2}$$

This fabrication method greatly increases fabrication time with respect to trapezoidal gratings,

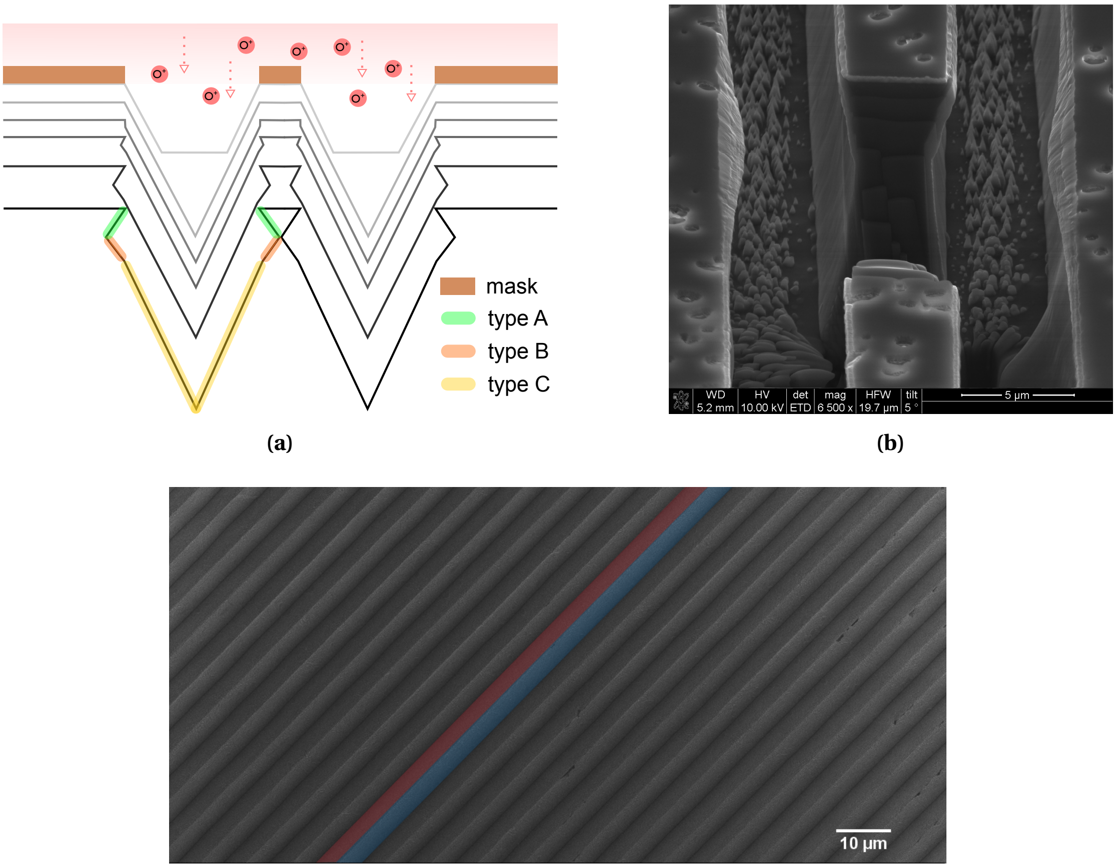

(a) (b) (c)

Figure 4.8 – Triangular groove geometry. **(a)** Evolution of profile during etching and formation of triangular beam and groove profile, with different surface families highlighted **(b)** FIB-cut cross-section showing the evolution of the triangular profile. **(c)** Fully etched large scale triangular profile gratings, with a single ridge highlighted for clarity. The gratings are uniform over a large surface (1 mm).

as the undercut proceeds with low etch rate of the {1 1 1} plane (**Eq.** (4.2)). During long etching, the thermal contact between the diamond plate and carrier wafer can deteriorate and lead to isotropic/thermochemical etching, which roughens the groove surfaces. However, the groove depth is primarily governed by the bar width and can be decreased by a smaller duty cycle, achievable by e-beam lithography (**Eq.** (4.1)). This also translates directly to undercut time, with bar width dominating the etch time (**Eq.** (4.2)). As an example, for a bar and gap width of 500 nm (duty cycle of 50 %), the groove height is 148 nm and the undercut time is 22 min. The etch rates calculated from the etch modelling are in good agreement with the time observed for the undercut, even though the model itself does not reproduce the undercut beam features.

This technique can also be used to undercut square pillars, which result in very sharp tips, which can be of use for micro-indenters and AFM systems.

4.1.3 Limitations

The etching process involves high density plasma to decrease the etching time. High power density heats up the substrate which leads to an isotropic surface roughening due to thermal etching [170]. Consequently, care must be taken to ensure good thermal contact with the backside cooled wafer. Extended etching times can lead to the deterioration of the thermal contact provided by the mounting wax. Thus, lowering the plasma density (by lowering ICP power) or cycling cooling steps [88] could be considered to decrease the thermal load. Imprecise alignment causes undercut of the mask and shifting of the groove centerline, leading to groove asymmetry. This phenomenon is especially pronounced for long grooves and precise alignment of the groove direction with respect to the substrate is required for good control of the groove shape. An alignment technique used for silicon crystallographic etching is a pre-etch [274], where a first etch reveals a crystallographic plane to be used for subsequent alignment. This technique can be used to the same effect for diamond substrates. Another method is to utilize closed groove patterns, which limits the undercut due to trapping of atomic steps [269].

4.2 Deep etching

Fabricating separate components out of single crystal diamond is a useful process, for example for the creation of optical or mechanical devices. This requires an etching process that can etch through thicknesses found in commercially available diamond plates. In the following section, the process for through-etching diamond plates with 150 µm thickness is shown.

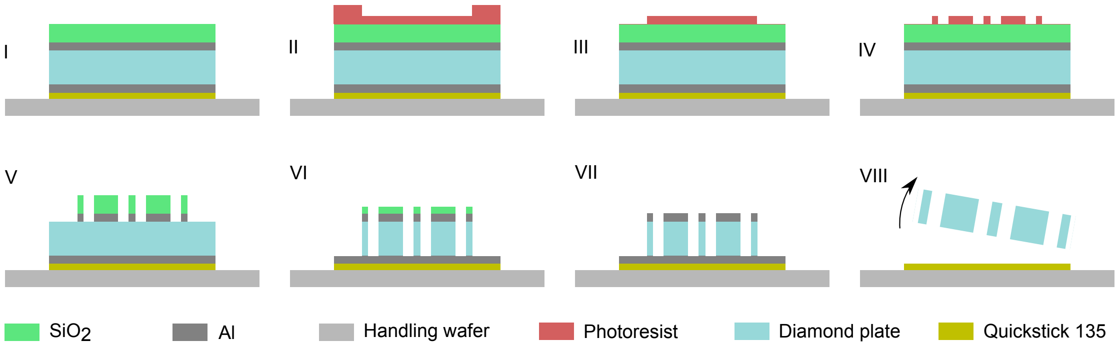

Figure 4.9 – Process flow for creating free-standing components from SCD via deep etching. **I**, Deposition of Al/SiO_2 thin film stack **II-IV**, Dual exposure photolithography **V**, SiO_2 fluorine-based and Al chlorine-based ICP etch **VI**, Deep diamond etch **VII-VIII**, Hardmask stripping and release of components

The fabrication is carried out on single crystal diamond plates, with typical dimensions of 5.5 mm x 5.5 mm x 150 µm (**Figure 4.9**). Several hard mask materials (Al, Si, Al_2O_3, and SiO_2) were experimentally assessed for selectivity against the deep diamond plasma etch. Metal thin films such as Al have previously been used as hard mask materials, because of good adhesion on diamond [275], and high selectivity [276], however metal hard masks generally result in significant micromasking during highly energetic oxygen plasma-based diamond etching [178, 246]. In contrast, dielectric thin films of silicon oxide (SiO_2) or alumina (Al_2O_3) show minimum micromasking effects in pure oxygen plasmas. SiO_2 hard mask was chosen due to the strong reduction of micromasking while exhibiting a good selectivity to the diamond (50:1). However, challenges arose from the thick layer of hard mask needed to etch through the diamond and the low adhesion of silicon oxide layers on diamond [275].

Etching through a 150 µm-thick diamond plate requires a 3 µm-thick SiO_2 hard mask. However, when using a highly biased plasma, hard mask faceting is a commonly encountered issue that leads to angled sidewalls in the etched substrate [242]. A well-known method used to minimize the effects of the hard mask faceting is to use a hard mask thicker than required. For this process, a 7 µm-thick hard mask is used, which is much thicker than usually encountered in common microfabrication processes. This can pose a challenge, as the hard mask layer can delaminate or crack due to low adhesion and internal stress [275, 277]. To avoid the mask from delaminating, a 200 nm-thick Al adhesion layer is used to promote adhesion. In addition, an identical Al layer was deposited on the backside of the diamond plate. This sacrificial layer is used to aid the removal of the individual diamond components when the through-etch is completed. Subsequently, the SiO_2 hard mask was deposited by RF sputtering. Sputtering in a reactive O_2 atmosphere increases the thin-film quality [278], but decreases deposition rate by roughly a factor of five in our experiments. Therefore, a first thin (65 nm) layer of SiO_2 was deposited with O_2 flow, while the remaining 7 µm layer was deposited without O_2, combining good adhesion with fast deposition rates.

The SiO_2 is etched in a $He/H_2/C_4F_8$-based plasma (SPTS APS). The photoresist is stripped afterwards using O_2 plasma, MICROPOSIT REMOVER 1165 solution and a second O_2 plasma cleaning step. In order to smoothen the SiO_2 sidewalls, the substrate is dipped for 15 seconds in a buffered hydrofluoric acid solution (NH_4F(40 %):HF(50 %) (7:1)). The aluminium layer is etched in a Cl_2/BCl_3-based plasma (STS Multiplex ICP), immediately followed by a DI water rinsing and drying under N_2 flow to remove any chlorine residues.

The single crystal diamond substrate is etched for approximately 5 h in O_2 based plasma (2000 W ICP power, 200 W bias power, 100 sccm O_2 flow, 15 mTorr chamber pressure, SPTS APS) until the Al backside layer is reached, with the etch end point determined by visual inspection. The SiO_2 is stripped in concentrated HF bath, and the Al is stripped in Al etchant until the parts are released from the handling Si wafer. Finally, the parts are rinsed in DI water and dried under N_2 flow.

Characterization of the resulting sidewalls reveal two distinct regions: the top region extends 25 µm from the top surface and possesses a taper ($(93.4 \pm 2.7)°$), while the bottom region has a reentrant profile ($(82.0 \pm 1.4)°$) (**Figure 4.10**a). The tapered profile is caused by the erosion and recession of the hard mask during etching, while the bottom profile is caused by isotropic etching. The top region is continuously subjected to ion bombardment incident at angle, which results in a smoothing effect, while the bottom region keeps the striations caused by

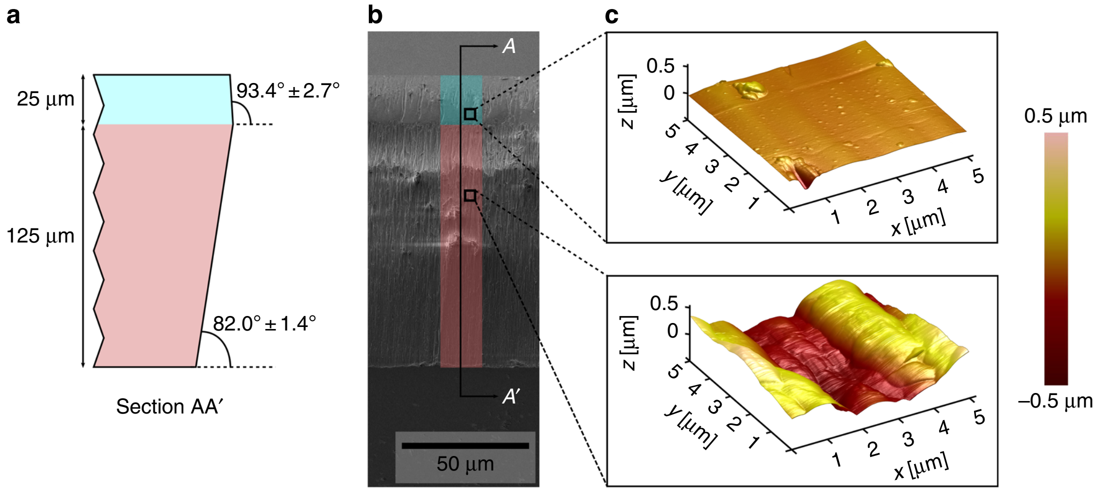

Figure 4.10 – Characterization of the deep etch sidewall. **a)** The sidewall is divided into two distinct areas, with the top part having a tapered profile and smooth surface, and the bottom part possessing a reentrant profile with elevated roughness. **b)** shows the SEM image of the sidewall, with **c)** AFM measurements of the shown areas.

ion damage. The sidewall roughness of the components was measured by AFM. **Figure 4.10b** shows a SEM image of the inspected sidewall, and the corresponding AFM measurements for two selected sites in **Figure 4.10c,d**. The top region of the sidewall exhibits a surface roughness as low as 20 nm rms, while the bottom region shows a surface roughness of about 200 nm rms. These values correspond to the standard deviation of the height in 5 µm x 5 µm areas, after plane fitting (i.e., data centring and tilt removal).

4.3 Vertical etching

Creating etched structures in diamond with smooth, vertical sidewalls is of high importance for creating various optical devices, including waveguides and other integrated optics devices. Such directional etching is also useful for fabricating diffractive optical elements (DOEs). The fabrication of a single crystal diamond binary DOE is shown, along with a discussion on implementing such vertical etching.

Fabrication of the DOEs (**Figure 4.11a**) was carried out on general grade single crystal diamond plates with dimensions of 3 mm x 3 mm x 0.25 mm (Element Six). The plates were cleaned in hot Piranha (H_2SO_4 : H_2O_2, 1:1) and subsequently in concentrated hydrofluoric acid to remove organic and polishing slurry contaminants. During subsequent steps the diamond chip is attached to a carrier wafer using QuickStick 135 mounting wax for handling and compatibility with standard tools (Si for e-beam and oxidised Si during etching).

To remove surface asperities an ion beam etching-based (IBE) polishing process was carried out based on [46]. A first normal incidence etching step removes remaining contamination.

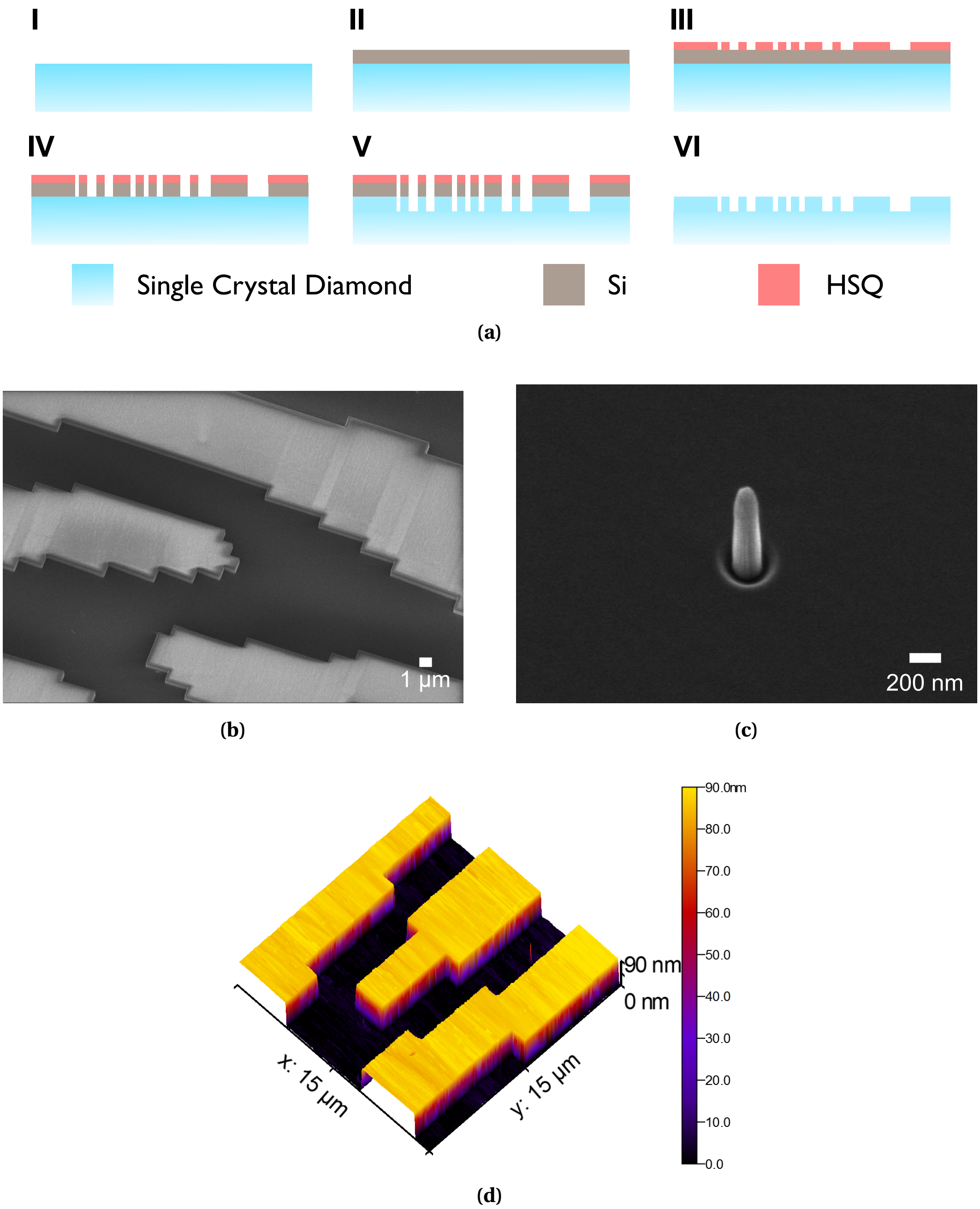

(a)

(b)

(c)

(d)

Figure 4.11 – **Vertical etch fabrication.** (**a**), DOE Microfabrication process flow: **I**, Substrate cleaning, followed by high-angle IBE polishing. **II**, Sputtering of silicon hardmask. **III**, Spin-coating of HSQ negative resist, electron beam lithography (Raith EBPG 5000+), and development in TMAH. **IV**, Cl_2-based ICP RIE patterning of the Si layer (STS Multiplex ICP). **V**, Highly directional O_2 plasma etch of diamond substrate. **VI**, Stripping of the hardmask using a wet silicon isotropic etch. (**b**), SEM image of the diamond DOE after fabrication, showing smooth etch floor and sidewalls. (**c**), SEM image of 180 nm diameter pillar fabricated with the vertical etch. (**d**), AFM image of the DOEs surface showing the 90 nm etch features.

The second, oblique incidence etching performs polishing due to the angle dependent etch rate. The third normal incidence step recovers the nanoscale smoothness. Amorphous silicon was deposited via sputtering to serve as a hardmask. Silicon was chosen due to the good selectivity during the diamond etch, for acting as a conductive layer during electron beam exposure, resistance to the developer (TMAH) and having a good adhesion to both diamond and the electron beam resist. Electron beam lithography (Raith EBPG 5000+) was carried using HSQ negative resist (FOX 16, Dow, thickness ~500 nm). Chlorine chemistry deep reactive ion etching was used to pattern the Si layer (STS Multiplex ICP), after fluorine-based recipes were found to overpassivate the etch surface due to the small exposed area. Transfer of the pattern into diamond was carried using highly directional O_2 plasma (STS Multiplex ICP, 400 W ICP power, 200 W bias power, 30 sccm O_2, 15 mTorr). The etch produces smooth surfaces and vertical sidewalls. The hardmask and HSQ were stripped using a wet silicon isotropic etch ($HF : HNO_3 : CH_3COOH$). The devices were subsequently characterized with SEM and AFM (**Figure 4.11b**, **Figure 4.11d**), which reveal a smooth etch floor and sidewalls.

This vertical etch process was also successfully used to fabricate single crystal diamond pillars for nanomechanical testing, where sidewall angle needs to be as close to 90° as possible. Nanomechanical testing was previously carried out for silicon [279] and microscale glass [280], and currently being carried for single crystal diamond using the fabricated test structures at the Swiss Federal Laboratories for Materials Science and Technology (EMPA). To achieve vertical pillar sidewalls, a hardmask layer was used in addition to HSQ, which is more resistant to the plasma etch (along with the other useful properties listed previously), thereby reducing lateral shrinking of the mask. The other key component of making the etch sufficiently directional, which is mainly governed by increasing the bias power in an ICP system. The drawback of this is the increased erosion of the hardmask due to an increase in the physical etching component (hardmask sputtering) and microtrenching. Pillars with diameters down to 120 nm have been fabricated this way (**Figure 4.11c**), having a height of ~700 nm and a sidewall angle of 88.7°. It is expected that the microtrenching can be reduced by further process optimisation (similar work has been performed for SiC [281]).

4.4 Proportional etching

As previously discussed in **§ 3.4**, 3D printing can be used to create almost arbitrary resist profiles, that can be transferred into diamond using proportional etching, thereby creating tailored surfaces. This method can also be used to fabricate optical structures, that are otherwise difficult or impossible to fabricate using 2D patterning techniques.

The microoptical components are fabricated on a commercially available double side polished CVD general grade single crystal diamond plate (Element Six), with dimensions of 3 mm x 3 mm x 0.3 mm. The samples are cleaned in hot Piranha bath, followed by HF to remove organic and polishing residues. Surface polishing is carried out using ion beam etching based on [46], exploiting the angle-dependent sputtering rate to arrive at a smooth surface. The dia-

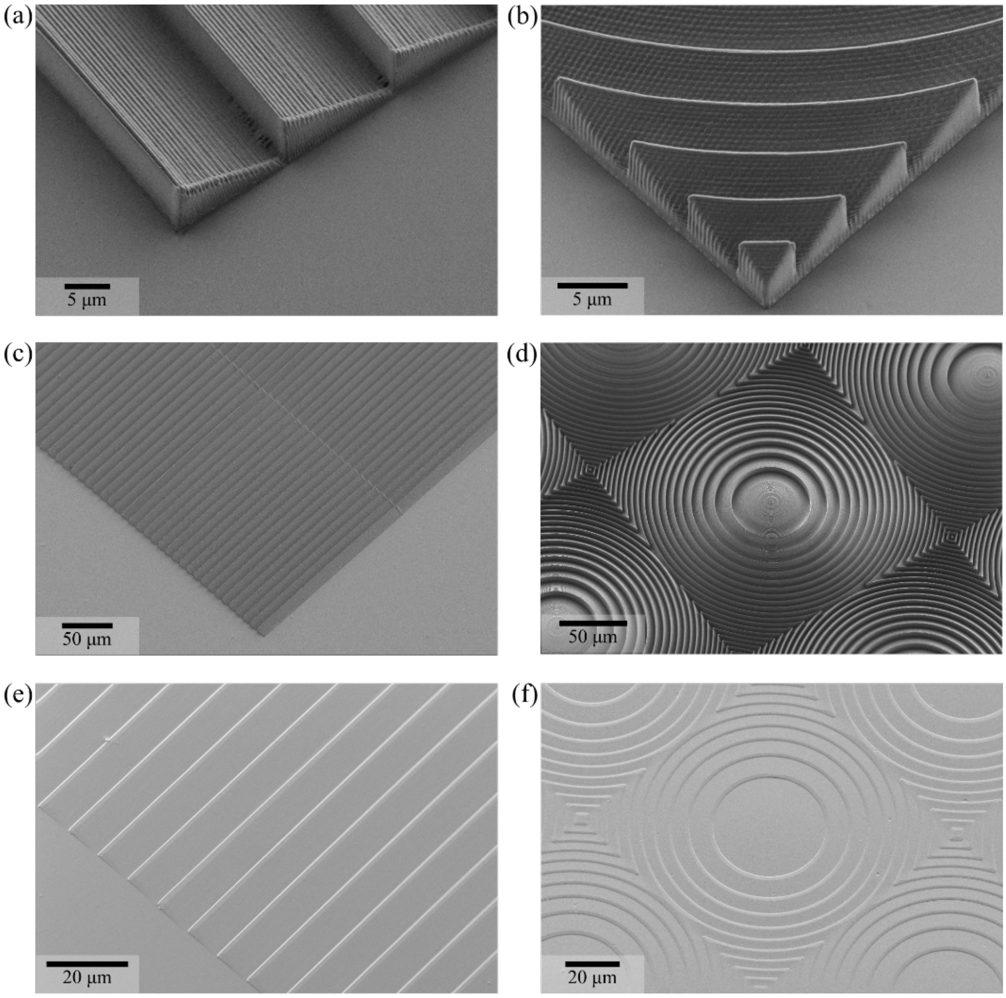

Figure 4.12 – SEM image of blazed diffraction grating (**a), c), e)**) and Fresnel lens (**b), d), f)**). The resist patterns show significant "staircase effect", due to the layer-by-layer printing (**a) - d)**), but this is greatly diminished during the transfer to the diamond substrate due to the low selectivity of the etch (1 : 15) (**e) - f)**).

mond samples are mounted using QuickStick 135 mounting wax in recesses on a prestructured silicon wafer to avoid accidental contact with the objective during the subsequent exposure step. Photoresist (NanoScribe IP-Dip) is dispensed over the chip and exposure is carried out using a 63x magnification objective on the NanoScribe system, followed by development in PGMEA and IPA. After the photoresist structuring, the structures are imaged using SEM, showing a staircase profile due to the layer-by-layer exposure employed by the 3D printing system (**Figure 4.12**).

The patterns in the exposed photoresist are transferred into diamond using a chlorine-based ICP reactive ion etching (STS Multiplex ICP, 800 W coil power, 300 W platen power, 5 mTorr chamber pressure, 40 sccm Cl_2 and 25 sccm Ar, etch rate 64.5 nm min^{-1}). This etch chemistry was found to have improved uniformity and smoothness over the commonly used O_2/Ar.

In addition, the etch has a low selectivity (1 : 15), which allows for the smoothening of the staircase profile observed in the resist layer, leading to a smooth surface (**Figure 4.12**). The diamond chip is detached from the handling wafer before characterisation.

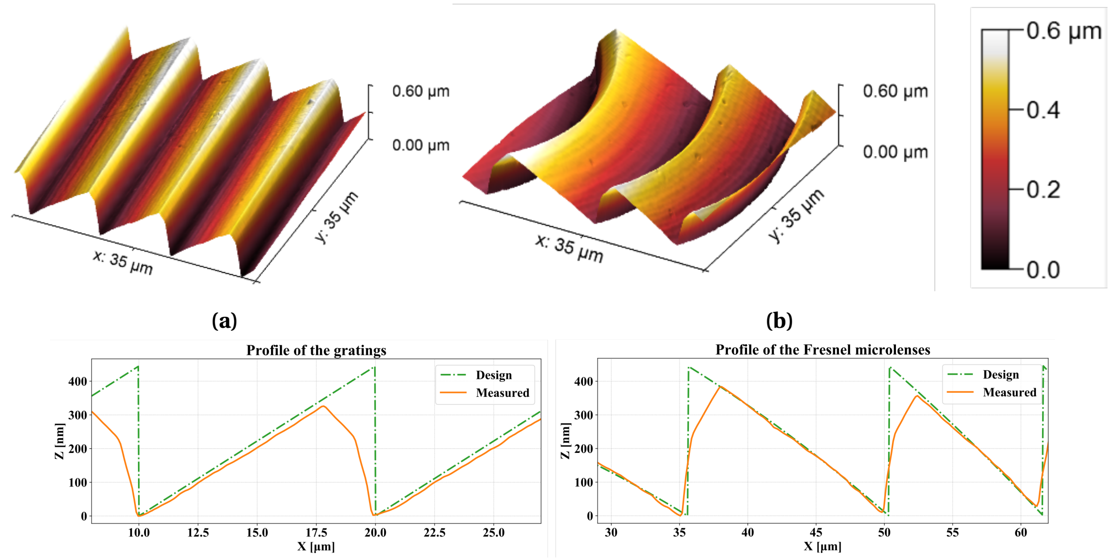

(a) **(b)**

(c) **(d)**

Figure 4.13 – Atomic force microscope (AFM) surface profile of the transferred patterns for **a)** blazed gratings and **b)** Fresnel lenses. In both cases, the surface is smooth. Extracted line scans (**c)**-**d)**) of the grooves match the design profile very closely, showing a deviation of only 3 % for the subtended angle with respect to the top surface. Sharp features of the patterns show rounding due to the low selectivity of the etch, which can be compensated for using a predistorted pattern if required.

The fabricated gratings were subsequently characterised using atomic force microscopy (AFM). The blazed surface subtends an angle of 2.48° to the top surface, deviating by less than 3 % from the targeted value. The period of the grating is (10.2 ± 0.1) µm (<2 % deviation), while the height is (310 ± 10) nm (<30 % deviation). Comparing the etched profile with the design profile (**Figure 4.13c**), it is apparent that edges are eroded during etching and are not transferred into the diamond accurately due to the low selectivity of the process. This effect could be compensated for by pre-distortion of the resist profile. Roughness measurements over a 5 µm x 5 µm reveal an R_a roughness of 2 nm, which shows excellent optical surface quality.

4.5 Discussion and conclusion

Crystallographic etching opens up the possibility of new MEMS and MOEMS structures in the diamond material system. While this type of quasi-3D etching was available for other crystalline materials, it is a relatively new development in diamond. This process was investigated in detail and applied to create relief diffraction gratings of trapezoidal cross-section. Furthermore, the process was employed to fabricate gratings via undercut, forming a triangular groove profile. It is expected that this improved understanding of the process and geometry will lead to novel structures, exploiting the additional degree of freedom of using directionality in a dry etch process.

To explain the origin of this discrepancy, the crystallographic diamond etching was modelled based on previously developed models for crystallographic etching of single crystal silicon (continuous cellular automata method, as described in **§ 4.1.1**). In agreement with the etch model, the angle difference is attributed to a directional anisotropic etching component. The directionality arises from an inherent biasing of the ICP plasma during diamond etching. We expect that this directionality can be tuned or even eliminated with the proper configuration of the plasma etcher, resulting in tunable groove angles.

The crystallographic etch process is very attractive for the fabrication of photonics, as the resulting surfaces are extremely smooth. With measured mean roughness values below 5 nm, these surfaces are comparable in roughness to optically polished diamond substrates. These type of smooth surfaces are advantageous not only for microoptics, but also as waveguide sidewalls, reducing scattering losses.

Diamond deep etching is a promising tool for the fabrication of free-standing mechanical and optical components, allowing the through-etch of 150 µm+ thick plates in a standard microfabrication process. The resulting structures improve upon currently achievable results machined via femtosecond laser cutting, paving the way for the integration of diamond micromechanical assemblies and for microoptical components. Further process optimisation is expected to improve both sidewall roughness (200 nm rms) and verticality (82°), important for decreasing friction in mechanical components and reducing scattering for optical systems.

As a complement to the deep etch, a shallow etch was developed as well. This etch method uses high plasma bias to create sidewalls that are very close to the vertical. This etch method is very useful for creating structures with binary profiles, like diffraction gratings and phase diffractive optical elements, along with mechanical structures. This technique lends itself well to e-beam fabrication, due to the requirement of a hardmask for ensuring conductivity during exposure and produces high-quality sidewalls and etch floor.

3D laser lithography allows the realisation of the almost arbitrary features in resist, which can then be transferred into diamond using proportional etching. This allows the tailoring of the optical surface to practically any degree, such as aspherical and free-form surfaces. As demonstrated, the etching results in excellent optical quality, despite the quantized nature of the writing layer-by-layer. The drawback of this method is the serial nature of the process and the investment into the lithography tool, both of which could be justified for niche applications. However, parallelising or increasing the speed of exposure can enable the scaling of this fabrication technique to industrial exploitation.

5 Characterisation of diamond microoptical devices

Diamond is an excellent optical material due to its high refractive index, broadband transmission window and high thermal conductivity, which enable the construction of compact, broadband, high power optical systems. In this chapter, the optical characterisation of the diamond microoptical devices is shown, along with their predicted performance based on numerical models and measurement results.

Diffraction gratings and diffractive optical elements (DOEs) are widely used in a broad range of industrial and commercial applications, such as in spectrometers [215, 216, 236], beam shapers [282], monochromators [235], beam splitters [237, 245] and beam samplers [283]. In such applications, the extraordinary optical, mechanical and thermal properties of single crystal diamond are of high practical and functional value.

5.1 Crystallographically etched gratings

Single crystal diamond diffraction gratings were fabricated by photolithography, hardmask patterning and crystallographic etching. Based on the fabrication flow shown in **§ 4.1**, diffraction gratings with sidewalls along the {1 0 0} and {1 1 1} planes are fabricated. Using the crystallographic etch method allows the definition of precise angles according to the crystalline planes of the substrate. Diffraction gratings in diamond have been previously published using directional anisotropic etching, exploitation of mask redeposition [242], boron implantation [251] and for x-ray applications [250]. Compared to these fabrication methods, crystallographic etching allows precise control of angles, produces smooth sidewalls free of ion damage and enables high aspect ratio gratings using commonly available microfabrication equipment. In the following section, the optical modelling and characterisation of these gratings is shown.

Optical modelling The diffraction efficiency of the fabricated gratings were calculated with the RETICOLO package [284] using Rigorous Coupled Wave Analysis. The ⟨1 1 0⟩ gratings were approximated by a staircase function of 50 steps (53 nm step height) and both were calculated using 50 Fourier terms (sufficient for convergence). The geometrical parameters were taken from the SEM and AFM measurements. Both $\hat{s}$ and $\hat{p}$ polarisations were extracted to compare against the measured values.

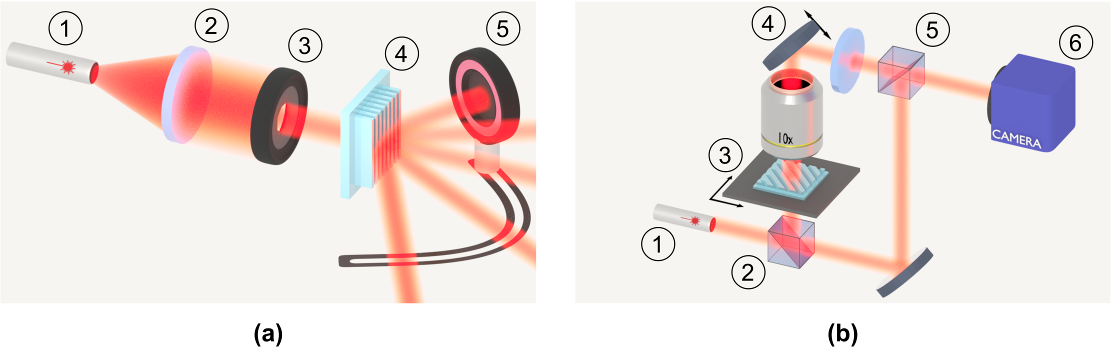

(a) (b)

Figure 5.1 – **(a)** Schematic representation of the optical measurement setup to determine the grating diffraction efficiency. A 635 nm laser **(1)** is collimated **(2)** and sent through an iris **(3)** to match the grating **(4)** dimensions. A photodetector **(5)** is mounted on a goniometer and rotated around the sample. **(b)** Schematic representation of the Mach-Zehnder interferometric microscope for determination of the optical flatness of the diamond gratings. Light from a helium-neon laser **(1)** is split into equal beams **(2)**. One beam is incident on the sample mounted on a stage **(3)** and is collected by a 10x objective before encountering a variable phase shift produced by a piezo-mounted mirror **(4)**. The beams are recombined **(5)**, creating the interference image on the detector **(6)**.

Diffraction efficiency An optical measurement setup was built to measure the diffraction efficiency of the fabricated gratings (**Figure 5.1**). A low-power collimated diode laser (635 nm, 1.2 mW, Thorlabs) illuminates the flat side of the grating mounted on a rotating stage. The diffraction orders are measured with a power sensor mounted on a goniometer. The distance of the power sensor to the sample (10 cm) was chosen to measure only a single order and to ensure the capture of the whole diffracted beam. The detector is rotated to measure the first 6 orders, and the peak values are recorded for each order. Oblique incidence is chosen for the ⟨1 0 0⟩ gratings to improve the contrast for the diffraction orders. At oblique incidence, orders higher than +1 were clipped due to the sample mount and excluded from the results.

Interferometry A Mach-Zehnder interferometric microscope [285] (**Figure 5.1**) was used in transmission to evaluate the optical flatness of the resulting diamond gratings. A 10x objective was used to take multiple phase images of the grating, subsequently stitched by digital image processing. The phase images of the gratings were numerically removed using a low pass Gaussian filter in MATLAB (with a radius of 60 1/µm), then peak-to-valley and rms optical path error was calculated.

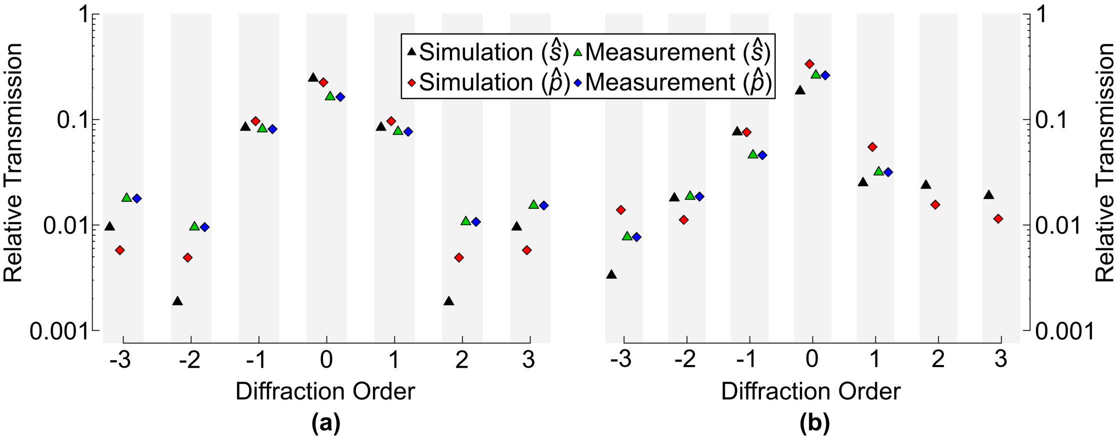

Figure 5.2 – Measured relative transmitted diffraction order efficiency for **(a)** ⟨1 1 0⟩ gratings, with a normal incidence beam, and **(b)** ⟨1 0 0⟩ gratings, with an oblique incident beam ($\phi_i = 41°$), compared to simulated efficiencies. Both $\hat{\mathbf{s}}$ and $\hat{\mathbf{p}}$ polarisations are measured and calculated.

5.1.1 Beamsplitter gratings

The beamsplitter gratings were characterized for optical performance by measuring the efficiency of diffracted orders using a rotating detector arm configuration (**Figure 5.1a**). We chose the operating wavelength to be 650 nm, since the availability of detectors and sources makes the optical measurement easier. The laser light is fiber coupled (for polarization scrambling) and then collimated onto the grating under test. The illumination occurs perpendicular to the grating, incident from the unstructured side of the substrate. The detector arm is rotated and the incident intensity is recorded as a function of the angle. The recorded transmitted optical power as function of detector rotation angle shows an absolute efficiency distribution of 21.1 % in the 0^{th} order and 25.1 % and 23.6 % in the -1^{st} and $+1^{\text{st}}$ orders respectively. The small discrepancy between the $\pm 1^{\text{st}}$ orders is due to the rotation of the sample (the grating lines are slightly off the perpendicular compared to the scanning plane), which will be corrected with an improved sample mounting method in our follow-up work. To evaluate the quality of the fabricated grating, we compare the recorded efficiency to the simulated values based on the measured geometry of the gratings. We use the GD-Calc [286] software with MATLAB to model the grating structure. The grating profile is approximated with a staircase function, with the same illumination conditions as in the measurement setup. A comparison of the measured and simulated grating efficiencies is depicted in **Figure 5.3**.

Comparing the measured and simulated efficiencies show good agreement (0.75 %, 10.28 %, 6.33 % percent error for -1^{st}, 0^{th}, 1^{st} orders respectively), indicating that the model is a good predictor of performance and that the fabricated geometry is close the ideal profile. Of note is the reduced absolute efficiency due to Fresnel losses, which could be improved via a backside anti-reflection coating or backside microstructuring.

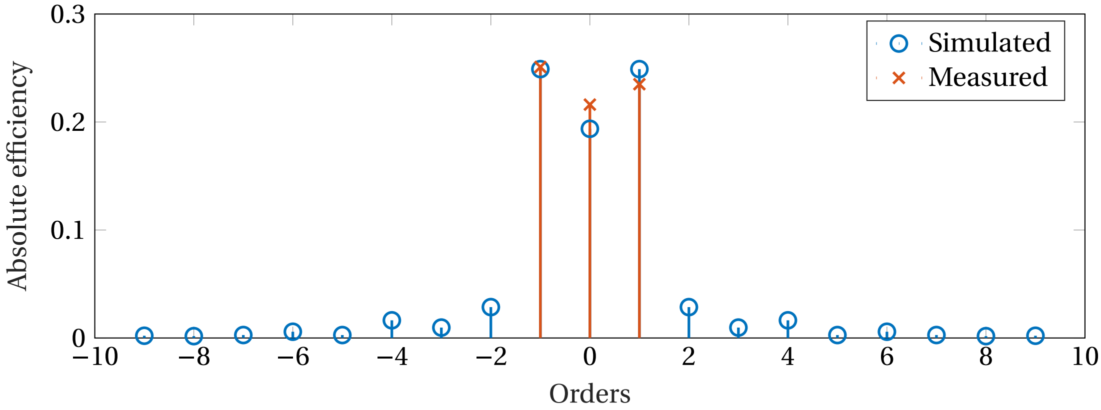

Figure 5.3 – Trapezoidal grating performance. Measured absolute efficiency is plotted against simulated values computed using parameters measured via AFM. Good agreement between the values shows the accuracy of the model and the quality of the fabrication.

5.1.2 Blazed gratings and triangular profile gratings

The advantage of having a precisely controlled grating profile via crystallographic etching is offset by the fact that the fabricated gratings will have a symmetric profile. This means in a practical sense that the no matter the efficiency of the design, the diffraction efficiencies will be symmetric for normal illumination incidence. While this is desirable for beam splitters and beam samplers, for applications that require high diffraction efficiency in a single order, this effectively limits efficiency at 50 %.

To overcome this limitation and fabricate non-symmetric (blazed) gratings, the diamond substrate can be cut at angle to the ⟨1 0 0⟩ direction to produce miscut plates. The geometric construction of such a blazed grating is shown on **Figure 5.4**: following a V-groove grating fabricated in ⟨1 0 0⟩ substrate along the ⟨1 1 0⟩ direction (**Figure 5.4a**), the groove sidewalls are {1 1 1} or quasi-{1 1 1} planes, subtending an angle α (54.7° to 57°) with respect to the {1 0 0} plane. If the substrate is miscut by θ (**Figure 5.4b**), grooves defined in the same will subtend α' ($= \alpha - \theta$) (of note is the angle at between the two sidewalls (β), which remains constant). If this is applied to the fabrication of a blazed grating (**Figure 5.4c**), it can be seen that the resulting grating will have *blaze angle* of α'. Due to the fabrication method, part of the grating surface will be unetched, so the slope will be denoted as d, along with the period D (duty cycle = $\frac{d}{D}$).

By considering the diffraction angle given by the grating equation and taking into account the refraction of the light on the grooves, the wavelength-dependent optimal blaze angle can be derived:

$$\alpha' = \tan^{-}1\left[\frac{Nm\lambda}{n - \sqrt{(1 - Nm\lambda)^2}}\right] \tag{5.1}$$

with n as the refractive index of the substrate, λ the wavelength of operation, m the diffraction

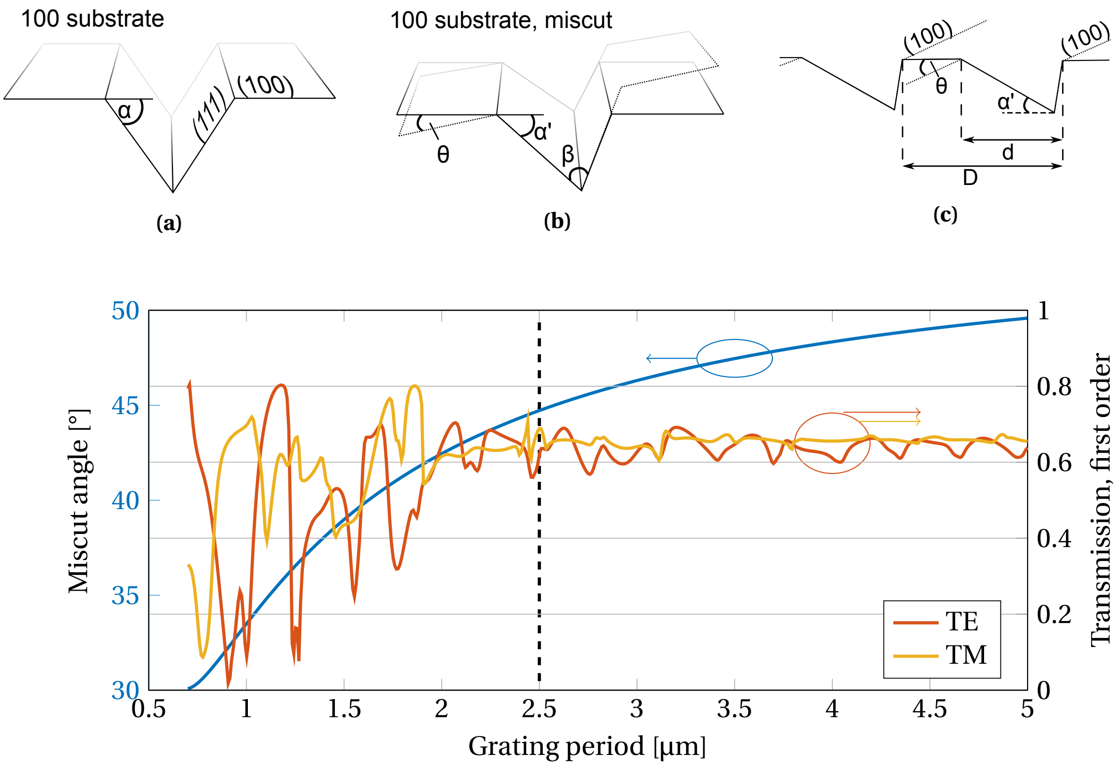

(a) **(b)** **(c)**

(d)

Figure 5.4 – **a)** Geometry of V-groove in a miscut substate, showing miscut angle θ, and the blaze angle α'. The angle β does not depend on the miscut. **b)** Profile of a miscut V-groove blazed grating. Due to the fabrication constraints, the groove width (d) will always be less than the period D. **c)** Theoretical efficiency of the first order, as simulated via RCWA, by setting the blaze angle by **Eq.** (5.1).

order and N the groove density.

The efficiency of the first order ($m = 1$) is plotted against the grating period, with the miscut angle shown as calculated from the optimal blaze angle (**Figure 5.4d**). It can be seen that the efficiency of such grating can be very high (>70 %), but requires a large miscut angle. For example, choosing 2.5 µm grating with a 45° miscut results in a diffraction efficiency close to 70 %, a value which is tolerant to fabrication errors and insensitive to polarisation. However, a 45° miscut is equivalent of a ⟨1 1 0⟩ substrate, which is more difficult to polish. In order to keep the miscut angle smaller, a smaller grating period can be used, but this increases sensitivity to polarisation and makes the grating more wavelength sensitive. In both cases, a larger-than-optimal blaze angle can also be used, which decreases the required miscut at the expense of efficiency.

5.2 Diamond DOEs

In the following section, the characterisation of two types of diamond diffractive elements are shown. The first draws on the fabrication method shown as the vertical etching (**§ 4.3**), the second follows a 3D patterning similar to the flattening technique shown in **§ 3.4**.

5.2.1 Flat-top beam shaper

Demonstration of binary patterning was carried out through the fabrication of a two-level diffractive optical element. The DOE was designed to operate as a flat-top beamshaper, transforming the incoming Gaussian beam into a constant intensity square. The element is designed to operate at 532 nm, the wavelength used for copper welding, where the precise control over the weld pool [287] requires shaping of the incoming high power beam [288, 289].

For operation as a transmission-relief diffractive element, the diamond surface is etched to produce recesses that induce a phase shift in the beam: $\Delta\phi = d \cdot k_0(n_d - 1)$. For a π phase shift in diamond, an etch depth of ~110 nm is required.

The design of the element was carried out using an iterative optimisation. The diffractive element is considered using the Thin Element Approximation (TEA) [290], neglecting effects of a finite thickness substrate. The Iterative Fourier Transform Algorithm (IFTA) [291] is used to optimise the profile of the diffractive element, consisting of a 3000 × 3000 grid of 1 µm × 1 µm pixels. The resulting element shapes the incoming beam into a 600 µm × 600 µm square, with a theoretical diffraction efficiency of approximately 50 % (which can be improved by using more etch levels).

The fabricated elements were characterized using an optical setup. A spatially filtered, expanded and collimated 532 nm laser beam (⌀2 mm $1/e^2$) is incident on the DOE under test. The shaped beam is magnified (3.5x 0.1NA microscope objective) and imaged onto a CMOS sensor (Basler acA1300-30uc).

Figure 5.5 shows the measurements results of the DOE (**Figure 5.5b**), along with simulated intensity (**Figure 5.5c**). The intensity profile is integrated vertically and compared with theoretical performance, showing good agreement (**Figure 5.5d**). The intensity shows sharp transition (2 pixels — 7.5 µm on the object plane) between the outside and inside of the 600 µm square. The 4 : 1 measured contrast is slightly lower than the simulated value due to scattering inside the DOE and the imaging optics. The inset (**Figure 5.5b**, inset) shows the versatility of the modelling method, allowing the definition of arbitrary patterns (such as the EPFL logo).

5.2.2 Blazed gratings and Fresnel lenses by 3D laser lithography

Another approach for creating complex optical surfaces is 3D lithography. The patterns are created by serial exposure via two-photon polymerisation, using the NanoScribe sys-

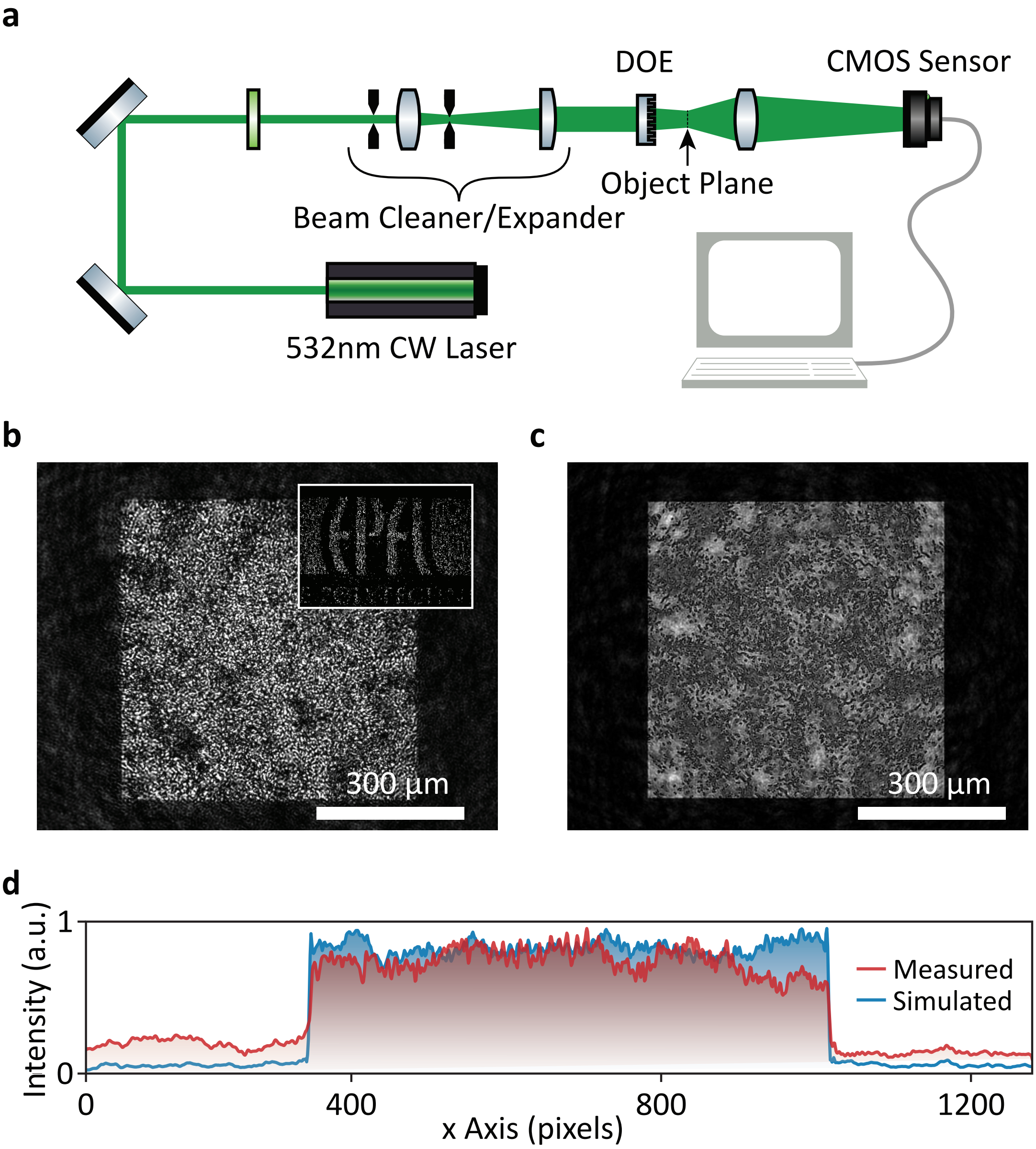

Figure 5.5 – Optical Characterization. a, Experimental set-up, a 532 nm CW laser, a 10 nm band pass filter centered at 532 nm, a spatial filter designed to clean and expand the beam to the required width, the DOE itself, a 3.5x 0.10 NA microscope objective imaging the object plan onto a CMOS array. **b**, Beam profile created by a square beam shaper DOE as imaged by the CMOS detector. Inset: The flexibility of the design and fabrication method is shown by making a beam shaper forming the logo of EPFL. **b**, Simulated beam profile. **d**, Vertically-integrated intensity of the beam profile.

tem (described in detail in **§ 3.4**). Similar to photoresist reflow based lens fabrication [179], proportional reactive ion etching is used to transfer the patterns into the diamond substrate.

A 5 x 5 Fresnel microlens array was fabricated, composed of 200 µm x 200 µm microlenses, with a design focal length of 1 mm, along with blazed gratings with dimensions of 1 mm × 1 mm,

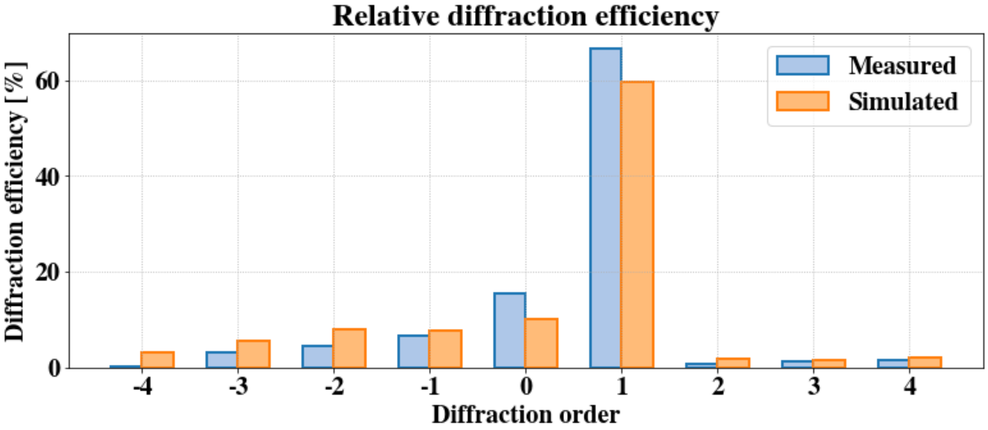

Figure 5.6 – Measured and simulated relative diffraction efficiency of the blazed diffraction gratings. The gratings show a measured maximum relative efficiency of 66 % in the first diffraction order. While the measurements closely match the simulated values, attributed to the discrepancies to the difference between the gratings profile used in the simulation (i.e. a software repetition of a single AFM measured period of the grating) and the actual gratings profile that slightly fluctuates from one period to another.

optimised for diffraction into the first order, with a diffraction angle of 3.6°, a period of 10 µm and a blaze angle of 2.55°. The geometrical characterisation of the devices by AFM/SEM is shown in **§ 4.4**. The structures are optimized for operation at 633 nm, which is the wavelength used for subsequent optical characterisation.

The fabricated blazed gratings were characterized using the goniometer setup previously described in **§ 5.1**, revealing a diffraction efficiency of 66 %, which closely matches the theoretical value predicted by Rigorous Coupled Wave Analysis (Reticolo [284]).

The Fresnel microlenses were measured using a transmission mode Mach-Zehnder microscope interferometer. The focal length is measured by the variation of focus from the base of lens to the focal point, showing a focal length of (960 ± 10) µm (4 % deviation). The transmission of the lens was measured using a 200 µm x 200 µm pinhole to be 48 %.

5.3 Discussion and conclusion

In conclusion, diffraction gratings in a single crystal diamond were successfully manufactured with well-defined sidewall angles and smooth sidewalls, using a fabrication process based on hardmask deposition, lithography and oxygen plasma etching. Using a crystallographic dry etch, grooves were fabricated along the $\langle 110\rangle$ and $\langle 100\rangle$ crystal directions, resulting in V-shaped and vertical groove profiles, respectively. Extensive geometrical and optical characterization was performed to assess the quality of the produced devices, which show that the resulting devices are optically flat (peak-to-valley flatness:$< \lambda/2$) and their diffraction efficiencies are close to what is predicted by simulations of the idealised groove profile.

The gratings fabricated with this method exhibit outstanding quality similar to the ones available in the silicon material system. We believe that this synergy allows the adaptation of existing designs for silicon-based diffractive elements to single crystal diamond, exploiting the broadband transmission window (including visible wavelengths) and the inherent high damage threshold. The shown fabrication method can be further refined to provide a scalable process enabling high quality single crystal diffraction gratings, with smoother sidewalls and improved grating uniformity.

Using the same process flow, single crystal diamond beamsplitters were also demonstrated with a trapezoidal profile. The gratings were characterized using SEM, AFM and optically, showing a trapezoidal profile with a pitch of 3.82 µm, depth of 170 nm and duty cycle of 35.5 %. The absolute diffraction efficiencies of the grating are measured, which are 21.1 % in the 0^{th} order and 25.1 % and 23.6 % for the + and -1^{st} orders respectively (16.6 % is attributed to higher orders and 16.1 % to reflection based on modelling). The fabricated gratings are modelled based on the measured geometry parameters and the diffraction efficiencies are simulated. The theoretical diffraction efficiencies are compared to the measured values show a good fit (deviation $\leq$ 10.28 % for the measured orders), indicating that the simulation is a good predictor of grating performance and that the grating fabrication process is suitable for producing gratings of desired properties.

As shown, this process can be extended to fabricate blazed gratings, by exploiting substrates miscut with respect to the $\langle 100 \rangle$ direction. In these substrates, asymmetric groove profiles can be realised, which are key to achieving high diffraction efficiency. However, large miscut angles are required for this method, which requires close collaboration with diamond substrate manufacturers. Ideally, the etch process needs to be tuned to eliminate biasing, as that can distort angles.

Using a different fabrication technique, binary diffractive optical elements in single crystal diamond were shown, which can generate arbitrary patterns in the object plane. This is of high practical value for the production of DOEs for the use in high-power applications which benefit from the excellent optical and thermal properties of SCD. The measured results show good agreement with the simulated intensity, but further improvements can be made both in the design and fabrication phase such as the use of a greater number of z-levels, which can by itself greatly improve the diffraction efficiency of the devices and the addition of anti-reflection coatings or patterns to reduce Fresnel reflection. Furthermore, the fabrication process can be easily adapted to photolithography, enabling large scale commercial exploitation.

3D laser lithography is an extremely versatile fabrication technique. As shown here, the process of realizing the almost arbitrary surface can be very well tuned to produce the desired optical performance. While some discrepancies still exist between the design and measurement values, it is expected that the additional fabrication experience will result in devices that match the specification. Furthermore, this process can also be straightforwardly combined with anti-reflection coatings or structures.

6 Conclusion and outlook

In this thesis the microfabrication and characterisation of single crystal diamond photonic and microoptic microsystems were shown.

In the first part, the design and fabrication of a diamond-on-insulator platform was shown. A thin diamond membrane was successfully created via helium ion implantation induced graphitisation and annealing. The implanted diamond sample was characterized via TEM, before it was bonded via HSQ – adhesive bonding to a carrier substrate. Electrochemical etching of the graphitised layer allowed the release of single crystal membranes bonded to the carrier substrate. The membranes show smooth surface and preserve the crystallinity of the original substrate. Subsequent patterning using e-beam lithography and etching was demonstrated, along with the release of the structures to form free-standing structures. The success of this technique demonstrates the viability of the layer transfer process via die-to-wafer bonding.

Furthermore, the demonstration of substrate surface quality improvement was demonstrated via IBE and 3D printing-based flattening. A 4-fold topography reduction was shown compared to the as-received sample, while the surface roughness of the substrate was preserved. This technique paves the way for the flattening and wedge error elimination of optical substrates. Furthermore this approach allows the reduction of topography of diamond plates sufficiently to make direct bonding feasible. It is expected that combining this technique with the DOI fabrication process will yield full die-scale bonding and release of diamond membranes. Furthermore the fabrication can be extended into a full photonic platform, where passive devices can be integrated with diamond-specific components, such as colour centres.

In the second part, this thesis aimed at putting forward a number of fabrication techniques that enable creating diamond microoptical devices that can compete in quality with ones in other material systems. Diffraction gratings were demonstrated using crystallographic diamond etching. This technique was investigated in detail, supported with modelling and characterisation of the resulting devices, geometrically and optically. Furthermore, the plasma through-etching of diamond was demonstrated for 150 μm-thick plates, creating surfaces that greatly improve upon laser-cut surfaces of same depth. Furthermore, shallow, highly vertical etching of diamond was shown, and used to create diffractive beam shapers and pillars for nanomechanical testing. Finally, 3D printing and proportional etching was shown to fabricate diffractive microoptical devices. The microoptical devices were characterised for their optical properties and compared to simulation predicted performance to qualify the fabrication process.

Diamond competes with fused silica, sapphire and silicon in the microoptical substrate field. It can be argued that all of these materials possess remarkable properties — but diamond does surpass all, especially for the visible. In particular, a remarkable property not seen in these other materials is the thermal conductivity, which gives diamond an edge in high power applications. Diamond has the highest refractive index for the visible among these materials, which can be an advantage over silica and sapphire, provided appropriate coating or anti-reflective microstructuring is used that negates Fresnel losses. Diamond microoptics faces challenges in substrate size: commercially single crystal substrates have sufficient quality for production of microoptical devices, but the size of these substrates are small compared to ones available for sapphire or fused silica, or the ones of larger size are prohibitively expensive. This situation is expected to improve with the maturing of diamond substrate technologies and the increase in demand for plate-type substrates — however, as long as diamonds remain valuable gemstones to be used in the jewellery industry, substrates for microoptical applications will have to compete for large stones that are prized jewels as well. However, in specific niches well suited for diamond substrates (high power, compact optics in the visible), diamond microoptics can thrive and find commercial exploitation after the demonstration of the proof-of-concept devices.

A Publication list

P01 **Marcell Kiss**, Teodoro Graziosi, Adrien Toros, Toralf Scharf, Christian Santschi, Olivier J. F. Martin and Niels Quack. "High Quality Single Crystal Diamond Diffraction Gratings Fabricated by Crystallographic Etching". Optics Express, vol. 27, no. 21, pp. 30371–30379, October 2019.

P02 **Marcell Kiss**, Teodoro Graziosi and Niels Quack, “Trapezoidal diffraction grating beam splitters in single crystal diamond”, Proceedings Volume 10513, Components and Packaging for Laser Systems IV, pp. 10513-10513–6, 2018.

P03 Thibault Wildi, **Marcell Kiss**, and Niels Quack, “Diamond Diffractive Optical Beamshapers for High Power Applications”, Optics Letters, *in preparation.*

P04 Adrien Toros, Nathanaël Restori, **Marcell Kiss**, Toralf Scharf, and Niels Quack, “Single crystal diamond blazed diffraction gratings and Fresnel microlens arrays by high-resolution 3D laser lithography and pattern transfer by dry etching”. *in review*

P05 **Marcell Kiss**, Teodoro Graziosi and Niels Quack, “Demonstration of V-groove diffraction gratings in single crystal diamond”, oral presentation at the International Conference on Diamond and Carbon Materials, Gothenburg, September 2017.

P06 **Marcell Kiss**, Teodoro Graziosi, Adrien Toros, Toralf Scharf, Christian Santschi, Olivier J. F. Martin and Niels Quack, “Characterization of Crystallographically Etched Single Crystal Diamond Gratings” oral presentation at the Symposium Latsis 2019 on Diamond Photonics, Lausanne, May 2019.

P07 Sichen Mi, Christian Santschi, **Marcell Kiss**, Olivier J. F. Martin, and Niels Quack, “Size Control of Self-Organized Gold Nanoparticles on Nanopatterned Single Crystal Diamond,” in 2018 International Conference on Optical MEMS and Nanophotonics (OMN), Lausanne, Switzerland, 2018, pp. 1–5.

P08 Teodoro Graziosi, Sichen Mi, **Marcell Kiss**, and Niels Quack, “Single crystal diamond micro-disk resonators by focused ion beam milling,” APL Photonics, vol. 3, no. 12, p. 126101, December 2018.

P09 Hamed Sattari, Teodoro Graziosi, **Marcell Kiss**, Tae Joon Seok, Ming C. Wu and Niels Quack, “Silicon Photonic MEMS Phase-Shifter,” Opt. Express, OE, vol. 27, no. 13, pp. 18959–18969, June 2019.

P10 Jonas Jacobs, Teodoro Graziosi, **Marcell Kiss**, Sangyoon Han, Tae Joon Seok, Ming C. Wu and Niels Quack, “Die level release of silicon photonic MEMS,” presented at the International Conference on Optical MEMS and Nanophotonics, September 2016.

P11 Adrien Toros, **Marcell Kiss**, Teodoro Graziosi, Hamed Sattari, Pascal Gallo and Niels Quack, "Precision Micro-Optical Components in Single Crystal Diamond by Deep Reactive Ion Etching", presentation at the Symposium Latsis 2019 on Diamond Photonics, Lausanne, May 2019.

P12 **Marcell Kiss**, Teodoro Graziosi, Niels Quack, "Single Crystalline Diamond Diffractive Optical Elements and Method of Fabricating the same", PCT/IB2018/056547 - **WO 2019/043570 A1**.

P13 Adrien Toros, **Marcell Kiss**, Teodoro Graziosi, Pascal Gallo, Niels Quack, "Single Crystalline Diamond Part Production Method for Stand Alone Single Crystalline Mechanical and Optical Component Production", PCT/IB2017/055200 - **WO 2019/043432 A1**.

P14 Gergely Huszka, Niels Quack, **Marcell Kiss**, "Optical element with high reflection at a first wavelength and low reflection at a different second Wavelength.", PCT/IB2019/055441.

P15 **Marcell Kiss**, Teodoro Graziosi, Niels Quack, Nathanaël Restori, "Method for flattening of substrates using 3D printing and proportional etching", PCT/IB2019/057909.

For the publications from the previous list that have been used in the preparation of this thesis, my contribution is listed below.

P01 Design and carry-out of microfabrication, geometrical and optical characterisation, simulation code design, writing of the manuscript.

P02 Optical design, design and carry-out of microfabrication, geometrical and optical characterisation, writing of the manuscript.

P03 Designed process flow, performed part of processing and manuscript authoring.

P04 Designed measurement setup, contributed to NanoScribe setup & reviewed manuscript and measurement data preparation.

P05 Design and carry-out of microfabrication, geometrical and optical characterisation, preparation of presentation and poster.

P06 Design and carry-out of microfabrication, geometrical and optical characterisation, simulation code design, preparation of presentation and poster.

B Copyright licenses

Figure 2.1B This work is licensed under a Creative Commons Attribution 4.0 International License.

Figure 2.2A This work is licensed under CC BY NC SA.

Figure 2.3B Reprinted with permission from Burek, de Leon, Shields, Hausmann, Chu, Quan, Zibrov, Park, Lukin, and Lončar, “Free-Standing Mechanical and Photonic Nanostructures in Single-Crystal Diamond”, 2012. Copyright 2012 American Chemical Society.

Figure 2.4 Reprinted with permission from Khanaliloo, Mitchell, Hryciw, and Barclay, “High-Q / V Monolithic Diamond Microdisks Fabricated with Quasi-Isotropic Etching”, 2015. Copyright 2015 American Chemical Society.

Figure 2.5 Rightslink 4687601161086. Reprinted by permission from Springer Nature.Faraon, Barclay, Santori, Fu, and Beausoleil, “Resonant Enhancement of the Zero-Phonon Emission from a Colour Centre in a Diamond Cavity”, 2011.

Figure 2.6A Rightslink 4687601452487.

Figure 2.6B Rightslink 4687541386342.

Figure 2.7 Rightslink 4687541458210. Reprinted with permission from Wang, Hu, Yang, and Butler, “Fabrication of Suspended Single Crystal Diamond Devices by Electrochemical Etch”, 2007. Copyright 2007, American Vacuum Society.

Figure 2.8A Piracha, Ganesan, Lau, Stacey, McGuinness, Tomljenovic-Hanic, and Prawer, “Scalable Fabrication of High-Quality, Ultra-Thin Single Crystal Diamond Membrane Windows”, 2016 - Published by The Royal Society of Chemistry.

Figure 2.8B Reprinted with permission from Piracha, Rath, Ganesan, Kühn, Pernice, and Prawer, “Scalable Fabrication of Integrated Nanophotonic Circuits on Arrays of Thin Single Crystal Diamond Membrane Windows”, 2016. Copyright 2016 American Chemical Society.

Figure 2.9A Rightslink 4687610638317. Reprinted from Hickey, Jones, and Elliman, "Amorphization and Graphitization of Single-Crystal Diamond — A Transmission Electron Microscopy Study", 2009, with permission from Elsevier.

Figure 2.9B Rightslink 4687541386342.

Figure 2.11A This work is licensed under CC BY NC ND.

Figure 2.11B This work is licensed under CC BY.

Figure 2.12A © 2003 Optical Society of America. Users may use, reuse, and build upon the article, or use the article for text or data mining, so long as such uses are for non-commercial purposes and appropriate attribution is maintained. All other rights are reserved.

Figure 2.12B Rightslink 4687620894097. Reprinted from Forsberg and Karlsson, "High Aspect Ratio Optical Gratings in Diamond", 2013, with permission from Elsevier.

Figure 2.13A Rightslink 4687550607557. Reprinted from Makita, Karvinen, Guzenko, Kujala, Vagovic, and David, "Fabrication of Diamond Diffraction Gratings for Experiments with Intense Hard X-Rays", 2017, with permission from Elsevier.

Figure 2.13B Rightslink 4687550685213. Reprinted by permission from Springer Nature.Stepanov, Nuzhdin, Galyautdinov, Kurbatova, Valeev, Vorobev, and Osin, "A Diffraction Grating Created in Diamond Substrate by Boron Ion Implantation", 2017.

Figure 3.15a,Figure 3.15b Rightslink 4687550741087. Reprinted from Gui, Elwenspoek, Tas, and Gardeniers, "The Effect of Surface Roughness on Direct Wafer Bonding", 1999, with the permission of AIP Publishing.

Figure 3.15c Rightslink 4687550844943. Reprinted from Tong and Gösele, "Semiconductor Wafer Bonding", 1994, with permission from Elsevier.

Bibliography

[1] *Silicon Photonics and Photonic Integrated Circuits 2019*, en-US, https://www.i-micronews.com/products/silicon-photonics-and-photonic-integrated-circuits-2019/.

[2] H. R. Phillip and E. A. Taft, “Kramers-Kronig Analysis of Reflectance Data for Diamond”, *Phys. Rev.*, vol. 136, no. 5A, A1445–A1448, 1964.

[3] H. H. Li, “Refractive index of silicon and germanium and its wavelength and temperature derivatives”, *Journal of Physical and Chemical Reference Data*, vol. 9, no. 3, pp. 561–658, 1980.

[4] I. H. Malitson, “Refraction and Dispersion of Synthetic Sapphire”, EN, *JOSA*, vol. 52, no. 12, pp. 1377–1379, 1962.

[5] I. H. Malitson, “Interspecimen Comparison of the Refractive Index of Fused Silica*,†”, EN, *JOSA*, vol. 55, no. 10, pp. 1205–1209, 1965.

[6] P. Rath, S. Ummethala, C. Nebel, and W. H. P. Pernice, “Diamond as a material for monolithically integrated optical and optomechanical devices: Diamond as a material for integrated optical and optomechanical devices”, en, *physica status solidi (a)*, vol. 212, no. 11, pp. 2385–2399, 2015.

[7] B. Bhushan and X. Li, “Micromechanical and tribological characterization of doped single-crystal silicon and polysilicon films for microelectromechanical systems devices”, en, *Journal of Materials Research*, vol. 12, no. 1, pp. 54–63, 1997.

[8] T. Chudoba, P. Schwaller, R. Rabe, J.-M. Breguet, and J. Michler, “Comparison of nanoindentation results obtained with Berkovich and cube-corner indenters”, *Philosophical Magazine*, vol. 86, no. 33-35, pp. 5265–5283, 2006.

[9] P. Hess, “The mechanical properties of various chemical vapor deposition diamond structures compared to the ideal single crystal”, *Journal of Applied Physics*, vol. 111, no. 5, p. 051 101, 2012.

[10] S. Reilly, V. G. Savitski, H. Liu, E. Gu, M. D. Dawson, and A. J. Kemp, “Monolithic diamond Raman laser”, en, *Optics Letters*, vol. 40, no. 6, p. 930, 2015.

[11] A. M. Zaitsev, *Optical Properties of Diamond: A Data Handbook*, en. Berlin Heidelberg: Springer-Verlag, 2001.

[12] I. Aharonovich, S. Castelletto, D. A. Simpson, C.-H. Su, A. D. Greentree, and S. Prawer, “Diamond-based single-photon emitters”, en, *Reports on Progress in Physics*, vol. 74, no. 7, p. 076 501, 2011.

[13] L. T. Hall, J. H. Cole, C. D. Hill, and L. C. L. Hollenberg, “Sensing of Fluctuating Nanoscale Magnetic Fields Using Nitrogen-Vacancy Centers in Diamond”, *Physical Review Letters*, vol. 103, no. 22, p. 220 802, 2009.

[14] J. M. Taylor, P. Cappellaro, L. Childress, L. Jiang, D. Budker, P. R. Hemmer, A. Yacoby, R. Walsworth, and M. D. Lukin, “High-sensitivity diamond magnetometer with nanoscale resolution”, en, *Nature Physics*, vol. 4, no. 10, pp. 810–816, 2008.

[15] A. Ajoy and P. Cappellaro, “Stable three-axis nuclear-spin gyroscope in diamond”, *Physical Review A*, vol. 86, no. 6, p. 062 104, 2012.

[16] R. Schirhagl, K. Chang, M. Loretz, and C. L. Degen, “Nitrogen-Vacancy Centers in Diamond: Nanoscale Sensors for Physics and Biology”, *Annual Review of Physical Chemistry*, vol. 65, no. 1, pp. 83–105, 2014.

[17] S. C. Rand and L. G. DeShazer, “Laser Action of H3 Color Center in Diamond”, en, in *Tunable Solid State Lasers for Remote Sensing*, R. L. Byer, E. K. Gustafson, and R. Trebino, Eds., ser. Springer Series in Optical Sciences, Springer Berlin Heidelberg, 1985, pp. 146–146.

[18] K. Bray, H. Kato, R. Previdi, R. Sandstrom, K. Ganesan, M. Ogura, T. Makino, S. Yamasaki, A. P. Magyar, M. Toth, and I. Aharonovich, “Single crystal diamond membranes for nanoelectronics”, en, *Nanoscale*, vol. 10, no. 8, pp. 4028–4035, 2018.

[19] Carlos Errando-Herranz, Alain Yuji Takabayashi, Pierre Edinger, Hamed Sattari, Kristinn B. Gylfason, and Niels Quack, “MEMS for Photonic Integrated Circuits”, 2019, under review.

[20] W. C. Jiang, X. Lu, J. Zhang, and Q. Lin, “High-frequency silicon optomechanical oscillator with an ultralow threshold”, *Opt. Express*, vol. 20, no. 14, p. 15 991, 2012.

[21] F. Peter, “Uber brechungsindizes und absorptionskonstanten des diamanten zwischen 644 und 226 mu”, de, *Zeitschrift fur Physik*, vol. 15, no. 1, pp. 358–368, 1923.

[22] E. Anoikin, A. Muhr, A. Bennett, D. Twitchen, and H. de Wit, “Diamond optical components for high-power and high-energy laser applications”, A. L. Glebov and P. O. Leisher, Eds., 2015, 93460T.

[23] M. S. Komlenok, P. A. Pivovarov, B. O. Volodkin, V. S. Pavelyev, V. I. Anisimov, V. V. Butuzov, V. R. Sorochenko, S. M. Nefedov, A. P. Mineev, V. A. Soifer, and V. I. Konov, “High-damage-threshold antireflection coatings on diamond for CW and pulsed CO2 lasers”, en, *Laser Physics Letters*, vol. 15, no. 3, p. 036 001, 2018.

[24] T. K. Yeung, D. Le Sage, L. M. Pham, P. L. Stanwix, and R. L. Walsworth, “Anti-reflection coating for nitrogen-vacancy optical measurements in diamond”, en, *Applied Physics Letters*, vol. 100, no. 25, p. 251 111, 2012.

[25] P. Forsberg and M. Karlsson, “Inclined surfaces in diamond: broadband antireflective structures and coupling light through waveguides”, en, *Optics Express*, vol. 21, no. 3, p. 2693, 2013.

[26] *Diamond PureOptics*, https://asia.e6.com/en/Home/Applications/Optics/High+power+laser+optics/Diamond+PureOptics/.

[27] S. Sun, Z. Xu, W. Cui, J. Lv, Y. Geng, H. Li, X. Jia, and H.-a. Ma, “The study on the diamond growth and morphology from light elements (N-B-H)synergistic doping systems under HPHT”, *International Journal of Refractory Metals and Hard Materials*, vol. 70, pp. 169–175, 2018.

[28] S. Eaton-Magaña, J. E. Shigley, and C. M. Breeding, “Observations on HPHT-Grown Synthetic Diamonds: A Review”, *Gems & Gemology*, 2017.

[29] U. F. D’Haenens-Johansson, A. Katrusha, K. S. Moe, P. Johnson, and W. Wang, “Large Colorless HPHT-Grown Synthetic Gem Diamonds from New Diamond Technology, Russia”, *Gems & Gemology*, 2015.

[30] C.-s. Yan, Y. K. Vohra, H.-k. Mao, and R. J. Hemley, “Very high growth rate chemical vapor deposition of single-crystal diamond”, *Proceedings of the National Academy of Sciences of the United States of America*, vol. 99, no. 20, pp. 12 523–12 525, 2002.

[31] T. Chakraborty, F. Lehmann, J. Zhang, S. Borgsdorf, N. Wöhrl, R. Remfort, V. Buck, U. Köhler, and D. Suter, “CVD growth of ultrapure diamond, generation of NV centers by ion implantation, and their spectroscopic characterization for quantum technological applications”, *Physical Review Materials*, vol. 3, no. 6, p. 065 205, 2019.

[32] W. Wang, U. F. S. D’Haenens-Johansson, P. Johnson, K. S. Moe, E. Emerson, M. E. Newton, and T. M. Moses, “CVD Synthetic Diamonds from Gemesis Corp.”, *Gems & Gemology*, vol. 48, no. 2, pp. 80–97, 2012.

[33] *Diamond Book Download*, https://e6cvd.com/us/diamond-book-download.

[34] M. Schreck, S. Gsell, R. Brescia, and M. Fischer, “Ion bombardment induced buried lateral growth: the key mechanism for the synthesis of single crystal diamond wafers”, en, *Scientific Reports*, vol. 7, no. 1, 2017.

[35] R. Nelz, J. Görlitz, D. Herrmann, A. Slablab, M. Challier, M. Radtke, M. Fischer, S. Gsell, M. Schreck, C. Becher, and E. Neu, “Toward wafer-scale diamond nano- and quantum technologies”, en, *APL Materials*, vol. 7, no. 1, p. 011 108, 2019.

[36] H. Yamada, A. Chayahara, H. Umezawa, N. Tsubouchi, Y. Mokuno, and S. Shikata, “Fabrication and fundamental characterizations of tiled clones of single-crystal diamond with 1-inch size”, *Diamond and Related Materials*, vol. 24, pp. 29–33, 2012.

[37] M. Naamoun, A. Tallaire, P. Doppelt, A. Gicquel, M. Legros, J. Barjon, and J. Achard, “Reduction of dislocation densities in single crystal CVD diamond by using self-assembled metallic masks”, en, *Diamond and Related Materials*, vol. 58, pp. 62–68, 2015.

[38] H. Yamada, A. Chayahara, Y. Mokuno, N. Tsubouchi, and S.-i. Shikata, “Uniform growth and repeatable fabrication of inch-sized wafers of a single-crystal diamond”, *Diamond and Related Materials*, vol. 33, pp. 27–31, 2013.

[39] J. R. Hird, “Polishing and Shaping of Monocrystalline Diamond”, en, in *Optical Engineering of Diamond*, R. P. Mildren and J. R. Rabeau, Eds., Weinheim, Germany: Wiley-VCH Verlag GmbH & Co. KGaA, 2013, pp. 71–107.

[40] Hird J. R. and Field J. E., “Diamond polishing”, *Proceedings of the Royal Society of London. Series A: Mathematical, Physical and Engineering Sciences*, vol. 460, no. 2052, pp. 3547–3568, 2004.

[41] T. Schuelke and T. A. Grotjohn, “Diamond polishing”, *Diamond and Related Materials*, vol. 32, pp. 17–26, 2013.

[42] N. Tatsumi, K. Harano, T. Ito, and H. Sumiya, “Polishing mechanism and surface damage analysis of type IIa single crystal diamond processed by mechanical and chemical polishing methods”, *Diamond and Related Materials*, 9th International Conference on New Diamond and Nano Carbons – NDNC 2015, vol. 63, pp. 80–85, 2016.

[43] Y. Lin, J. Lu, R. Tong, Q. Luo, and X. Xu, “Surface damage of single-crystal diamond (100) processed based on a sol-gel polishing tool”, *Diamond and Related Materials*, vol. 83, pp. 46–53, 2018.

[44] T. E. Derry, N. van der Berg, and N. W. Makau, “Diamond surfaces polished both mechanically and manually; an atomic force microscopy (AFM) study”, *Diamond and Related Materials*, vol. 17, no. 2, pp. 127–136, 2008.

[45] I. Friel, S. L. Clewes, H. K. Dhillon, N. Perkins, D. J. Twitchen, and G. A. Scarsbrook, “Control of surface and bulk crystalline quality in single crystal diamond grown by chemical vapour deposition”, *Diamond and Related Materials*, Proceedings of Diamond 2008, the 19th European Conference on Diamond, Diamond-Like Materials, Carbon Nanotubes, Nitrides and Silicon Carbide, vol. 18, no. 5, pp. 808–815, 2009.

[46] S. Mi, A. Toros, T. Graziosi, and N. Quack, “Non-contact polishing of single crystal diamond by ion beam etching”, en, *Diamond and Related Materials*, vol. 92, pp. 248–252, 2019.

[47] M. Naamoun, A. Tallaire, F. Silva, J. Achard, P. Doppelt, and A. Gicquel, “Etch-pit formation mechanism induced on HPHT and CVD diamond single crystals by H_2/O_2 plasma etching treatment: Part of Topical Section on Fundamentals and Applications of Diamond”, en, *physica status solidi (a)*, vol. 209, no. 9, pp. 1715–1720, 2012.

[48] A. Tallaire, T. Ouisse, A. Lantreibecq, R. Cours, M. Legros, H. Bensalah, J. Barjon, V. Mille, O. Brinza, and J. Achard, “Identification of Dislocations in Synthetic Chemically Vapor Deposited Diamond Single Crystals”, en, *Crystal Growth & Design*, vol. 16, no. 5, pp. 2741–2746, 2016.

[49] P.-N. Volpe, P. Muret, F. Omnes, J. Achard, F. Silva, O. Brinza, and A. Gicquel, “Defect analysis and excitons diffusion in undoped homoepitaxial diamond films after polishing and oxygen plasma etching”, *Diamond and Related Materials*, vol. 18, no. 10, pp. 1205–1210, 2009.

[50] A. Kubota, S. Nagae, and M. Touge, “Improvement of material removal rate of single-crystal diamond by polishing using H2O2 solution”, *Diamond and Related Materials*, vol. 70, pp. 39–45, 2016.

[51] H. Tokura, C.-F. Yang, and M. Yoshikawa, “Study on the polishing of chemically vapour deposited diamond film”, *Thin Solid Films*, Special Issue: Diamond Films and Related Materials, vol. 212, no. 1, pp. 49–55, 1992.

[52] M. Challier, S. Sonusen, A. Barfuss, D. Rohner, D. Riedel, J. Koelbl, M. Ganzhorn, P. Appel, P. Maletinsky, and E. Neu, “Advanced fabrication of single-crystal diamond membranes for quantum technologies”, en, *Micromachines*, vol. 9, no. 4, p. 148, 2018.

[53] M. Rabarot, J. Widiez, S. Saada, J.-P. Mazellier, C. Lecouvey, J.-C. Roussin, J. Dechamp, P. Bergonzo, F. Andrieu, O. Faynot, S. Deleonibus, L. Clavelier, and J. Roger, “Silicon-On-Diamond layer integration by wafer bonding technology”, en, *Diamond and Related Materials*, vol. 19, no. 7-9, pp. 796–805, 2010.

[54] V. Bharadwaj, O. Jedrkiewicz, J. P. Hadden, B. Sotillo, M. R. Vázquez, P. Dentella, T. T. Fernandez, A. Chiappini, A. N. Giakoumaki, T. Le Phu, M. Bollani, M. Ferrari, R. Ramponi, P. E. Barclay, and S. M. Eaton, “Femtosecond laser written photonic and microfluidic circuits in diamond”, *Journal of Physics: Photonics*, vol. 1, no. 2, p. 022 001, 2019.

[55] H. Jin, S. P. Turaga, S. K. Vanga, and A. A. Bettiol, “Single-mode light guiding in diamond waveguides directly written by a focused proton beam”, EN, *Optics Letters*, vol. 43, no. 11, pp. 2648–2651, 2018.

[56] N. S. Rajput and X. Luo, “Chapter 3 - FIB Micro-/Nano-fabrication”, in *Micromanufacturing Engineering and Technology (Second Edition)*, ser. Micro and Nano Technologies, Y. Qin, Ed., Boston: William Andrew Publishing, 2015, pp. 61–80.

[57] I. Bayn, B. Meyler, J. Salzman, and R. Kalish, “Triangular nanobeam photonic cavities in single-crystal diamond”, *New Journal of Physics*, vol. 13, no. 2, p. 025 018, 2011.

[58] T. Graziosi, S. Mi, M. Kiss, and N. Quack, “Single crystal diamond micro-disk resonators by focused ion beam milling”, en, *APL Photonics*, vol. 3, no. 12, p. 126 101, 2018.

[59] T. M. Babinec, J. T. Choy, K. J. M. Smith, M. Khan, and M. Lončar, “Design and focused ion beam fabrication of single crystal diamond nanobeam cavities”, en, *Journal of Vacuum Science & Technology B, Nanotechnology and Microelectronics: Materials, Processing, Measurement, and Phenomena*, vol. 29, no. 1, p. 010 601, 2011.

[60] M. Schaffer, B. Schaffer, and Q. Ramasse, “Sample preparation for atomic-resolution STEM at low voltages by FIB”, *Ultramicroscopy*, vol. 114, pp. 62–71, 2012.

[61] M. J. Burek, N. P. de Leon, B. J. Shields, B. J. M. Hausmann, Y. Chu, Q. Quan, A. S. Zibrov, H. Park, M. D. Lukin, and M. Lončar, “Free-Standing Mechanical and Photonic Nanostructures in Single-Crystal Diamond”, en, *Nano Letters*, vol. 12, no. 12, pp. 6084–6089, 2012.

[62] M. J. Burek, Y. Chu, M. S. Z. Liddy, P. Patel, J. Rochman, S. Meesala, W. Hong, Q. Quan, M. D. Lukin, and M. Lončar, “High quality-factor optical nanocavities in bulk single-crystal diamond”, en, *Nature Communications*, vol. 5, no. 1, 2014.

[63] H. A. Atikian, P. Latawiec, M. J. Burek, Y.-I. Sohn, S. Meesala, N. Gravel, A. B. Kouki, and M. Lončar, “Freestanding nanostructures via reactive ion beam angled etching”, en, *APL Photonics*, vol. 2, no. 5, p. 051 301, 2017.

[64] B. Khanaliloo, M. Mitchell, A. C. Hryciw, and P. E. Barclay, “High- Q / V monolithic diamond microdisks fabricated with quasi-isotropic etching”, en, *Nano Letters*, vol. 15, no. 8, pp. 5131–5136, 2015.

[65] K. A. Shaw, Z. L. Zhang, and N. C. MacDonald, “SCREAM I: A single mask, single-crystal silicon, reactive ion etching process for microelectromechanical structures”, *Sensors and Actuators A: Physical*, vol. 40, no. 1, pp. 63–70, 1994.

[66] M. Mitchell, B. Khanaliloo, D. P. Lake, T. Masuda, J. P. Hadden, and P. E. Barclay, “Single-crystal diamond low-dissipation cavity optomechanics”, en, *Optica*, vol. 3, no. 9, p. 963, 2016.

[67] M. Mitchell, D. P. Lake, and P. E. Barclay, “Realizing Q > 300 000 in diamond microdisks for optomechanics via etch optimization”, en, *APL Photonics*, vol. 4, no. 1, p. 016 101, 2019.

[68] S. Mouradian, N. H. Wan, T. Schröder, and D. Englund, “Rectangular photonic crystal nanobeam cavities in bulk diamond”, en, *Applied Physics Letters*, vol. 111, no. 2, p. 021 103, 2017.

[69] N. H. Wan, S. Mouradian, and D. Englund, “Two-dimensional photonic crystal slab nanocavities on bulk single-crystal diamond”, en, *Applied Physics Letters*, vol. 112, no. 14, p. 141 102, 2018.

[70] S. Prawer and I. Aharonovich, Eds., *Quantum Information Processing with Diamond: Principles and Applications.* Amsterdam ; New York: Elsevier/WP, Woodhead Publishing is an imprint of Elsevier, 2014, OCLC: ocn859583047.

[71] C. F. Wang, R. Hanson, D. D. Awschalom, E. L. Hu, T. Feygelson, J. Yang, and J. E. Butler, “Fabrication and characterization of two-dimensional photonic crystal microcavities in nanocrystalline diamond”, en, *Applied Physics Letters*, vol. 91, no. 20, p. 201 112, 2007.

[72] C. F. Wang, Y.-S. Choi, J. C. Lee, E. L. Hu, J. Yang, and J. E. Butler, “Observation of whispering gallery modes in nanocrystalline diamond microdisks”, en, *Applied Physics Letters*, vol. 90, no. 8, p. 081 110, 2007.

[73] P. Rath, S. Khasminskaya, C. Nebel, C. Wild, and W. H. Pernice, “Grating-assisted coupling to nanophotonic circuits in microcrystalline diamond thin films”, en, *Beilstein Journal of Nanotechnology*, vol. 4, pp. 300–305, 2013.

[74] P. Rath, S. Khasminskaya, C. Nebel, C. Wild, and W. H. P. Pernice, “Diamond-integrated optomechanical circuits”, en, *Nature Communications*, vol. 4, p. 1690, 2013.

[75] P. Rath, N. Gruhler, S. Khasminskaya, C. Nebel, C. Wild, and W. H. P. Pernice, “Waferscale nanophotonic circuits made from diamond-on-insulator substrates”, en, *Optics Express*, vol. 21, no. 9, p. 11 031, 2013.

[76] J. Riedrich-Möller, L. Kipfstuhl, C. Hepp, E. Neu, C. Pauly, F. Mücklich, A. Baur, M. Wandt, S. Wolff, M. Fischer, S. Gsell, M. Schreck, and C. Becher, “One- and two-dimensional photonic crystal microcavities in single crystal diamond”, en, *Nature Nanotechnology*, vol. 7, no. 1, pp. 69–74, 2012.

[77] *Delaware Diamond Knives*, http://www.ddk.com/index.php.

[78] *Diamond Membranes & Foils | Applied Diamond, Inc.* en-US.

[79] A. Faraon, P. E. Barclay, C. Santori, K.-M. C. Fu, and R. G. Beausoleil, “Resonant enhancement of the zero-phonon emission from a colour centre in a diamond cavity”, en, *Nature Photonics*, vol. 5, no. 5, pp. 301–305, 2011.

[80] B. J. M. Hausmann, I. B. Bulu, P. B. Deotare, M. McCutcheon, V. Venkataraman, M. L. Markham, D. J. Twitchen, and M. Lončar, “Integrated High-Quality Factor Optical Resonators in Diamond”, en, *Nano Letters*, vol. 13, no. 5, pp. 1898–1902, 2013.

[81] B. J. M. Hausmann, B. J. Shields, Q. Quan, Y. Chu, N. P. de Leon, R. Evans, M. J. Burek, A. S. Zibrov, M. Markham, D. J. Twitchen, H. Park, M. D. Lukin, and M. Loncăr, “Coupling of NV Centers to Photonic Crystal Nanobeams in Diamond”, en, *Nano Letters*, vol. 13, no. 12, pp. 5791–5796, 2013.

[82] T. Jung, L. Kreiner, C. Pauly, F. Mücklich, A. M. Edmonds, M. Markham, and C. Becher, “Reproducible fabrication and characterization of diamond membranes for photonic crystal cavities: Reproducible fabrication and characterization of diamond membranes”, en, *physica status solidi (a)*, vol. 213, no. 12, pp. 3254–3264, 2016.

[83] L. Li, I. Bayn, M. Lu, C.-Y. Nam, T. Schröder, A. Stein, N. C. Harris, and D. Englund, “Nanofabrication on unconventional substrates using transferred hard masks”, en, *Scientific Reports*, vol. 5, no. 1, p. 7802, 2015.

[84] T. Schröder, M. E. Trusheim, M. Walsh, L. Li, J. Zheng, M. Schukraft, A. Sipahigil, R. E. Evans, D. D. Sukachev, C. T. Nguyen, J. L. Pacheco, R. M. Camacho, E. S. Bielejec, M. D. Lukin, and D. Englund, “Scalable focused ion beam creation of nearly lifetime-limited single quantum emitters in diamond nanostructures”, en, *Nature Communications*, vol. 8, no. 1, p. 15 376, 2017.

[85] F. Gao, J. Van Erps, Z. Huang, H. Thienpont, R. G. Beausoleil, and N. Vermeulen, "Directional Coupler Based on Single-Crystal Diamond Waveguides", *IEEE Journal of Selected Topics in Quantum Electronics*, vol. 24, no. 6, pp. 1–9, 2018.

[86] F. Gao, Z. Huang, B. Feigel, J. Van Erps, H. Thienpont, R. G. Beausoleil, and N. Vermeulen, "Low-Loss Millimeter-Length Waveguides and Grating Couplers in Single-Crystal Diamond", *Journal of Lightwave Technology*, vol. 34, no. 23, pp. 5576–5582, 2016.

[87] P. Hill, E. Gu, M. D. Dawson, and M. J. Strain, "Thin film diamond membranes bonded on-demand with SOI ring resonators", en, *Diamond and Related Materials*, vol. 88, pp. 215–221, 2018.

[88] P. Appel, E. Neu, M. Ganzhorn, A. Barfuss, M. Batzer, M. Gratz, A. Tschöpe, and P. Maletinsky, "Fabrication of all diamond scanning probes for nanoscale magnetometry", en, *Review of Scientific Instruments*, vol. 87, no. 6, p. 063 703, 2016.

[89] S. Ali Momenzadeh, F. F. de Oliveira, P. Neumann, D. D. Bhaktavatsala Rao, A. Denisenko, M. Amjadi, Z. Chu, S. Yang, N. B. Manson, M. W. Doherty, and J. Wrachtrup, "Thin Circular Diamond Membrane with Embedded Nitrogen-Vacancy Centers for Hybrid Spin-Mechanical Quantum Systems", *Physical Review Applied*, vol. 6, no. 2, p. 024 026, 2016.

[90] M. Pomorski, B. Caylar, and P. Bergonzo, "Super-thin single crystal diamond membrane radiation detectors", *Applied Physics Letters*, vol. 103, no. 11, p. 112 106, 2013.

[91] J. S. Hodges, L. Li, M. Lu, E. H. Chen, M. E. Trusheim, S. Allegri, X. Yao, O. Gaathon, H. Bakhru, and D. Englund, "Long-lived NV-spin coherence in high-purity diamond membranes", en, *New Journal of Physics*, vol. 14, no. 9, p. 093 004, 2012.

[92] M. Bruel, B. Aspar, and A.-J. Auberton-Hervé, "Smart-Cut: A New Silicon On Insulator Material Technology Based on Hydrogen Implantation and Wafer Bonding ^{*1}", en, *Japanese Journal of Applied Physics*, vol. 36, no. Part 1, No. 3B, pp. 1636–1641, 1997.

[93] N. R. Parikh, J. D. Hunn, E. McGucken, M. L. Swanson, C. W. White, R. A. Rudder, D. P. Malta, J. B. Posthill, and R. J. Markunas, "Single-crystal diamond plate liftoff achieved by ion implantation and subsequent annealing", en, *Applied Physics Letters*, vol. 61, no. 26, p. 3124, 1992.

[94] P. Olivero, S. Rubanov, P. Reichart, B. C. Gibson, S. T. Huntington, J. Rabeau, A. D. Greentree, J. Salzman, D. Moore, D. N. Jamieson, *et al.*, "Ion-Beam-Assisted Lift-Off Technique for Three-Dimensional Micromachining of Freestanding Single-Crystal Diamond", *Advanced Materials*, vol. 17, no. 20, pp. 2427–2430, 2005.

[95] B. A. Fairchild, P. Olivero, S. Rubanov, A. D. Greentree, F. Waldermann, R. A. Taylor, I. Walmsley, J. M. Smith, S. Huntington, B. C. Gibson, D. N. Jamieson, and S. Prawer, "Fabrication of Ultrathin Single-Crystal Diamond Membranes", en, *Advanced Materials*, vol. 20, no. 24, pp. 4793–4798, 2008.

[96] C. F. Wang, E. L. Hu, J. Yang, and J. E. Butler, "Fabrication of suspended single crystal diamond devices by electrochemical etch", en, *Journal of Vacuum Science & Technology B: Microelectronics and Nanometer Structures*, vol. 25, no. 3, p. 730, 2007.

[97] M. P. Hiscocks, K. Ganesan, B. C. Gibson, S. T. Huntington, F. Ladouceur, and S. Prawer, "Diamond waveguides fabricated by reactive ion etching", en, *Optics Express*, vol. 16, no. 24, p. 19 512, 2008.

[98] A. P. Magyar, J. C. Lee, A. M. Limarga, I. Aharonovich, F. Rol, D. R. Clarke, M. Huang, and E. L. Hu, "Fabrication of thin, luminescent, single-crystal diamond membranes", en, *Applied Physics Letters*, vol. 99, no. 8, p. 081 913, 2011.

[99] A. H. Piracha, K. Ganesan, D. W. M. Lau, A. Stacey, L. P. McGuinness, S. Tomljenovic-Hanic, and S. Prawer, "Scalable fabrication of high-quality, ultra-thin single crystal diamond membrane windows", en, *Nanoscale*, vol. 8, no. 12, pp. 6860–6865, 2016.

[100] A. H. Piracha, P. Rath, K. Ganesan, S. Kühn, W. H. P. Pernice, and S. Prawer, "Scalable Fabrication of Integrated Nanophotonic Circuits on Arrays of Thin Single Crystal Diamond Membrane Windows", en, *Nano Letters*, vol. 16, no. 5, pp. 3341–3347, 2016.

[101] V. Bormashov, S. Terentiev, S. Buga, S. Tarelkin, A. Volkov, D. Teteruk, N. Kornilov, M. Kuznetsov, and V. Blank, "Thin large area vertical Schottky barrier diamond diodes with low on-resistance made by ion-beam assisted lift-off technique", en, *Diamond and Related Materials*, vol. 75, pp. 78–84, 2017.

[102] S. Tarelkin, V. Bormashov, S. Buga, A. Volkov, D. Teteruk, N. Kornilov, M. Kuznetsov, S. Terentiev, A. Golovanov, and V. Blank, "Power diamond vertical Schottky barrier diode with 10 A forward current: Power diamond vertical Schottky barrier diode", en, *physica status solidi (a)*, vol. 212, no. 11, pp. 2621–2627, 2015.

[103] L. Li, E. H. Chen, J. Zheng, S. L. Mouradian, F. Dolde, T. Schröder, S. Karaveli, M. L. Markham, D. J. Twitchen, and D. Englund, "Efficient Photon Collection from a Nitrogen Vacancy Center in a Circular Bullseye Grating", en, *Nano Letters*, vol. 15, no. 3, pp. 1493–1497, 2015.

[104] S. A. Momenzadeh, R. J. Stöhr, F. F. de Oliveira, A. Brunner, A. Denisenko, S. Yang, F. Reinhard, and J. Wrachtrup, "Nanoengineered Diamond Waveguide as a Robust Bright Platform for Nanomagnetometry Using Shallow Nitrogen Vacancy Centers", en, *Nano Letters*, vol. 15, no. 1, pp. 165–169, 2015.

[105] O. Gaathon, J. Hodges, E. Chen, L. Li, S. Bakhru, H. Bakhru, D. Englund, and R. Osgood, "Planar fabrication of arrays of ion-exfoliated single-crystal-diamond membranes with nitrogen-vacancy color centers", en, *Optical Materials*, vol. 35, no. 3, pp. 361–365, 2013.

[106] J. C. Lee, I. Aharonovich, A. P. Magyar, F. Rol, and E. L. Hu, "Coupling of silicon-vacancy centers to a single crystal diamond cavity", en, *Optics Express*, vol. 20, no. 8, p. 8891, 2012.

[107] B. Yang, J. Li, L. Guo, N. Huang, L. Liu, Z. Zhai, W. Long, and X. Jiang, “Fabrication of silicon-vacancy color centers in diamond films: tetramethylsilane as a new dopant source”, en, *CrystEngComm*, vol. 20, no. 8, pp. 1158–1167, 2018.

[108] J. C. Angus and C. C. Hayman, “Low-Pressure, Metastable Growth of Diamond and “Diamondlike” Phases”, *Science*, vol. 241, no. 4868, pp. 913–921, 1988.

[109] G. Braunstein, A. Talmi, R. Kalish, T. Bernstein, and R. Beserman, “Radiation damage and annealing in Sb implanted diamond”, en, *Radiation Effects*, vol. 48, no. 1-4, pp. 139–143, 1980.

[110] R. Locher, D. Behr, H. Güllich, N. Herres, P. Koidl, R. Samlenski, and R. Brenn, “Lift-off technique of homoepitaxial CVD diamond films by deep implantation and selective etching”, en, *Diamond and Related Materials*, vol. 6, no. 5-7, pp. 654–657, 1997.

[111] R. Samlenski, H. Gärtner, R. Locher, P. Koidl, and R. Brenn, “Liftoff-technique of single-crystal diamond plates: study of the lattice damage of the implanted substrates and the crystalline quality of the homoepitaxial films by ion channelling”, en, *Diamond and Related Materials*, vol. 6, no. 1, pp. 149–152, 1997.

[112] A. A. Gippius, R. A. Khmelnitsky, V. A. Dravin, and A. V. Khomich, “Defect-induced graphitisation in diamond implanted with light ions”, *Physica B: Condensed Matter*, vol. 308, pp. 573–576, 2001.

[113] A. Gippius, R. Khmelnitsky, V. Dravin, and A. Khomich, “Diamond–graphite transformation induced by light ions implantation”, en, *Diamond and Related Materials*, vol. 12, no. 3-7, pp. 538–541, 2003.

[114] A. V. Khomich, R. A. Khmelnitskiy, V. A. Dravin, A. A. Gippius, E. V. Zavedeev, and I. I. Vlasov, “Radiation damage in diamonds subjected to helium implantation”, en, *Physics of the Solid State*, vol. 49, no. 9, pp. 1661–1665, 2007.

[115] A. Silverman, J. Adler, and R. Kalish, “Diamond membrane surface after ion-implantation-induced graphitization for graphite removal: Molecular dynamics simulation”, *Physical Review B*, vol. 83, no. 22, p. 224 206, 2011.

[116] J. Suk, H. Kim, W. C. Lim, J. Yune, S. Moon, J. A. Eliades, J. Kim, J. Lee, and J. Song, “Fabrication of thin diamond membranes by using hot implantation and ion-cut methods”, *Applied Physics Letters*, vol. 110, no. 10, p. 101 903, 2017.

[117] F. Bosia, N. Argiolas, M. Bazzan, P. Olivero, F. Picollo, A. Sordini, M. Vannoni, and E. Vittone, “Modification of the structure of diamond with MeV ion implantation”, en, *Diamond and Related Materials*, vol. 20, no. 5-6, pp. 774–778, 2011.

[118] F. Bosia, S. Calusi, L. Giuntini, S. Lagomarsino, A. Lo Giudice, M. Massi, P. Olivero, F. Picollo, S. Sciortino, A. Sordini, M. Vannoni, and E. Vittone, “Finite element analysis of ion-implanted diamond surface swelling”, en, *Nuclear Instruments and Methods in Physics Research Section B: Beam Interactions with Materials and Atoms*, vol. 268, no. 19, pp. 2991–2995, 2010.

[119] F Bosia, N Argiolas, M Bazzan, B. A. Fairchild, A. D. Greentree, D. W. M. Lau, P Olivero, F Picollo, S Rubanov, and S Prawer, "Direct measurement and modelling of internal strains in ion-implanted diamond", *Journal of Physics: Condensed Matter*, vol. 25, no. 38, p. 385 403, 2013.

[120] F. Picollo, A. Battiato, L. Boarino, S. Ditalia Tchernij, E. Enrico, J. Forneris, A. Gilardino, M. Jakšić, F. Sardi, N. Skukan, A. Tengattini, P. Olivero, A. Re, and E. Vittone, "Fabrication of monolithic microfluidic channels in diamond with ion beam lithography", *Nuclear Instruments and Methods in Physics Research, Section B: Beam Interactions with Materials and Atoms*, vol. 404, pp. 193–197, 2017.

[121] G. García, I. Preda, M. Díaz-Híjar, V. Tormo-Márquez, O. Peña-Rodríguez, J. Olivares, F. Bosia, N. Pugno, F. Picollo, L. Giuntini, S. A., P. Olivero, L. López-Mir, and C. Ocal, "Micro and nano-patterning of single-crystal diamond by swift heavy ion irradiation", *Diamond and Related Materials*, vol. 69, pp. 1–7, 2016.

[122] G. Tomagra, P. Aprà, A. Battiato, C. Collà Ruvolo, A. Pasquarelli, A. Marcantoni, E. Carbone, V. Carabelli, P. Olivero, and F. Picollo, "Micro graphite-patterned diamond sensors: Towards the simultaneous in vitro detection of molecular release and action potentials generation from excitable cells", *Carbon*, vol. 152, pp. 424–433, 2019.

[123] J. O. Orwa, K. W. Nugent, D. N. Jamieson, and S. Prawer, "Raman investigation of damage caused by deep ion implantation in diamond", *Physical Review B*, vol. 62, no. 9, p. 5461, 2000.

[124] P. Olivero, S. Rubanov, P. Reichart, B. Gibson, S. Huntington, J. Rabeau, A. D. Greentree, J. Salzman, D. Moore, D. Jamieson, and S. Prawer, "Characterization of three-dimensional microstructures in single-crystal diamond", en, *Diamond and Related Materials*, vol. 15, no. 10, pp. 1614–1621, 2006.

[125] B. R. Patton, P. R. Dolan, F. Grazioso, M. B. Wincott, J. M. Smith, M. L. Markham, D. J. Twitchen, Y. Zhang, E. Gu, M. D. Dawson, B. A. Fairchild, A. D. Greentree, and S. Prawer, "Optical properties of single crystal diamond microfilms fabricated by ion implantation and lift-off processing", en, *Diamond and Related Materials*, vol. 21, pp. 16–23, 2012.

[126] D. Hickey, K. Jones, and R. Elliman, "Amorphization and graphitization of single-crystal diamond — A transmission electron microscopy study", en, *Diamond and Related Materials*, vol. 18, no. 11, pp. 1353–1359, 2009.

[127] S. Rubanov, B. A. Fairchild, A. Suvorova, P. Olivero, and S. Prawer, "Structural transformation of implanted diamond layers during high temperature annealing", *Nuclear Instruments and Methods in Physics Research Section B: Beam Interactions with Materials and Atoms*, Proceedings of the 19th International Conference on Ion Beam Modification of Materials (IBMM 2014), vol. 365, pp. 50–54, 2015.

[128] H. Umezawa, Y. Kato, H. Watanabe, A. M. M. Omer, H. Yamaguchi, and S.-i. Shikata, “Characterization of crystallographic defects in homoepitaxial diamond films by synchrotron X-ray topography and cathodoluminescence”, *Diamond and Related Materials*, vol. 20, no. 4, pp. 523–526, 2011.

[129] Z. Ma, B. Liu, H. Naramoto, Y. Aoki, S. Yamamoto, H. Takeshita, and P. Goppelt-Langer, “Non-destructive characterization of ion-implanted diamond”, en, *Vacuum*, vol. 55, no. 3-4, pp. 207–217, 1999.

[130] M. A. Draganski, E. Finkman, B. C. Gibson, B. A. Fairchild, K. Ganesan, N. Nabatova-Gabain, S. Tomljenovic-Hanic, A. D. Greentree, and S. Prawer, “Tailoring the optical constants of diamond by ion implantation”, EN, *Optical Materials Express*, vol. 2, no. 5, pp. 644–649, 2012.

[131] M. Marchywka, “Electrochemical Patterning of Amorphous Carbon on Diamond”, en, *Journal of The Electrochemical Society*, vol. 140, no. 2, p. L19, 1993.

[132] M. J. Marchywka, “Electrochemical process and product therefrom”, pat. US5269890A.

[133] R. W. Coughlin and M. Farooque, “Hydrogen production from coal, water and electrons”, en, *Nature*, vol. 279, no. 5711, pp. 301–303, 1979.

[134] G. Roelkens, J. Van Campenhout, J. Brouckaert, D. Van Thourhout, R. Baets, P. R. Romeo, P. Regreny, A. Kazmierczak, C. Seassal, X. Letartre, *et al.*, “III-V/Si photonics by die-to-wafer bonding”, *Materials Today*, vol. 10, no. 7, pp. 36–43, 2007.

[135] X. Luo, Y. Cao, J. Song, X. Hu, Y. Cheng, C. Li, C. Liu, T.-Y. Liow, M. Yu, H. Wang, Q. J. Wang, and P. G.-Q. Lo, “High-Throughput Multiple Dies-to-Wafer Bonding Technology and III/V-on-Si Hybrid Lasers for Heterogeneous Integration of Optoelectronic Integrated Circuits”, *Frontiers in Materials*, vol. 2, 2015.

[136] E. Russell and I. Thomson, “Embedded diamond heat sinks for avalanche diodes”, *Proceedings of the IEEE*, vol. 60, no. 8, pp. 1014–1015, 1972.

[137] A. Katz, C. Lee, and K. Tai, “Advanced metallization schemes for bonding of InP-based laser devices to CVD-diamond heatsinks”, en, *Materials Chemistry and Physics*, vol. 37, no. 4, pp. 303–328, 1994.

[138] S. Weiss, E. Zakel, and H. Reichl, “Mounting of high power laser diodes on diamond heatsinks”, *IEEE Transactions on Components, Packaging, and Manufacturing Technology: Part A*, vol. 19, no. 1, pp. 46–53, 1996.

[139] X. Xie, Q. Zhou, K. Li, Y. Shen, Q. Li, Z. Yang, A. Beling, and J. C. Campbell, “Improved power conversion efficiency in high-performance photodiodes by flip-chip bonding on diamond”, en, *Optica*, vol. 1, no. 6, p. 429, 2014.

[140] A. Ahnood, M. C. Escudie, R. Cicione, C. D. Abeyrathne, K. Ganesan, K. E. Fox, D. J. Garrett, A. Stacey, N. V. Apollo, S. G. Lichter, C. D. L. Thomas, N. Tran, H. Meffin, and S. Prawer, “Ultrananocrystalline diamond-CMOS device integration route for high acuity retinal prostheses”, en, *Biomedical Microdevices*, vol. 17, no. 3, p. 50, 2015.

[141] S. Stanković, R. Jones, J. Heck, M. Sysak, D. Van Thourhout, and G. Roelkens, "Die-to-die adhesive bonding procedure for evanescently-coupled photonic devices", *Electrochemical and Solid-State Letters*, vol. 14, no. 8, H326–H329, 2011.

[142] V Lebedev, T Lisec, T Yoshikawa, M Reusch, D Iankov, and C Giese, "Nanodiamond resonators fabricated on 8"si substrates using adhesive wafer bonding", en, *J. Micromech. Microeng.*, p. 9, 2017.

[143] Y. Tao, J. M. Boss, B. A. Moores, and C. L. Degen, "Single-crystal diamond nanomechanical resonators with quality factors exceeding one million", en, *Nature Communications*, vol. 5, no. 1, p. 3638, 2014.

[144] B. Bayram, O. Akar, and T. Akin, "Plasma-activated direct bonding of diamond-on-insulator wafers to thermal oxide grown silicon wafers", en, *Diamond and Related Materials*, vol. 19, no. 11, pp. 1431–1435, 2010.

[145] A. Plössl and G. Kräuter, "Wafer direct bonding: tailoring adhesion between brittle materials", *Materials Science and Engineering: R: Reports*, vol. 25, no. 1, pp. 1–88, 1999.

[146] D. Pasquariello and K. Hjort, "Plasma-assisted InP-to-Si low temperature wafer bonding", *IEEE Journal of Selected Topics in Quantum Electronics*, vol. 8, no. 1, pp. 118–131, Jan.-Feb./2002.

[147] D. Liang, A. W. Fang, H. Park, T. E. Reynolds, K. Warner, D. C. Oakley, and J. E. Bowers, "Low-Temperature, Strong SiO2-SiO2 Covalent Wafer Bonding for III–V Compound Semiconductors-to-Silicon Photonic Integrated Circuits", en, *Journal of Electronic Materials*, vol. 37, no. 10, pp. 1552–1559, 2008.

[148] V. Masteika, J. Kowal, N. S. J. Braithwaite, and T. Rogers, "A review of hydrophilic silicon wafer bonding", *ECS Journal of Solid State Science and Technology*, vol. 3, no. 4, Q42–Q54, 2014.

[149] F. Mu, Y. Wang, and T. Suga, "*(Invited)* Room Temperature Wafer Bonding of Wide Bandgap Semiconductors", en, *ECS Transactions*, vol. 86, no. 5, pp. 3–21, 2018.

[150] Q.-Y. Tong and U. Gösele, "Semiconductor wafer bonding: recent developments", en, *Materials Chemistry and Physics*, vol. 37, no. 2, pp. 101–127, 1994.

[151] D. Conrad, K. Scheerschmidt, and U. Gösele, "On the possibility of diamond wafer bonding in ultrahigh vacuum", en, *Applied Physics Letters*, vol. 77, no. 1, pp. 49–51, 2000.

[152] G. N. Yushin, S. D. Wolter, A. V. Kvit, R. Collazo, B. R. Stoner, J. T. Prater, and Z. Sitar, "Study of fusion bonding of diamond to silicon for silicon-on-diamond technology", en, *Applied Physics Letters*, vol. 81, no. 17, pp. 3275–3277, 2002.

[153] M. I. Landstrass and D. M. Fleetwood, "Total dose radiation hardness of diamond-based silicon-on-insulator structures", en, *Applied Physics Letters*, vol. 56, no. 23, pp. 2316–2318, 1990.

[154] G. Yushin, A. Aleksov, S. Wolter, F. Okuzumi, J. Prater, and Z. Sitar, “Wafer bonding of highly oriented diamond to silicon”, en, *Diamond and Related Materials*, vol. 13, no. 10, pp. 1816–1821, 2004.

[155] J. Liang, S. Masuya, M. Kasu, and N. Shigekawa, “Realization of direct bonding of single crystal diamond and Si substrates”, en, *Applied Physics Letters*, vol. 110, no. 11, p. 111 603, 2017.

[156] Y. Koga and K. Kurita, “SOI wafer fabricated with a diamond BOX layer using surface activated bonding at room temperature”, *Japanese Journal of Applied Physics*, vol. 58, no. 1, p. 016 505, 2019.

[157] J. Liang, S. Masuya, S. Kim, T. Oishi, M. Kasu, and N. Shigekawa, “Stability of diamond/Si bonding interface during device fabrication process”, *Applied Physics Express*, vol. 12, no. 1, p. 016 501, 2019.

[158] M. Nagata, R. Shirahama, S. Duangchan, and A. Baba, “Fabrication of silicon-on-diamond substrate with an ultrathin SiO_2 bonding layer”, *Japanese Journal of Applied Physics*, vol. 57, no. 6S1, 06HJ08, 2018.

[159] T. Sugino, T. Itagaki, and J. Shirafuji, “P-diamond/n-GaAs junctions formed by direct bonding”, *Electronics Letters*, vol. 32, no. 1, pp. 71–73, 1996.

[160] K. Chabak, J. Gillespie, V. Miller, A. Crespo, J. Roussos, M. Trejo, D. Walker, G. Via, G. Jessen, J. Wasserbauer, F. Faili, D. Babic, D. Francis, and F. Ejeckam, “Full-Wafer Characterization of AlGaN/GaN HEMTs on Free-Standing CVD Diamond Substrates”, *IEEE Electron Device Letters*, vol. 31, no. 2, pp. 99–101, 2010.

[161] H. G. Stenhouse, S. J. Beecher, and J. I. Mackenzie, “Direct bonding CVD-grown diamond to ZnSe and sapphire”, en, in *Laser Congress 2017 (ASSL, LAC)*, Nagoya, Aichi: OSA, 2017, AW3A.6.

[162] B. J. M. Hausmann, I. Bulu, V. Venkataraman, P. Deotare, and M. Lončar, “Diamond nonlinear photonics”, en, *Nature Photonics*, vol. 8, no. 5, pp. 369–374, 2014.

[163] L. Li, X. Chen, W. Zhang, and K. Peng, “Characterization and formation mechanism of pits on diamond {100} face etched by molten potassium nitrite”, en, *International Journal of Refractory Metals and Hard Materials*, vol. 71, pp. 129–134, 2018.

[164] V. M. Sonin, A. I. Chepurov, E. I. Zhimulev, A. A. Chepurov, and N. V. Sobolev, “Surface graphitization of diamond in K2CO3 melt at high pressure”, en, *Doklady Earth Sciences*, vol. 451, no. 2, pp. 858–860, 2013.

[165] M. Jamali, I. Gerhardt, M. Rezai, K. Frenner, H. Fedder, and J. Wrachtrup, “Microscopic diamond solid-immersion-lenses fabricated around single defect centers by focused ion beam milling”, en, *Review of Scientific Instruments*, vol. 85, no. 12, p. 123 703, 2014.

[166] A. A. Martin, S. Randolph, A. Botman, M. Toth, and I. Aharonovich, “Maskless milling of diamond by a focused oxygen ion beam”, en, *Scientific Reports*, vol. 5, p. 8958, 2015.

[167] J. Bishop, M. Fronzi, C. Elbadawi, V. Nikam, J. Pritchard, J. E. Fröch, N. M. H. Duong, M. J. Ford, I. Aharonovich, C. J. Lobo, and M. Toth, “Deterministic Nanopatterning of Diamond Using Electron Beams”, en, *ACS Nano*, vol. 12, no. 3, pp. 2873–2882, 2018.

[168] M. Polikarpov, V. Polikarpov, I. Snigireva, and A. Snigirev, “Diamond X-ray Refractive Lenses with High Acceptance”, en, *Physics Procedia*, vol. 84, pp. 213–220, 2016.

[169] T. Yatsui, W. Nomura, M. Naruse, and M. Ohtsu, “Realization of an atomically flat surface of diamond using dressed photon–phonon etching”, en, *Journal of Physics D: Applied Physics*, vol. 45, no. 47, p. 475 302, 2012.

[170] D. I. Shahin, T. J. Anderson, T. I. Feygelson, B. B. Pate, V. D. Wheeler, J. D. Greenlee, J. K. Hite, M. J. Tadjer, A. Christou, and K. D. Hobart, “Thermal etching of nanocrystalline diamond films”, en, *Diamond and Related Materials*, vol. 59, pp. 116–121, 2015.

[171] Z. Shpilman, I. Gouzman, E. Grossman, L. Shen, T. K. Minton, J. T. Paci, G. C. Schatz, R. Akhvlediani, and A. Hoffman, “Oxidation and Etching of CVD Diamond by Thermal and Hyperthermal Atomic Oxygen”, *The Journal of Physical Chemistry C*, vol. 114, no. 44, pp. 18 996–19 003, 2010.

[172] V. Ralchenko, T. Kononenko, S. Pimenov, N. Chernenko, E. Loubnin, V. Armeyev, and A. Zlobin, “Catalytic interaction of Fe, Ni and Pt with diamond films: patterning applications”, en, *Diamond and Related Materials*, vol. 2, no. 5-7, pp. 904–909, 1993.

[173] H.-A. Mehedi, C. Hebert, S. Ruffinatto, D. Eon, F. Omnes, and E. Gheeraert, “Formation of oriented nanostructures in diamond using metallic nanoparticles”, en, *Nanotechnology*, vol. 23, no. 45, p. 455 302, 2012.

[174] M. Nagai, K. Nakanishi, H. Takahashi, H. Kato, T. Makino, S. Yamasaki, T. Matsumoto, T. Inokuma, and N. Tokuda, “Anisotropic diamond etching through thermochemical reaction between Ni and diamond in high-temperature water vapour”, en, *Scientific Reports*, vol. 8, no. 1, p. 6687, 2018.

[175] A. Joshi and R. Nimmagadda, “Erosion of diamond films and graphite in oxygen plasma”, *Journal of materials research*, vol. 6, no. 07, pp. 1484–1490, 1991.

[176] T. Izak, A. Kromka, O. Babchenko, M. Ledinsky, K. Hruska, and E. Verveniotis, “Comparative study on dry etching of polycrystalline diamond thin films”, en, *Vacuum*, vol. 86, no. 6, pp. 799–802, 2012.

[177] T. Yamada, H. Yoshikawa, H. Uetsuka, S. Kumaragurubaran, N. Tokuda, and S.-i. Shikata, “Cycle of two-step etching process using ICP for diamond MEMS applications”, *Diamond and Related Materials*, Proceedings of Diamond 2006, the 17th European Conference on Diamond, Diamond-Like Materials, Carbon Nanotubes, Nitrides and Silicon Carbide, vol. 16, no. 4, pp. 996–999, 2007.

[178] Y. Ando, Y. Nishibayashi, K. Kobashi, T. Hirao, and K. Oura, “Smooth and high-rate reactive ion etching of diamond”, en, *Diamond and Related Materials*, vol. 11, no. 3-6, pp. 824–827, 2002.

[179] C. Lee, E. Gu, M. Dawson, I. Friel, and G. Scarsbrook, “Etching and micro-optics fabrication in diamond using chlorine-based inductively-coupled plasma”, en, *Diamond and Related Materials*, vol. 17, no. 7-10, pp. 1292–1296, 2008.

[180] V. Yurov, E. Bushuev, A. Bolshakov, E. Ashkinazi, I. Antonova, E. Zavedeev, A. Khomich, V. Voronov, and V. Ralchenko, “Etching Kinetics of (100) Single Crystal Diamond Surfaces in a Hydrogen Microwave Plasma, Studied with In Situ Low-Coherence Interferometry”, en, *physica status solidi (a)*, vol. 214, no. 11, p. 1 700 177, 2017.

[181] N. Tsubouchi, Y. Mokuno, and S. Shikata, “Characterizations of etch pits formed on single crystal diamond surface using oxygen/hydrogen plasma surface treatment”, *Diamond and Related Materials*, 9th International Conference on New Diamond and Nano Carbons – NDNC 2015, vol. 63, pp. 43–46, 2016.

[182] P. W. Leech, G. K. Reeves, A. S. Holland, and F. Shanks, “Ion beam etching of CVD diamond film in Ar, Ar/O2 and Ar/CF4 gas mixtures”, *Diamond and Related Materials*, 12th European Conference on Diamond, Diamond- Like Materials, Carbon Nanotubes, Nitrides & Silicon Carbide, vol. 11, no. 3, pp. 833–836, 2002.

[183] P. Pal and K. Sato, *Silicon Wet Bulk Micromachining for MEMS*, en. CRC Press, 2017.

[184] A. V. N. Rao, V. Swarnalatha, and P. Pal, “Etching characteristics of Si{110} in 20 wt% KOH with addition of hydroxylamine for the fabrication of bulk micromachined MEMS”, en, *Micro and Nano Systems Letters*, vol. 5, no. 1, p. 23, 2017.

[185] J. Chai, G. Walker, L. Wang, D. Massoubre, S. H. Tan, K. Chaik, L. Hold, and A. Iacopi, “Silicon etching using only Oxygen at high temperature: An alternative approach to Si micro-machining on 150 mm Si wafers”, *Scientific Reports*, vol. 5, p. 17 811, 2015.

[186] L. Xie, T. X. Zhou, R. J. Stöhr, and A. Yacoby, “Crystallographic orientation dependent reactive ion etching in single crystal diamond”, en, *Advanced Materials*, vol. 30, no. 11, p. 1 705 501, 2018.

[187] O. Auciello, S. Pacheco, A. Sumant, C. Gudeman, S. Sampath, A. Datta, R. Carpick, V. Adiga, P. Zurcher, Z. Ma, H.-c. Yuan, J. Carlisle, B. Kabius, J. Hiller, and S. Srinivasan, “Are Diamonds a MEMS’ Best Friend?”, *IEEE Microwave Magazine*, vol. 8, no. 6, pp. 61–75, 2007.

[188] M. Possas-Abreu, F. Ghassemi, L. Rousseau, E. Scorsone, E. Descours, and G. Lissorgues, “Development of Diamond and Silicon MEMS Sensor Arrays with Integrated Readout for Vapor Detection”, en, *Sensors*, vol. 17, no. 6, p. 1163, 2017.

[189] E Kohn, P Gluche, and M Adamschik, “Diamond MEMS — a new emerging technology”, en, *Diamond and Related Materials*, vol. 8, no. 2-5, pp. 934–940, 1999.

[190] H. Björkman, P. Rangsten, and K. Hjort, “Diamond microstructures for optical micro electromechanical systems”, en, *Sensors and Actuators A: Physical*, vol. 78, no. 1, pp. 41–47, 1999.

[191] M. Liao, S. Hishita, E. Watanabe, S. Koizumi, and Y. Koide, “Suspended Single-Crystal Diamond Nanowires for High-Performance Nanoelectromechanical Switches”, *Advanced Materials*, vol. 22, no. 47, pp. 5393–5397, 2010.

[192] M. Liao, L. Sang, T. Teraji, S. Koizumi, and Y. Koide, “Ultrahigh Performance On-Chip Single Crystal Diamond NEMS/MEMS with Electrically Tailored Self-Sensing Enhancing Actuation”, en, *Advanced Materials Technologies*, vol. 4, no. 2, p. 1 800 325, 2019.

[193] J. J. Bernstein, M. G. Bancu, E. H. Cook, M. V. Chaparala, W. A. Teynor, and M. S. Weinberg, “A MEMS diamond hemispherical resonator”, *Journal of Micromechanics and Microengineering*, vol. 23, no. 12, p. 125 007, 2013.

[194] D. Saito, C. Yang, A. Heidari, H. Najar, L. Lin, and D. A. Horsley, “Microcrystalline diamond cylindrical resonators with quality-factor up to 0.5 million”, *Applied Physics Letters*, vol. 108, no. 5, p. 051 904, 2016.

[195] T. L. Naing, T. O. Rocheleau, Z. Ren, S. Li, and C. T. Nguyen, “High- Q UHF Spoke-Supported Ring Resonators”, *Journal of Microelectromechanical Systems*, vol. 25, no. 1, pp. 11–29, 2016.

[196] H. Wu, L. Sang, Y. Li, T. Teraji, T. Li, M. Imura, J. You, Y. Koide, M. Toda, and M. Liao, “Reducing intrinsic energy dissipation in diamond-on-diamond mechanical resonators toward one million quality factor”, en, *Physical Review Materials*, vol. 2, no. 9, p. 090 601, 2018.

[197] H. Rokhsari, T. J. Kippenberg, T. Carmon, and K. J. Vahala, “Radiation-pressure-driven micro-mechanical oscillator”, *Opt. Express*, vol. 13, no. 14, p. 5293, 2005.

[198] M. Aspelmeyer, T. J. Kippenberg, and F. Marquardt, “Cavity optomechanics”, en, *Reviews of Modern Physics*, vol. 86, no. 4, pp. 1391–1452, 2014.

[199] X. Luan, Y. Huang, Y. Li, J. F. McMillan, J. Zheng, S.-W. Huang, P.-C. Hsieh, T. Gu, D. Wang, A. Hati, D. A. Howe, G. Wen, M. Yu, G. Lo, D.-L. Kwong, and C. W. Wong, “An integrated low phase noise radiation-pressure-driven optomechanical oscillator chipset”, *Sci. Rep.*, vol. 4, p. 6842, 2014.

[200] C. Huang, J. Fan, R. Zhang, and L. Zhu, “Internal frequency mixing in a single optomechanical resonator”, *Appl. Phys. Lett.*, vol. 101, no. 23, p. 231 112, 2012.

[201] F. Liu and M. Hossein-Zadeh, “On the spectrum of radiation pressure driven optomechanical oscillator and its application in sensing”, *Optics Communications*, vol. 294, pp. 338–343, 2013.

[202] F. Liu, S. Alaie, Z. C. Leseman, and M. Hossein-Zadeh, “Sub-pg mass sensing and measurement with an optomechanical oscillator”, *Opt. Express*, vol. 21, no. 17, p. 19 555, 2013.

[203] K. E. Grutter, “Optical whispering-gallery mode resonators for applications in optical communication and frequency control”, PhD thesis, University of California, Berkeley, 2013.

[204] S. Tallur, S. Sridaran, and S. A. Bhave, “A monolithic radiation-pressure driven, low phase noise silicon nitride opto-mechanical oscillator”, *Opt. Express*, vol. 19, no. 24, p. 24 522, 2011.

[205] W. C. Jiang and Q. Lin, “Chip-scale cavity optomechanics in lithium niobate”, *ArXiv e-prints*, 2016.

[206] P. Rath, S. Ummethala, S. Diewald, G. Lewes-Malandrakis, D. Brink, N. Heidrich, C. Nebel, and W. H. P. Pernice, “Diamond electro-optomechanical resonators integrated in nanophotonic circuits”, *Applied Physics Letters*, vol. 105, no. 25, p. 251 102, 2014.

[207] M. J. Burek, J. D. Cohen, S. M. Meenehan, N. El-Sawah, C. Chia, T. Ruelle, S. Meesala, J. Rochman, H. A. Atikian, M. Markham, D. J. Twitchen, M. D. Lukin, O. Painter, and M. Lončar, “Diamond optomechanical crystals”, en, *Optica*, vol. 3, no. 12, p. 1404, 2016.

[208] B. Khanaliloo, H. Jayakumar, A. C. Hryciw, D. P. Lake, H. Kaviani, and P. E. Barclay, “Single-Crystal Diamond Nanobeam Waveguide Optomechanics”, *Physical Review X*, vol. 5, no. 4, p. 041 051, 2015.

[209] F. Nikolajeff and M. Karlsson, “Refractive and Diffractive Diamond Optics”, en, in *Optical Engineering of Diamond*, R. P. Mildren and J. R. Rabeau, Eds., Weinheim, Germany: Wiley-VCH Verlag GmbH & Co. KGaA, 2013, pp. 109–142.

[210] C. Holly, M. Traub, D. Hoffmann, C. Widmann, D. Brink, C. Nebel, T. Gotthardt, M. C. Sözbir, and C. Wenzel, “Monocrystalline CVD-diamond optics for high-power laser applications”, in *SPIE LASE*, F. Dorsch and S. Kaierle, Eds., San Francisco, California, United States, 2016, p. 974 104.

[211] J. Ge, B. Zhao, S. Powell, A. Fletcher, X. Wan, L. Chang, H. Jakeman, D. Koukis, D. B. Tanner, D. Ebbets, J. Weinberg, S. Lipscy, R. Nyquist, and J. Bally, “Silicon immersion gratings and their spectroscopic applications”, R. Navarro, C. R. Cunningham, and E. Prieto, Eds., 2012, 84502U.

[212] J. Lee, S. Ahn, H. Chang, J. Kim, Y. Park, and H. Jeon, “Polarization-dependent GaN surface grating reflector for short wavelength applications”, en, *Optics Express*, vol. 17, no. 25, p. 22 535, 2009.

[213] G Almuneau, M Condé, O Gauthier-Lafaye, V Bardinal, and C Fontaine, “High reflectivity monolithic sub-wavelength diffraction grating with GaAs/AlO $_x$ stack”, *Journal of Optics*, vol. 13, no. 1, p. 015 505, 2011.

[214] D. J. Mar, J. P. Marsh, C. P. Deen, H. Ling, H. Choo, and D. T. Jaffe, “Micromachined silicon grisms for infrared optics”, en, *Applied Optics*, vol. 48, no. 6, p. 1016, 2009.

[215] Q. Nie, Z. Wen, and J. Huang, “A high-performance scanning grating based on tilted (111) silicon wafer for near infrared micro spectrometer application”, en, *Microsystem Technologies*, vol. 21, no. 8, pp. 1749–1755, 2015.

[216] J. Reimers, A. Bauer, K. P. Thompson, and J. P. Rolland, “Freeform spectrometer enabling increased compactness”, *Light: Science & Applications*, vol. 6, no. 7, e17026, 2017.

[217] B. Mroziewicz, E. Kowalczyk, L. Dobrzanski, J. Ratajczak, and S. J. Lewandowski, “External cavity diode lasers with E-beam written silicon diffraction gratings”, en, *Optical and Quantum Electronics*, vol. 39, no. 7, pp. 585–595, 2007.

[218] W.-g. Lu, R. Xiao, J. Liu, L. Wang, H. Zhong, and Y. Wang, “Large-area rainbow holographic diffraction gratings on a curved surface using transferred photopolymer films”, en, *Optics Letters*, vol. 43, no. 4, p. 675, 2018.

[219] J. Chen, H. Huang, Y. Zhang, Y. Wang, F. Kong, Y. Wang, Y. Jin, P. Chen, J. Xu, and J. Shao, “Reducing electric-field-enhancement in metal-dielectric grating by designing grating with asymmetric ridge”, en, *Scientific Reports*, vol. 8, no. 1, p. 5228, 2018.

[220] P. Karvinen, S. Rutishauser, A. Mozzanica, D. Greiffenberg, P. N. Juranić, A. Menzel, A. Lutman, J. Krzywinski, D. M. Fritz, H. T. Lemke, M. Cammarata, and C. David, “Single-shot analysis of hard x-ray laser radiation using a noninvasive grating spectrometer”, en, *Optics Letters*, vol. 37, no. 24, p. 5073, 2012.

[221] M. Makita, P. Karvinen, D. Zhu, P. N. Juranic, J. Grünert, S. Cartier, J. H. Jungmann-Smith, H. T. Lemke, A. Mozzanica, S. Nelson, L. Patthey, M. Sikorski, S. Song, Y. Feng, and C. David, “High-resolution single-shot spectral monitoring of hard x-ray free-electron laser radiation”, en, *Optica*, vol. 2, no. 10, p. 912, 2015.

[222] E. Woerner, C. Wild, W. Mueller-Sebert, and P. Koidl, “CVD-diamond optical lenses”, en, *Diamond and Related Materials*, vol. 10, no. 3-7, pp. 557–560, 2001.

[223] H. Liu, S. Reilly, J. Herrnsdorf, E. Xie, V. G. Savitski, A. J. Kemp, E. Gu, and M. D. Dawson, “Large radius of curvature micro-lenses on single crystal diamond for application in monolithic diamond Raman lasers”, en, *Diamond and Related Materials*, vol. 65, pp. 37–41, 2016.

[224] E. Gu, H. W. Choi, C. Liu, C. Griffin, J. M. Girkin, I. M. Watson, M. D. Dawson, G. McConnell, and A. M. Gurney, “Reflection/transmission confocal microscopy characterization of single-crystal diamond microlens arrays”, en, *Applied Physics Letters*, vol. 84, no. 15, pp. 2754–2756, 2004.

[225] H. W. Choi, E. Gu, C. Liu, C. Griffin, J. M. Girkin, I. M. Watson, and M. D. Dawson, “Fabrication of natural diamond microlenses by plasma etching”, en, *Journal of Vacuum Science & Technology B: Microelectronics and Nanometer Structures*, vol. 23, no. 1, p. 130, 2005.

[226] T.-F. Zhu, J. Fu, W. Wang, F. Wen, J. Zhang, R. Bu, M. Ma, and H.-X. Wang, “Fabrication of diamond microlenses by chemical reflow method”, en, *Optics Express*, vol. 25, no. 2, p. 1185, 2017.

[227] T.-F. Zhu, J. Fu, Z. Liu, Y. Liang, W. Wang, F. Wen, J. Zhang, and H.-X. Wang, “Investigation of the occupancy ratio dependence for microlens arrays on diamond”, en, *RSC Advances*, vol. 8, no. 52, pp. 29 544–29 547, 2018.

[228] M. Karlsson and F. Nikolajeff, “Diamond micro-optics: microlenses and antireflection structured surfaces for the infrared spectral region”, en, *Optics Express*, vol. 11, no. 5, p. 502, 2003.

[229] Y. Li, Y. Zhang, L. Liu, and C. Yang, “Diamond micro-lenses with variable height using self-assembly silica-microsphere-monolayer as etching mask”, en, *Materials Today Communications*, vol. 11, pp. 119–122, 2017.

[230] Y. Zhang, Y. Li, L. Liu, C. Yang, Y. Chen, and S. Yu, “Demonstration of diamond microlens structures by a three-dimensional (3D) dual-mask method”, en, *Optics Express*, vol. 25, no. 13, p. 15 572, 2017.

[231] C. Lee, H. Choi, E. Gu, M. Dawson, and H. Murphy, “Fabrication and characterization of diamond micro-optics”, en, *Diamond and Related Materials*, vol. 15, no. 4-8, pp. 725–728, 2006.

[232] P. Siyushev, F. Kaiser, V. Jacques, I. Gerhardt, S. Bischof, H. Fedder, J. Dodson, M. Markham, D. Twitchen, F. Jelezko, and J. Wrachtrup, “Monolithic diamond optics for single photon detection”, en, *Applied Physics Letters*, vol. 97, no. 24, p. 241 902, 2010.

[233] J. P. Hadden, J. P. Harrison, A. C. Stanley-Clarke, L. Marseglia, Y.-L. D. Ho, B. R. Patton, J. L. O’Brien, and J. G. Rarity, “Strongly enhanced photon collection from diamond defect centers under microfabricated integrated solid immersion lenses”, en, *Applied Physics Letters*, vol. 97, no. 24, p. 241 901, 2010.

[234] L. Marseglia, J. P. Hadden, A. C. Stanley-Clarke, J. P. Harrison, B. Patton, Y.-L. D. Ho, B. Naydenov, F. Jelezko, J. Meijer, P. R. Dolan, J. M. Smith, J. G. Rarity, and J. L. O’Brien, “Nanofabricated solid immersion lenses registered to single emitters in diamond”, en, *Applied Physics Letters*, vol. 98, no. 13, p. 133 107, 2011.

[235] L. Poletto, P. Miotti, F. Frassetto, C. Spezzani, C. Grazioli, M. Coreno, B. Ressel, D. Gauthier, R. Ivanov, A. Ciavardini, M. de Simone, S. Stagira, and G. De Ninno, “Double-configuration grating monochromator for extreme-ultraviolet ultrafast pulses”, en, *Applied Optics*, vol. 53, no. 26, p. 5879, 2014.

[236] R. E. Bell, “Exploiting a transmission grating spectrometer”, en, *Review of Scientific Instruments*, vol. 75, no. 10, pp. 4158–4161, 2004.

[237] J. A. Davis and G. H. Evans, “Polarizing binary diffraction grating beam splitter”, en, *Optics Letters*, vol. 29, no. 13, p. 1443, 2004.

[238] D. H. Martz, H. T. Nguyen, D. Patel, J. A. Britten, D. Alessi, E. Krous, Y. Wang, M. A. Larotonda, J. George, B. Knollenberg, B. M. Luther, J. J. Rocca, and C. S. Menoni, “Large area high efficiency broad bandwidth 800 nm dielectric gratings for high energy laser pulse compression”, en, *Optics Express*, vol. 17, no. 26, p. 23 809, 2009.

[239] G. R. Harrison, “The production of diffraction gratings I. Development of the ruling art”, en, *Journal of the Optical Society of America*, vol. 39, no. 6, p. 413, 1949.

[240] A. Labeyrie and J. Flamand, “Spectrographic performance of holographically made diffraction gratings”, en, *Optics Communications*, vol. 1, no. 1, pp. 5–8, 1969.

[241] Y. Fu and B. K. A. Ngoi, “Investigation of diffractive optical element fabricated on diamond film by use of focused ion beam direct milling”, en, *Optical Engineering*, vol. 42, no. 8, p. 2214, 2003.

[242] P. Forsberg and M. Karlsson, “High aspect ratio optical gratings in diamond”, en, *Diamond and Related Materials*, vol. 34, pp. 19–24, 2013.

[243] M. Karlsson, K. Hjort, and F. Nikolajeff, “Transfer of continuous-relief diffractive structures into diamond by use of inductively coupled plasma dry etching”, en, *Optics Letters*, vol. 26, no. 22, p. 1752, 2001.

[244] M. Martínez-Calderon, J. J. Azkona, N. Casquero, A. Rodríguez, M. Domke, M. Gómez-Aranzadi, S. M. Olaizola, and E. Granados, “Tailoring diamond’s optical properties via direct femtosecond laser nanostructuring”, en, *Scientific Reports*, vol. 8, no. 1, p. 14 262, 2018.

[245] M. Karlsson and F. Nikolajeff, “Fabrication and evaluation of a diamond diffractive fan-out element for high power lasers”, en, *Optics Express*, vol. 11, no. 3, p. 191, 2003.

[246] E. Vargas Catalan, P. Forsberg, O. Absil, and M. Karlsson, “Controlling the profile of high aspect ratio gratings in diamond”, en, *Diamond and Related Materials*, vol. 63, pp. 60–68, 2016.

[247] C. Delacroix, P. Forsberg, M. Karlsson, D. Mawet, O. Absil, C. Hanot, J. Surdej, and S. Habraken, “Design, manufacturing, and performance analysis of mid-infrared achromatic half-wave plates with diamond subwavelength gratings”, en, *Applied Optics*, vol. 51, no. 24, p. 5897, 2012.

[248] P. Forsberg, M. Malmström, E. V. Catalan, and M. Karlsson, “Diamond grating waveplates”, en, *Optical Materials Express*, vol. 6, no. 6, p. 2024, 2016.

[249] E. V. Catalán, P. Piron, A. Jolivet, P. Forsberg, C. Delacroix, E. Huby, O. Absil, I. Vartiainen, M. Kuittinen, and M. Karlsson, “Subwavelength diamond gratings for vortex coronagraphy: towards an annular groove phase mask for shorter wavelengths and topological charge 4 designs”, en, *Optical Materials Express*, vol. 8, no. 7, p. 1976, 2018.

[250] M. Makita, P. Karvinen, V. Guzenko, N. Kujala, P. Vagovic, and C. David, “Fabrication of diamond diffraction gratings for experiments with intense hard x-rays”, en, *Microelectronic Engineering*, vol. 176, pp. 75–78, 2017.

[251] A. L. Stepanov, V. I. Nuzhdin, M. F. Galyautdinov, N. V. Kurbatova, V. F. Valeev, V. V. Vorobev, and Y. N. Osin, “A diffraction grating created in diamond substrate by boron ion implantation”, en, *Technical Physics Letters*, vol. 43, no. 1, pp. 104–106, 2017.

[252] J. F. Ziegler, M. Ziegler, and J. Biersack, "SRIM – The stopping and range of ions in matter (2010)", en, *Nuclear Instruments and Methods in Physics Research Section B: Beam Interactions with Materials and Atoms*, vol. 268, no. 11-12, pp. 1818–1823, 2010.

[253] F. Uhlén, D. Nilsson, A. Holmberg, H. M. Hertz, C. G. Schroer, F. Seiboth, J. Patommel, V. Meier, R. Hoppe, A. Schropp, H. J. Lee, B. Nagler, E. Galtier, J. Krzywinski, H. Sinn, and U. Vogt, "Damage investigation on tungsten and diamond diffractive optics at a hard x-ray free-electron laser", en, *Optics Express*, vol. 21, no. 7, p. 8051, 2013.

[254] C. David, S. Gorelick, S. Rutishauser, J. Krzywinski, J. Vila-Comamala, V. A. Guzenko, O. Bunk, E. Färm, M. Ritala, M. Cammarata, D. M. Fritz, R. Barrett, L. Samoylova, J. Grünert, and H. Sinn, "Nanofocusing of hard X-ray free electron laser pulses using diamond based Fresnel zone plates", en, *Scientific Reports*, vol. 1, no. 1, p. 57, 2011.

[255] N. Kujala, M. Makita, J. Liu, A. Zozulya, M. Sprung, C. David, and J. Grünert, "Characterizing transmissive diamond gratings as beam splitters for the hard X-ray single-shot spectrometer of the European XFEL", *Journal of Synchrotron Radiation*, vol. 26, no. 3, pp. 708–713, 2019.

[256] W Bogaerts and S. K. Selvaraja, "Compact Single-Mode Silicon Hybrid Rib/Strip Waveguide With Adiabatic Bends", *IEEE Photonics Journal*, vol. 3, no. 3, pp. 422–432, 2011.

[257] A. Schliesser and T. J. Kippenberg, "Cavity Optomechanics with Whispering-Gallery-Mode Microresonators", in *Cavity Optomechanics*, Springer Science + Business Media, 2014, pp. 121–148.

[258] D. Nečas and P. Klapetek, "Gwyddion: an open-source software for SPM data analysis", *Open Physics*, vol. 10, no. 1, 2012.

[259] I. S. LLC, *ImageMagick*, en, https://imagemagick.org/.

[260] M. Kiss, *Sample GWL writing program of the NanoScribe*, https://figshare.com/articles/Sample_GWL_writing_program_of_the_NanoScribe/9948593, 2019.

[261] M. Kiss, *Image conversion script*, https://figshare.com/articles/Image_conversion_script/9948605, 2019.

[262] *CIME – Interdisciplinary Centre for Electron Microscopy*, en-GB.

[263] C. Gui, M. Elwenspoek, N. Tas, and J. G. E. Gardeniers, "The effect of surface roughness on direct wafer bonding", en, *Journal of Applied Physics*, vol. 85, no. 10, pp. 7448–7454, 1999.

[264] D. W. Brenner and O. A. Shenderova, "Theory and modelling of diamond fracture from an atomic perspective", en, *Philosophical Transactions of the Royal Society A: Mathematical, Physical and Engineering Sciences*, vol. 373, no. 2038, p. 20 140 139, 2015.

[265] K. Petersen, "Dynamic micromechanics on silicon: Techniques and devices", *IEEE Transactions on Electron Devices*, vol. 25, no. 10, pp. 1241–1250, 1978.

[266] M. T. Kim, “Influence of substrates on the elastic reaction of films for the microindentation tests”, en, *Thin Solid Films*, vol. 283, no. 1-2, pp. 12–16, 1996.

[267] M. Kiss, *Roughness parameter extraction*, https://figshare.com/articles/Roughness_parameter_extraction/9948608, 2019.

[268] V. Dubey, J. Derakhshandeh, E. Beyne, J. Celis, and I. D. Wolf, “Fine Pitch Rapid Heat Self-Aligned Assembly and Liquid-Mediated Direct Bonding of Si Chips”, *IEEE Transactions on Components, Packaging and Manufacturing Technology*, vol. 6, no. 6, pp. 946–953, 2016.

[269] S. Tan, R. Boudreau, and M. Reed L., “Effects of mask misalignment and wafer misorientation on silicon v-groove etching”, *Sensors and Materials*, vol. 15, no. 2, pp. 101–112, 2003.

[270] O. Than and S. Büttgenbach, “Simulation of anisotropic chemical etching of crystalline silicon using a cellular automata model”, en, *Sensors and Actuators A: Physical*, vol. 45, no. 1, pp. 85–89, 1994.

[271] Zhenjun Zhu and Chang Liu, “Micromachining process simulation using a continuous cellular automata method”, *Journal of Microelectromechanical Systems*, vol. 9, no. 2, pp. 252–261, 2000.

[272] M. Kiss, *Crystallographic etch simulation code*, https://osapublishing.figshare.com/s/d099944c36163d07ea3c, 2019.

[273] M. Kiss, T. Graziosi, and N. Quack, “Trapezoidal diffraction grating beam splitters in single crystal diamond”, A. L. Glebov and P. O. Leisher, Eds., SPIE, 2018, p. 55.

[274] S. S. Singh, P. Pal, A. K. Pandey, Y. Xing, and K. Sato, “Determination of precise crystallographic directions for mask alignment in wet bulk micromachining for MEMS”, en, *Micro and Nano Systems Letters*, vol. 4, no. 1, p. 5, 2016.

[275] R. Otterbach, U. Hilleringmann, T. J. Horstmann, and K. Goser, “Structures with a minimum feature size of less than 100 nm in CVD-diamond for sensor applications”, *Diamond and Related Materials*, 11th European Conference on Diamond, Diamond-like Materials, Carbon Nanotubes, Nitrides and Silicon Carbide, vol. 10, no. 3, pp. 511–514, 2001.

[276] D. T. Tran, C. Fansler, T. A. Grotjohn, D. K. Reinhard, and J. Asmussen, “Investigation of mask selectivities and diamond etching using microwave plasma-assisted etching”, *Diamond and Related Materials*, Proceedings of Diamond 2009, The 20th European Conference on Diamond, Diamond-Like Materials, Carbon Nanotubes and Nitrides, Part 2, vol. 19, no. 7, pp. 778–782, 2010.

[277] X. Zhang, K. Chen, and S. M. Spearing, "Residual stress and fracture of thick dielectric films for power MEMS applications", in *Technical Digest. MEMS 2002 IEEE International Conference. Fifteenth IEEE International Conference on Micro Electro Mechanical Systems (Cat. No.02CH37266)*, 2002, pp. 164–167.

[278] H. Fujiyama, T. Sumomogi, and T. Endo, "Effect of O2 gas partial pressure on mechanical properties of SiO2 films deposited by radio frequency magnetron sputtering", *Journal of Vacuum Science & Technology A*, vol. 20, no. 2, pp. 356–361, 2002.

[279] C. M. Lauener, L. Petho, M. Chen, Y. Xiao, J. Michler, and J. M. Wheeler, "Fracture of Silicon: Influence of rate, positioning accuracy, FIB machining, and elevated temperatures on toughness measured by pillar indentation splitting", *Materials & Design*, vol. 142, pp. 340–349, 2018.

[280] R. Ramachandramoorthy, J. Schwiedrzik, L. Petho, C. Guerra-Nuñez, D. Frey, J.-M. Breguet, and J. Michler, "Dynamic Plasticity and Failure of Microscale Glass: Rate-Dependent Ductile–Brittle–Ductile Transition", *Nano Letters*, vol. 19, no. 4, pp. 2350–2359, 2019.

[281] G. M. Beheim and L. J. Evans, "Control of Trenching and Surface Roughness in Deep Reactive Ion Etched 4H and 6H SiC", en, *MRS Proceedings*, vol. 911, 2006.

[282] U. Umhofer, E. Jäger, and C. Bischoff, "Refractive and diffractive laser beam shaping optics", *Laser Technik Journal*, vol. 8, 2011.

[283] M. Ciofini, A. Lapucci, and S. Lolli, "Diffractive optical components for high power laser beam sampling", en, *Journal of Optics A: Pure and Applied Optics*, vol. 5, no. 3, pp. 186–191, 2003.

[284] J. Hugonin and P. Lalanne, *Reticolo software for grating analysis*, Institut d'Optique, Orsay, France, 2005.

[285] C. Rockstuhl, I. Marki, T. Scharf, M. Salt, H. Peter Herzig, and R. Dandliker, "High resolution interference microscopy: a tool for probing optical waves in the far-field on a nanometric length scale", en, *Current Nanoscience*, vol. 2, no. 4, pp. 337–350, 2006.

[286] K. Johnson, *GD-Calc*.

[287] J Kell, J. R. Tyrer, R. L. Higginson, J. C. Jones, and S Noden, "Laser weld pool management through diffractive holographic optics", en, *Materials Science and Technology*, vol. 28, no. 3, pp. 354–363, 2012.

[288] J. B. Hammond, E. G. Johnson, C. S. Koehler, J. D. Stack, T. J. Suleski, A. Kar, and W. Guo, "Diffractive optics for laser welding and bonding", in *Optoelectronics '99 - Integrated Optoelectronic Devices*, I. Cindrich, S. H. Lee, and R. L. Sutherland, Eds., San Jose, CA, 1999, pp. 206–213.

[289] C. Kong, M. Bolut, J. Sundqvist, A. Kaplan, E. Assunção, L. Quintino, and J. Blackburn, “Single-pulse Conduction Limited Laser Welding Using A Diffractive Optical Element”, *Physics Procedia*, vol. 83, pp. 1217–1222, 2016, Laser Assisted Net Shape Engineering 9 International Conference on Photonic Technologies Proceedings of the LANE 2016 September 19-22, 2016 Fürth, Germany.

[290] H. Zhong, S. Zhang, and F. Wyrowski, “Parabasal thin-element approximation approach for the analysis of microstructured interfaces and freeform surfaces”, *J. Opt. Soc. Am. A*, vol. 32, no. 1, pp. 124–129, 2015.

[291] R. Gerchberg and A Saxton W. O., “A practical algorithm for the determination of phase from image and diffraction plane pictures”, *Optik*, vol. 35, pp. 237–250, 1971.

Marcell Kiss

1022 Chavannes-près-Renens
Chemin des Ramiers 16
☎ *+41 76 606 6058*
✉ *marcell.kiss@epfl.ch*

Education

2015–*2019*	**PhD**, *École Polytechnique Federale de Lausanne*, STI IMT GR-QUA.
Thesis	Advanced Diamond Microfabrication for Microoptics and Photonics
2013–2015	**MSc**, *Budapest University of Technology and Economics*, Electrical Engineering, Major specialisation: Micro- and nanoelectronics.
Thesis	Development of a MEMS device for neural optical stimulation
2013. 07.	**Visiting scholar**, *ETH Zürich, Institute for Biomedical Engineering*.
2009–2013	**BSc**, *Budapest University of Technology and Economics*, Electrical Engineering, Specialisation: Microelectronics.
Thesis	Development of polymer-based microstructures for biomedical applications

Employment

2015–*2019*	**Research assistant**, *École Polytechnique Federale de Lausanne*, STI IMT GR-QUA.
2012–2015	**Research intern**, *Hungarian Academy of Sciences*, Institute for Technical Physics and Materials Science.

Selected publications

Kiss M., Graziosi T., Toros A., Scharf T., Santschi C., Martin J. F. O., Quack N.: *High Quality Single Crystal Diamond Diffraction Gratings Fabricated by Crystallographic Etching*, Optics Express (2019)

Toros A., Kiss M., Graziosi T., Sattari H., Gallo P., Quack N.: *Precision micromechanical components in single crystal diamond by deep reactive ion etching*, Microsystems & Nanoengineering (2018)

Kiss M., Földesy P., Fekete Z.: *Optimization of a Michigan-type silicon microprobe for infrared neural stimulation*, Sensors and Actuators B: Chemical (2015)

Márton G., Orbán G., Kiss M., Fiáth R., Pongrácz A., Ulbert I.: *A Multimodal, SU-8 - Platinum - Polyimide Microelectrode Array for Chronic* In Vivo *Neurophysiology*, PLOS One (2015)

Experience & Skills

- Cleanroom fabrication expertise
- Diamond micro/nanofabrication
- Optical simulation / COMSOL
- SEM & TEM
- Matlab & C++

Language skills

- **English** C1
- **French** B1

Ce document a été imprimé au Centre d'impression EPFL,
imprimerie climatiquement neutre, certifiée myClimate.